Multi-scale Modeling of Deformation and Failure Mechanisms of Al Alloys at Elevated Temperature

By Ningning Du

B.S., Tsinghua University, 2002

M.S., Tsinghua University, 2004

M.S., Brown University, 2008

A Dissertation Submitted in Partial Fulfillment of the

Requirements for the Degree of Doctor of Philosophy in the Division of Engineering

at Brown University

Providence, Rhode Island

May 2010

This dissertation by Ningning Du is accepted in its present form

by the Division of Engineering as satisfying the

dissertation requirement for the degree of Doctor of Philosophy.

Date _____ _____

Allan F. Bower, Advisor

Recommended to the Graduate Council

Date _____ _____

Huajian Gao, Reader

Date _____ _____

Eric Chason, Reader

Approved by the Graduate Council

Date _____ _____

Sheila Bonde, Dean of the Graduate School

Curriculum Vitae

Ningning Du was born on March 20th, 1981 in Changle of Shandong Province in The People's Republic of China. She grew up and attended several schools in Changle before she went to college at Tsinghua University in Beijing in 1998. She graduated with a Bachelor's degree in 2002 and a Master's degree in 2004, both in Engineering Mechanics. In 2004 she entered Brown University to continue her studies in Engineering. At Brown, she majored in Solid Mechanics with minors in both Material Science and Applied Mathematics. She coauthored a number of journal and conference publications during her graduate school study. She was awarded a Master's degree in Applied Mathematics in 2008. Ningning defended her Ph.D dissertation on July 29th, 2009.

Acknowledgements

I would like to express my sincere gratitude to my advisor, Professor Allan Bower for his excellent guidance, teaching and constant encouragement throughout the course of my dissertation. His scientific insight, as well as great sense of humor, have made being his student a truly wonderful experience for me.

I would also like to extend my appreciation to Dr. Paul Krajewski, Dr. Yue Qi and Dr. Louis Hector for their guidance and collaboration on a number of research projects. Many thanks to Dr. Yue Qi for receiving me as an intern student at General Motors Research and Development for two summers.

I would also like to thank the Brown University solid mechanics community. The excellent academic atmosphere has helped me to absorb knowledge both crucial for my research as well as for my academic and professional progress more generally.

Special thanks to my family and friends, and to Kevin Morris in particular. I would not have come this far without your love and support.

Finally, I would like to thank the readers, Professor Huajian Gao and Professor Eric Chason, for carefully reviewing this manuscript. I am also grateful for the financial support from the GM-Brown Collaborative Research Lab.

Table of Contents

List of Tables

List of Figures

Chapter 1: Introduction

1.1 Overview

Superplasticity is the ability of certain materials to exhibit very large tensile elongations (sometimes over 1000%) prior to failure in a generally isotropic manner[1]. Figure 1-1 shows a sample of Cu-Al alloy being uniaxially stretched to 8000% strain without significant necking. Superplasticity has been found in over 10,000 different materials including metals, ceramics, intermetallics, composites and more recently in nanocrystalline materials[2]. Many superplastic materials are also capable of conventional plastic deformation, and can only be brought to superplastic state under restrictive conditions such as elevated temperature ($T > 0.5T_m$, where T_m is the melting temperature) and a narrow strain rate range (usually around $10^{-4}s^{-1}$).

Superplasticity has been successfully exploited in industrial manufacturing processes such as superplastic forming [3-5]. Recently research on superplastic materials such as aluminum and magnesium alloys has become increasingly important in the automotive industry because of the emergence of a new warm forming technology called quick plastic forming [6-8]. Auto parts such as body panels made with these light alloys through the QPF technologies provides higher strength to weight ratio compared to steel and can provide weight reduction of up to 50% and therefore higher vehicle fuel efficiency[9]. Currently the utilization of this technology in mass production is hindered

by the high cost of the raw materials. The development and characterization of materials that exhibits sufficient formability under the QPF condition and are suitable for mass production is critical to the success of the technology and next generation of fuel efficient vehicles.

Superplasticity is of practical and scientific significance not only because of the resulting extraordinary ductility, but also because of its unique underlying physical mechanisms. While the conventional metal plasticity is usually induced by intragranular dislocation slip, superplasticity is controlled by grain boundary deformation, through processes such as grain boundary sliding and grain boundary diffusion, as well as the interaction of these grain boundaries processes with intragranular deformation. Since the 1960s significant progress has been made toward understanding superplasticity and superplastic materials. But there are still many open questions that need to be addressed in order to completely understand the deformation, to be able to make reliable quantitive predictions, and to ultimately modify and design engineered materials that is suitable for various purposes.

This dissertation investigates some aspects that are related to the deformation and failure of superplastic materials with numerical simulations of multiple time and length scales. Microstructure based finite element simulations are used to predict the constitutive relation and cavitation of the material from an assembly of grains, and are linked to continuum finite element models to simulate metal forming. In addition, molecular dynamics simulations are used to study the effect of grain boundary chemistry on grain boundary sliding.

1.2 Current Understandings of Superplasticity

Superplasticity was initially documented in 1912 and became the subject of intensive research since 1960s. Two types of superplasticity have been documented [1]. The first type is fine-structure superplasticity and as its name suggests, it requires materials with fine grain size (usually less than 10 μm), evenly distributed second phase or particles at grain boundaries to inhibit grain growth during deformation, equiaxed grains, and a large number of high energy grain boundaries. The second type is internal stress superplasticity, which is generated by developing internal incompatible stress within the material, using processes such as thermal cycling or pressure cycling of polymorphic material through phase change, thermal cycling of pure metals or single phase alloys that have anisotropic thermal, or thermal cycling of composite materials in which the constituents have different thermal expansion coefficients. In this dissertation we only consider materials that are capable of the first type of superplasticity.

Experimental observations of superplastic materials reveal that they possess several universal features:

1. A sigmoidal flow stress versus strain rate curve, with high strain rate sensitivity when superplasticity occurs,
2. The retention of random texture and equiaxed grain shapes in superplastic deformation, and
3. Failure due to extensive cavitation.

This section will first briefly summarize these characteristics of the superplastic materials, and then review the current understanding of the deformation mechanisms.

1.2.1 Mechanical Response of Uniaxial Tension

When a superplastic material is subjected to uniaxial tension with a wide range of strain rates, the plot of flow stress as a function of strain rate on a log-log scale usually exhibits a sigmoidal shape. Figure 1-2(a) shows the flow stress as a function of strain rate for a superplastic aluminum alloy. The material is tested at two temperature, 550℃ and 570℃. For each temperature, the flow stress versus strain rate curve can be divided into three regions, region I, II and III, according to the value of strain rate sensitivity *m* which is defined in the following phenomenological equation,

$$\sigma = C\dot{\varepsilon}^{m}, \tag{1.1}$$

where σ is the true flow stress, *C* is a constant which depends on the temperature and microstructural quantities such as grain size, $\dot{\varepsilon}$ is the true strain rate. At low strain rate, in region I, the flow stress is low and its dependence on strain rate is relatively mild with a low value of *m* (about 0.2). As the strain rate increases, the dependence of flow stress on strain rate becomes stronger with *m* about 0.5. In region III at fast strain rates, the strain rate sensitivity decreases again and approach the characteristic values of typical ductile materials.

The corresponding elongation-to-failure strain as a function of strain rate is plotted in Figure 1-3 (b) and it shows that the maximum elongation-to-failure of the material is achieved in region II. For a typical superplastic material, region II is where superplasticity occurs. It has been recognized that the strain rate sensitivity is directly related to the ductility of superplastic materials. The reason that maximum ductility is achieved in region II is generally believed to be that high values of *m* increases local

strain rate during the necking process, which causes local hardening and prevents further strain localization[1].

The flow stress and strain rate sensitivity also varies with temperature and microstructural features such as average grain size and grain size distribution. For example, Figure 1-3(a) shows that the stress-strain rate curve becomes flatter and the strain rate range corresponding to the maximum strain rate sensitivity *m* decreases as temperature decreases. Figure 1-4 shows the effect of grain size on the flow stress versus strain rate curve for an aluminum alloy and one can observe that increasing grain size has a similar effect of decreasing temperature on the stress –strain rate curve. When the temperature is sufficiently low or grain size is sufficiently large, the stress – strain rate curve can become absolutely flat, and the superplastic state of the materials disappears. It is also interesting to note from Figure 1-4 that the mechanical response of the material is very sensitive to the change of the grain size at low strain rates but becomes less sensitive at high strain rates.

The change of strain rate sensitivity and ductility with strain rate, temperature and grain size clearly suggest transition of deformation mechanisms in these materials under different conditions. It is well established that there are multiple mechanisms operating in these materials and these possible mechanisms are grain boundary sliding, intragranular dislocation slip and grain boundary diffusion [10]. It is generally believed that in region II, where superplasticity occurs, the dominant deformation mechanism is grain boundary sliding. Region II thus is also referred to as grain boundary sliding regime in literature. Grain boundary sliding is the rigid translation of adjacent grains parallel to grain boundary plane, as illustrated in Figure 1-5. Numerous experiments

have observed grain boundary sliding during superplastic deformation with pre-existing markers on the surface of the material. Figure 1-6 shows an example of such experiments in a superplastically deformed Mg-0.78%Al alloy. The offset of the transverse marker line clearly reveals that grain boundary sliding occurs between some of the adjacent grains, and the markers have no distortion within the grains suggests minimal grain deformation and shape change during superplastic deformation. In region III at fast strain rate, dislocation activities within the grains become dominant and the deformation of the materials gradually transform from superplastic state to conventional plastic state as strain rate increases. Region III is also called dislocation creep regime. The deformation mechanism in region I is not well known and is attributed to threshold stress for superplasticity.

Though grain boundary sliding is generally considered as a main deformation mechanism for superplasticity, it is more difficult to make quantitive predictions of the contribution of grain boundary sliding to the total deformation under various conditions. Some efforts have been to measure the displacement of the surface scratches to predict the contribution (reviewed by [10] and [11]). But these prediction have a few limitations, first, the interfering effect of the scratches, these scratches might change the grain boundary structure and chemistry. Second, the displacement measured from the surface does not necessarily accurately present the sliding amount within the body. Third, lack of in-situ measurements taking in account of the grain rearrangement often leads to underestimate of the sliding amount. Other approaches all based on phenomenological constitutive models, and these models often over simplify the microstructure and overlook the grain level inhomogenity and thus make the prediction unreliable.

1.2.2 Microstructure Evolution

Superplasticity is different from conventional plasticity not only because it possesses much higher strain rate sensitivity but also because it exhibits different microstructural evolution during the deformation. Figure 1-7 contains the sketches of microstructural evolution of plasticity and superplasticity. In conventional plasticity, the deformation mechanism is intragranular dislocation slip. During the deformation, the grains are elongated along the tension direction, and usually a strong texture develops due to the gradual rotation of the slip systems, or the crystal orientation. The elongation strain is mainly accommodated by the shape change of grains due to dislocation slip. This was sketched in Figure 1-7(a). In contrast, during superplastic deformation, the elongation strain is mainly accommodated by the rearrangement of the grains along the tension direction: the grains slide against each other and at some point during the deformation some peculiar events that are only seen in superplasticity such as switch of neighboring grains. Through these events, the grains line up in the tension direction to accommodate the elongation of the material. Even after extraordinary elongation, the grains remain equiaxed. In addition, it is commonly observed that after superplastic deformation the crystallographic orientations of the grains remain randomly distributed. Figure 1-8 shows the EBSD images of an Al AA5083 material tested by uniaxial tension at elevated temperature and different strain rate. Figure 1-8(a) is the EBSD image of the undeformed material in the grip area and it shows that the material initially has randomly distributed crystallographic orientations. Figure 1-8(b)-(d) show that at low strain rate (0.0005/s), the orientation of the grains remains randomly distributed after deformation, while deformation texture develops as higher strain rates and the intensity of the texture

becomes stronger as strain rate increases. It can also be seen that the grains are significantly elongated at strain rate 0.01/s while the grains remain equiaxed at strain rate 0.0005/s.

The difference in microstructure evolution during deformation at slow and fast strain rate provides additional evidence to the mechanism transition in superplastic materials. The texture randomization at low strain rates is believed to occur due to grain boundary sliding, which is the dominant mechanism of deformation at low strain rates, while at high strain rates, dislocation slip causes the grains to orient in a preferred direction and a crystallographic texture develops.

1.2.3 Failure

It is accepted that the failure of superplastic materials at elevated temperature is controlled by two competing process: flow localization such as necking and extensive cavitation. When the deformation is controlled by dislocation creep, the deformation is accompanied by continuous hardening of the materials and they are finally failed by localized deformation such as necking. In contrast, when the deformation is controlled by grain boundary sliding, increased porosity is often observed in a wide range of materials such as alloys based on copper, aluminum, nickel and magnesium. Failure in superplastic deformation usually occurs by cavity nucleation, coalescence and eventually the rapture of the materials. Figure 1-9 shows an example of an Al AA5083 alloy failed by different mechanisms when deformed in dislocation creep regime and grain boundary sliding regime respectively.

The literature on cavity nucleation and growth is substantial. Experimental observations suggest that cavities are mostly likely nucleated at grain boundary particles and triple junctions. They can pre-exist and continuously nucleate during deformation. In general, experiments report much larger cavity volume fraction in samples deformed in the grain boundary sliding regime than those deformed in the dislocation creep regime. Micrographs of the samples deformed in the dislocation regime show that cavities can also be observed but have different morphology than the cavities in the materials deformed in grain boundary sliding regime. As shown in Figure 1-10, under dislocation creep, cavities coalesce along the tensile axis into thin, stringer like formations. Under grain boundary sliding creep, cavities coalesce in a more isotropic manner, with fewer stringerlike features and significant coalescence perpendicular to the tensile axis.

In summary, cavitation is the limiting factor for tensile elongations and is likely to have a deleterious effect on the postforming properties of commercially formed parts.

1.2.4 Nature of Grain Boundary Sliding

It has been established in the previous sections that the superplastic flow is a results of operating of multiple mechanisms including grain interior dislocation slip, grain boundary diffusion and grain boundary sliding. There is no doubt that grain boundaries play essential role in superplastic flow. The plasticity caused by grain boundary processes (Grain-boundary sliding, grain-boundary migration and lattice slip localized in regions adjacent to grain boundaries) has been recently termed as ‘grain boundary plasticity’ [12]

The understanding of the role of grain boundaries in superplasticity and the elementary mechanisms of grain boundary plasticity has always been the main focus of the research on superplasticity. Among the deformation mechanisms grain boundary sliding is the most studiesd one, because it is geometrically simple but its atomic mechanism is complicated partly due to the complexity of grain boundary structure itself, and partly due to the interaction of grain boundary sliding with other deformation mechanisms.

Precisely by what the atomistic process grain boundary sliding in a polycrystal occurs has been debated since the early stage of superplasticity research and is still not clearly understood. Due to the incompatible nature of grain boundary sliding, there must be some accommodation mechanism in the polycrystal when grain boundary sliding occurs. It is not geometrically possible for grains to slide against each other without changing shape or creating extensive openings at triple junctions.

Traditionally dislocation slip or grain boundary diffusion are believed to be the accommodation mechanisms and a number of micromechanics models were proposed for grain boundary sliding since the 1970s. These models focus on postulating the atomic mechanism for grain boundary sliding, and calculating the resulting phenomenological relation of grain boundary sliding creep. Each of these models claims a different atomic mechanism of grain boundary sliding and predicts a rate equation for region II of the superplastic curve based on the assumption of homogenous microstructures (namely, the microstructure is reduced to an average grain size). These models can be classified into three groups based on different accommodation mechanisms: (i) grain boundary sliding accommodated by diffusion (ii) grain boundary sliding accommodated by dislocation slip

(iii) grain boundary sliding with no accommodation mechanism. The above two groups of models all assume that the removal of the obstacles of grain boundary sliding (for example, triple junctions and steps) either by diffusion or dislocation activities is the rate controlling process.

Among the models of grain boundary sliding accommodated by diffusion, the Raj-Ashby model [13] and Ashby-Verrall model [14] are the two most famous. Raj-Ashby model considers that grain boundary diffusion controls the sliding rate of a curved grain boundary. Ashby and Verrall proposed a mechanism for the grains to switch neighbors without changing their shape significantly and line up in the loading direction by grain boundary sliding accommodated by diffusion flow (sketched in Figure 1-11). A threshold stress for grain boundary sliding is predicted from this model due to the increased surface of the boundaries during the grain rearrangement, and it can be used to explain the decreased strain rate sensitivity in region I on the typical stress-strain rate curve. The intermediate step in Ashby-Verrall model was also modified by Ashby et al. [15], from irregularly shaped grains to square grains and used to calculate upper and lower bounds for creep rates during the neighbor switching mechanism. More recently Yang and Wang [16, 17] proposed a model of a 9-grain cluster that incorporates both the Ashby–Verrall mechanism and grain rotation.

Grain boundary sliding accommodated by dislocation slip is the most studied mechanism of deformation in superplasticity. The first model for grain boundary sliding accommodated by slip mechanism was proposed by Ball and Hutchinson [18]. Their model considers sliding of a group of grains and assumes that grain boundary sliding occurs easily but is restricted by obstacles such as triple junctions. grain boundary

sliding is accommodated by generation of dislocations at these obstacles and their subsequent movement across the grains and accumulation at opposite grains. The rate-controlling step in this theory is dislocation climb. The rate controlling process is the sliding of the leading dislocations in the pile-up along the boundary towards the region of their annihilation. Mukherjee [19] proposed a similar model for grain boundary sliding in which the rate is controlled by dislocation motion within the grains but with the assumption that grain boundary sliding occurs not in groups of grains, but in individual grain boundaries. The dislocations originate from the protrusions or ledges on a grain boundary surface instead triple junctions. Dislocation climb from these sites is the rate controlling step. Langdon [20] proposed a model in which dislocations originate within the grains (rather than at boundary obstacles like in Ball and Hutchinson model) and enter the grain boundary region by slip. Hayden et al [21] proposed a model that assumes that the dislocations generated at the grain boundaries move through the grains and subsequently climb along the opposite boundaries where their annihilation takes place. Arieli and Mukherjee [22] assume that the climbing dislocations themselves get multiplied according to the Bardin-Herring mechanism. Gifkins [23] proposed the 'core-and-mantle' model which assumes that plastic flow arises from two separate mechanisms: grain boundary sliding accommodated by the movement of lattice dislocations in the thin 'mantle' region near the grain boundaries, and dislocation slip in the 'core' region (sketched in Figure 1-12). Ghosh [24] modified "core and mantle" model to incooperate grain growth. It is assumed that both grain boundary sliding and grain growth are controlled by dislocation glide and climb in the mantle region. Gittus [25] has developed a theory specifically for two-phase materials in which grain boundary sliding occurs by

dislocation activity in the interphase-boundary. This model also considers a threshold stress associated with pinning of dislocations at the ledges in the interphase-boundary. The activation energy is the same as that for interphase-boundary diffusion. Kaibyshev et al [26] proposed a model on the basis of hardening due to easy generation of lattice dislocations in the boundaries and recovery. Langdon [27, 28] proposed a unified model to explain grain boundary sliding in both fine and coarse grained materials (Figure 1-13). When the grain size larger than the equilibrium subgrain size as shown in Figure 1-7(a), conventional plasticity occurs and the stress concentration at the triple point A leads to intragranular slip in the adjacent grain and these dislocations pile up at the first subgrain boundary at B. By contrast, no subgrains are formed in superplasticity when the grain size is less than the equilibrium subgrain size and the stress concentration at the triple point C leads to intragranular slip in the opposing grain and the dislocations then pile up at the opposite grain boundary at D. The rate equations for these two processes are governed by the rate of removal of dislocations from the heads of the pile-ups at B and D.

The models of the third group assume that grain boundary sliding does not need accommodation mechanism and grain boundary sliding itself is the rate controlling process. A theory of “pure” grain boundary sliding was given by Padmanabhan [29] in which deformation takes place only at the grain boundaries and needs no accommodation. Grain boundary sliding is aided by diffusional flow, which is not a rate controlling process.

In summary, each model has its own strength and weakness, and some models give satisfactory phenomenological equations compared to experiments. Although these

models are based on postulated mechanism for grain boundary sliding, they give great insight to the nature of grain boundary sliding and superplasticity.

Recent advancement of modern research facilities such as high-resolution electron microscopy and analytical techniques such as atomistic simulations has shed new lights on the physical mechanism of grain boundary sliding. A variety of atomic mechanisms for grain boundary sliding have been confirmed or newly found: Simulations [30-39] indicate that grain boundary sliding could occur by various mechanisms under different condition, for example, diffusion, stick-slip, atom shuffling, dislocation nucleation, partial melting, or resultant from boundary migration.

A few other interesting characteristics of sliding of individual grain boundaries have emerged through direct measurements of bicystals or tricrystals (in Al [40-47], in Cu[48-50] and in Zn [51, 52]) and numerical simulations [30-36]:

1. Grain boundary sliding is strongly depends on the grain boundary energy, the bicrystallagraphy and even the detailed atomic structure of the grain boundary. In general, experiments and simulations predict that low angle grain boundaries or ordered boundaries near coincidence orientations have higher sliding resistance.
2. Threshold stress exists for grain boundary sliding: As suggested by postulated models of Ashby-Verrall model [14] and Gittus [25], a number of experiments [53] as well as atomistic simulations [32] suggested that there exist a threshold stress for grain boundary sliding. This means that below this threshold no sliding occurs. This threshold stress should also be responsible to the superplastic material behavior in region I. The origin of the threshold stress is not clear and estimates of the threshold

stress for grain boundary sliding vary, and suggest it is a function of temperature, grain size and grain boundary misorientation.

3. Anisotropy: Some experiments and simulations also suggest that the grain boundary sliding is anisotropic within the grain boundary plane. For example, Shiga and Shinoda [35] found that for tilt grain boundaries, the sliding parallel to tilt axis is much easier than the sliding perpendicular to this direction. Uesugi et al [36] also found that compared to tilt grain boundaries, twist grain boundaries is less anisotropic within the grain boundary plane.
4. Solute effect: the superplastic deformation behavior of aluminum alloys can be significantly affected by slight variations in material chemistry.

1.3 Summary of the Thesis

Current knowledge of superplasticity suggests that there are a number of aspects of the phenomenon that remain unclear or untouched, such as what is the contribution of each possible mechanism to the total deformation and how the mechanisms are interrelated to each other. Other questions include how does the deformation mechanism transition happen? How do microstructure features affect the constitutive relation and the failure of superplastic material and how to engineer the microstructure and grain boundary chemistry to achieve desired formability?

Our ultimate goal is to predict the effect of grain boundary chemistry and microstructure on the formability of these materials, and provide recommendations on how to modify the material to achieve the desired mechanical properties (such as

ductility). To this end, a number of problems that are related to the deformation and failure mechanisms of superplastic materials were investigated using numerical simulations of various time and scale lengths. Specifically, these problems are:

1. Prediction of the constitutive relation of superplastic flow and contribution from each possible deformation mechanisms using a microstructure based finite element model [54] that accounts rigorously for the coupling of grain interior dislocation slip, grain boundary diffusion and grain boundary sliding. Specifically, the model was used to estimate the influence of a threshold stress for grain boundary sliding on the relationship between macroscopic flow stress and strain rate for the aluminum alloy AA5083 when subjected to plane strain uniaxial tension at 450°C.
2. Void growth during elevated temperature straining of polycrystalline AA 5083 Aluminum alloy was simulated with the microstructure base finite element computations based on a realistic 2D grain structure. The simulations are used to predict the influence of loading conditions, material properties and microstructure on void growth rates.
3. The influence of alloying elements (Si and Mg) and vacancies segregated to grain boundaries on the sliding of Al bicrystals at elevated temperature is investigated with molecular dynamics simulations. The threshold stress for grain boundary sliding is estimated for six grain boundary structures including one symmetric tilt grain boundary and five asymmetric tilt grain boundaries.
4. The microstructure based finite element model is combined with continuum finite element simulations to predict the effect of grain size on bulge forming of AA5083 at 450ºC and the results are compared with experimental measurements. Modeling was

done in two stages: (1) a microstructure-based finite element method for predicting the constitutive response at elevated temperature was employed to generate constitutive behavior for materials with the same grain sizes used experimentally and (2) these constitutive equations were used in a finite element forming simulation to predict biaxial bulge forming. This work establishes a framework for multi-scale modeling of deformation which can be applied to the forming of more complicated shape and stress state as well as other materials.

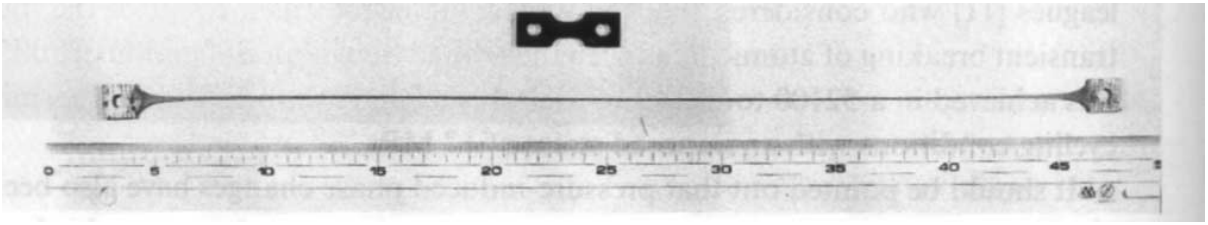

Figure 1-1 Superplasticity in a Cu-Al alloy. The image shows a sample before and after uniaxial tension. 8000% strain is achieved without significant necking. Figure take from [2].

Figure 1-2 Deck lid of Cadillac STS car made using the QPF process. (a) inner panel, and (b) outer panel. Inner and outer panels are hemmed together to make the assembly panel. Courtesy of General Motors R&D Center.

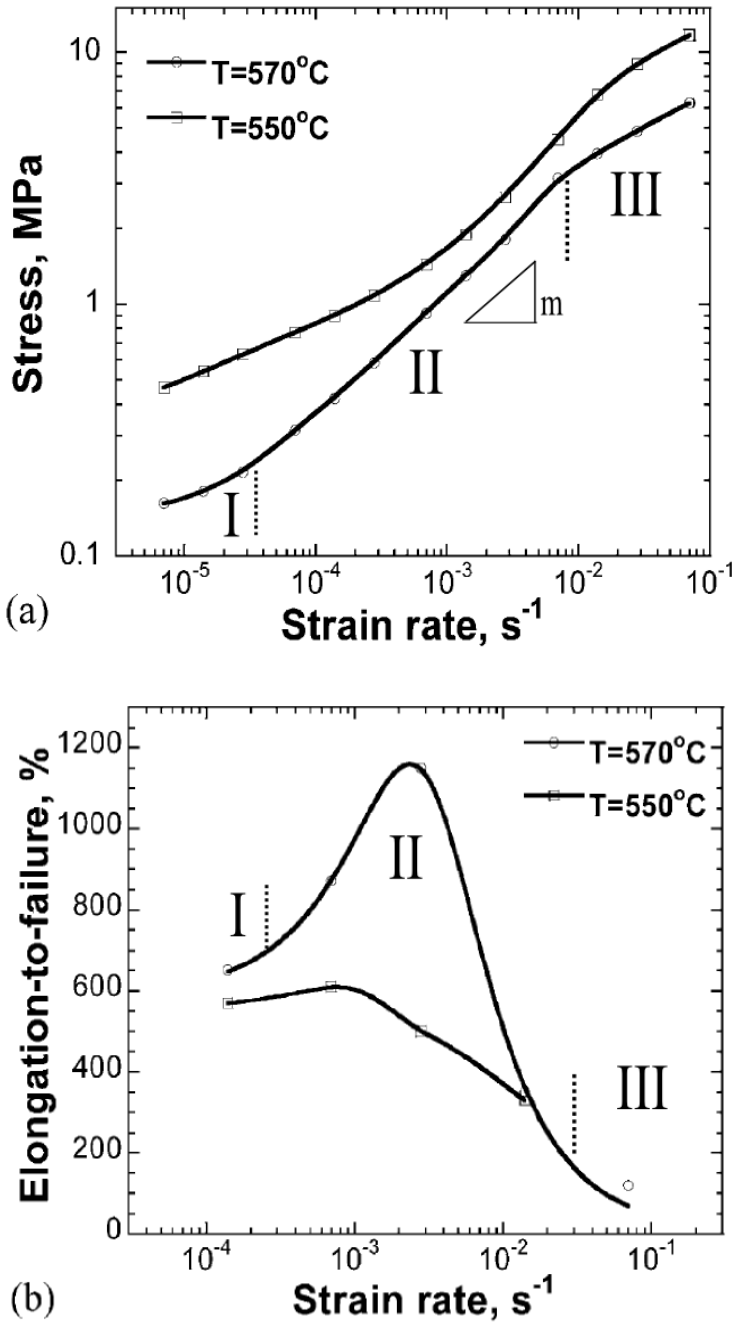

Figure 1-3 (a) Flow stress and (b) elongation to failure vs strain rate for 0.2%Zr and 1.6%Mn modified 5083 aluminum alloy having a grain size of 6.2 μm, tested at temperatures in the range from 550 to 570 ℃ [55]. The stress-strain rate plot can be divided into three regions marked as I, II and III. Note the boundaries of these regions change with temperature and as temperature decreases, the level of flow stress increases and the sigmoidal curve shape becomes flatter.

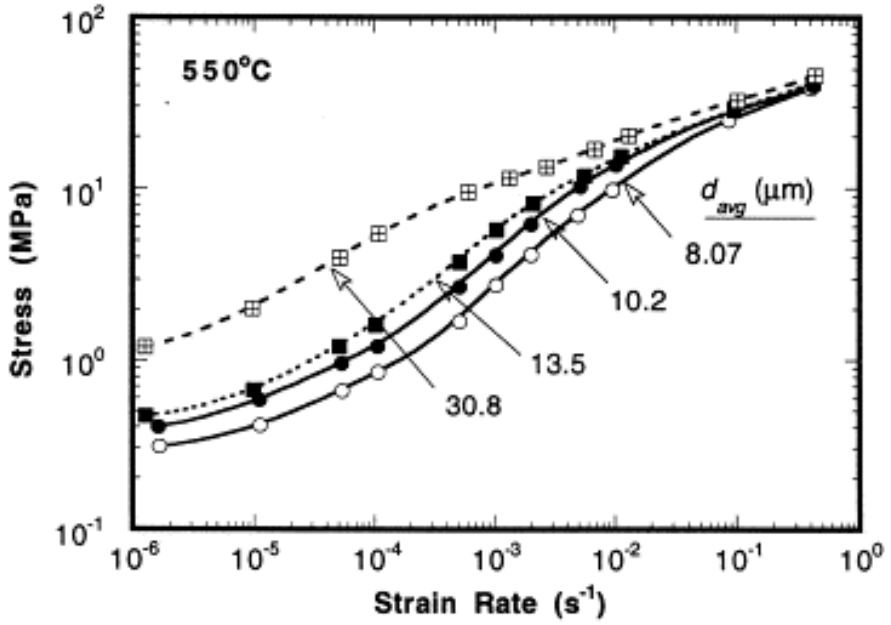

Figure 1-4 Grain size dependence of the stress vs strain-rate relationship for an Al–Mg–Mn–Cu alloy at a temperature of 550°C. As the grain size increases, the level of flow stress increases and the sigmoidal curve shape becomes flatter. [56].

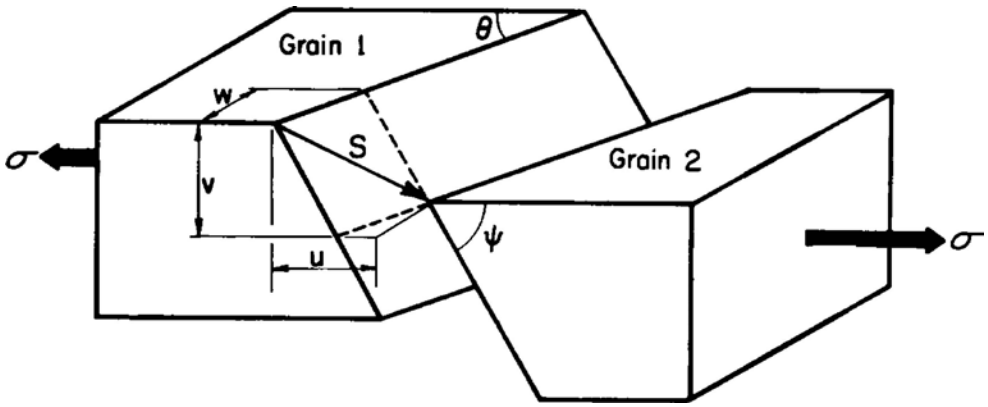

Figure 1-5 Sketch of grain boundary sliding. Taken from [28].

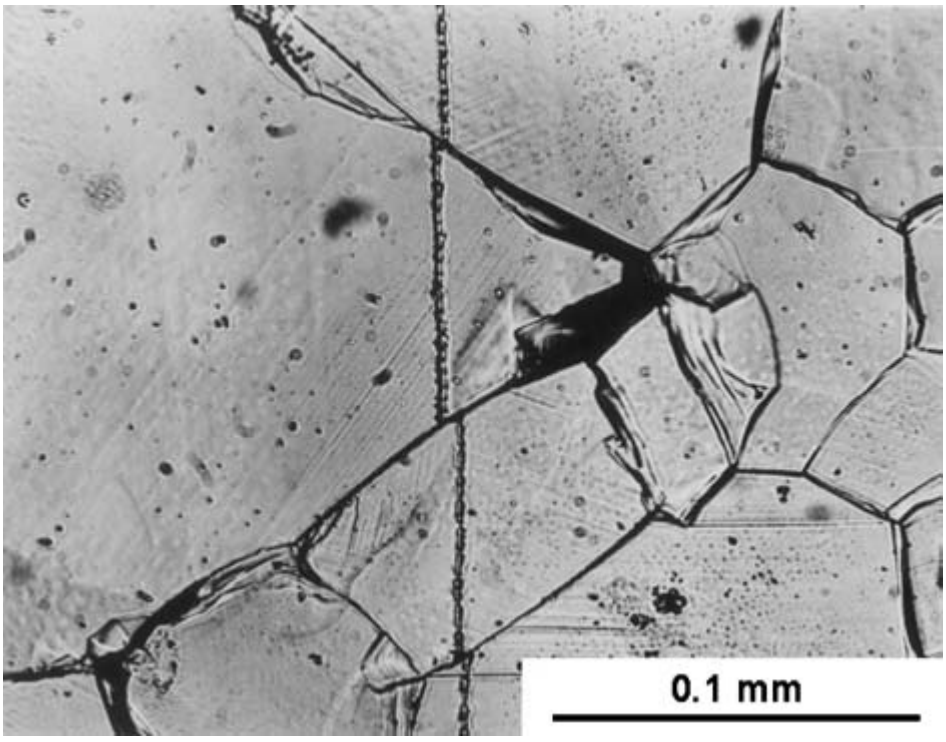

Figure 1-6 The occurrence of grain boundary sliding revealed by the boundary offsets in a transverse marker line for aMg-0.78% Al alloy tested under creep conditions at 473 K: the tensile axis is horizontal. Taken from [28].

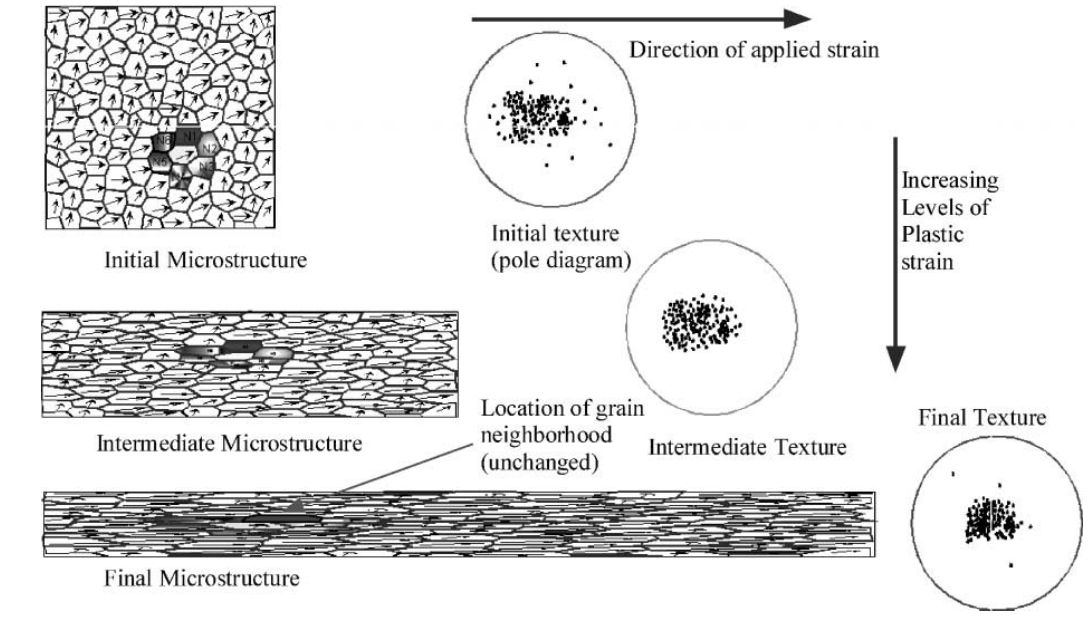

(a)

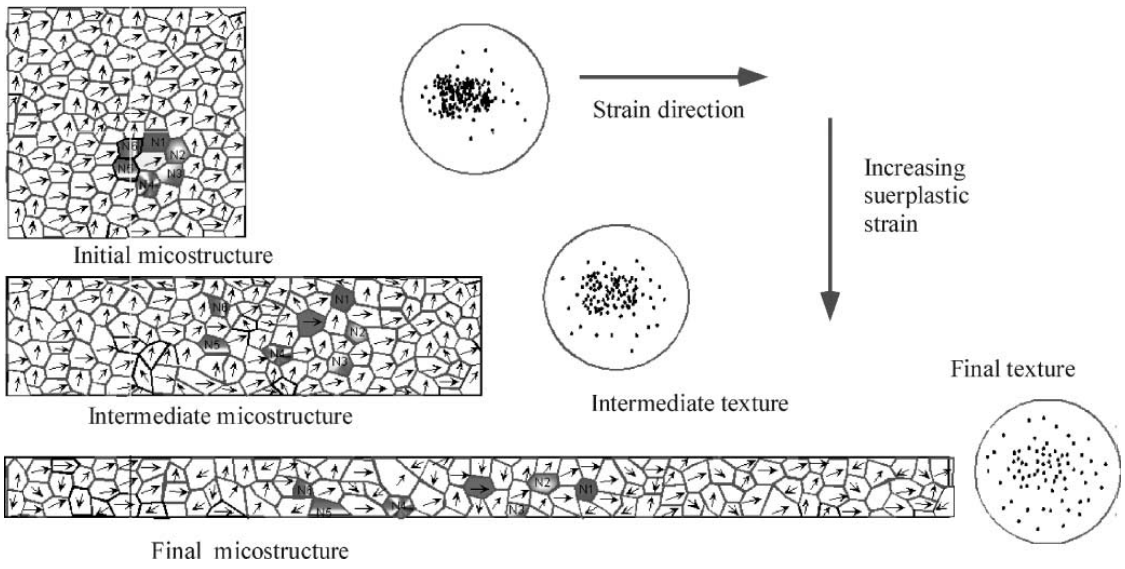

(b)

Figure 1-7 Sketch of microstructural evolution of (a) plasticity and (b) superplasticity. Taken from [2].

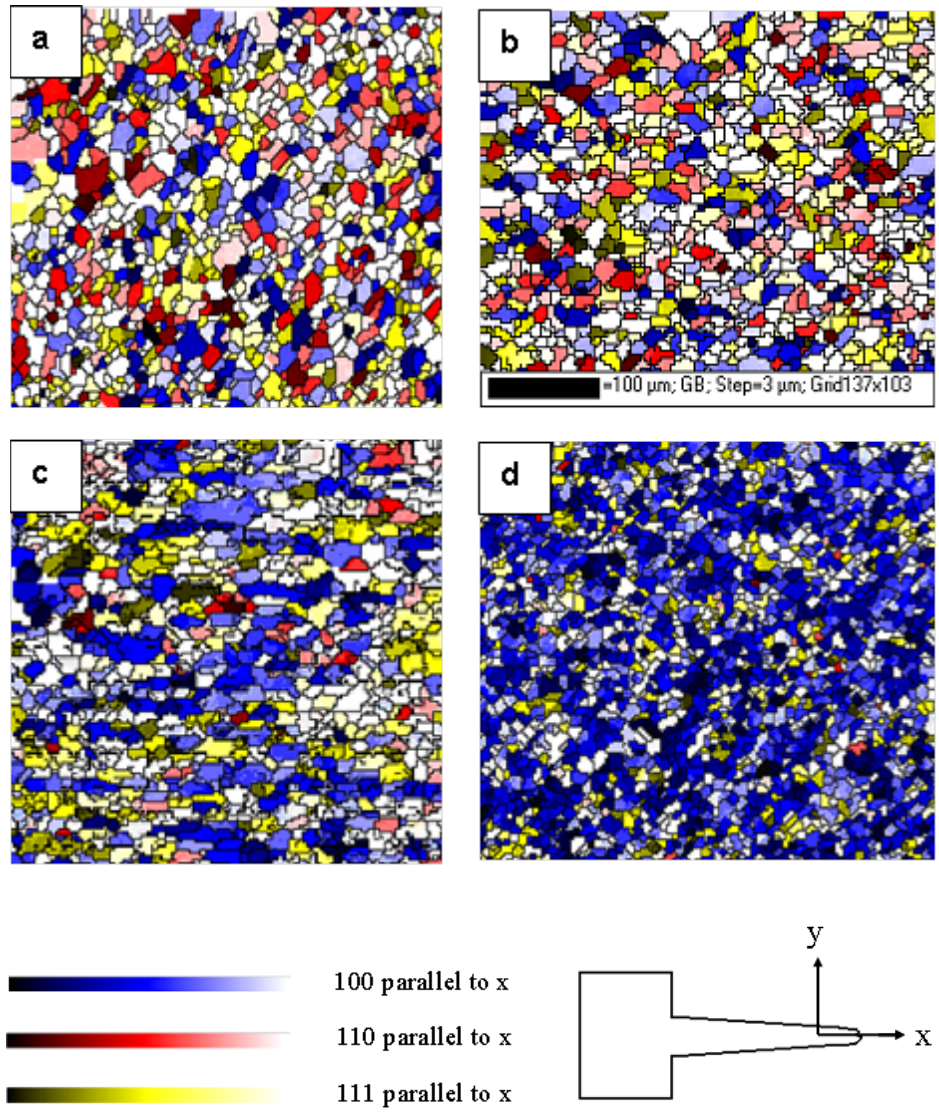

Figure 1-8 EBSD images of AA5083 samples tested at 450oC were taken from the following areas: (a) in the grip region of a sample tested at 0.3/s, (b) from the gage section of a sample tested at 0.0005/s, (c) in the gage section of a sample tested at 0.01/s, and (d) in the gage section of a sample tested at 0.3/s. Taken from [57].

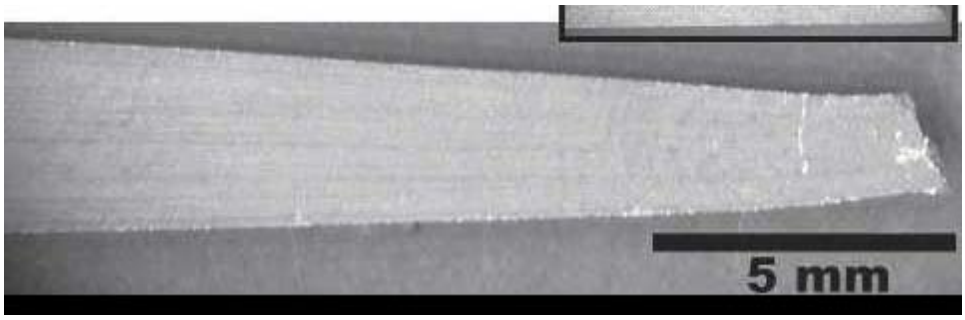

(a)

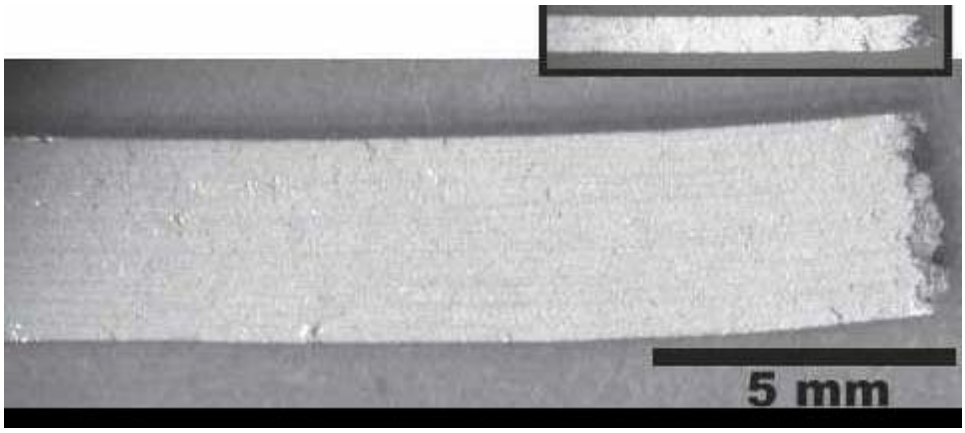

(b)

Figure 1-9 The failure regions of aluminum alloy AA5083 specimens are shown for (a) failure controlled by necking in both tensile direction and through thickness direction when deformation is by dislocation creep (T = 450ºC, $\dot{\varepsilon} = 6\times10^{-2}\text{s}^{-1}$) and (b) failure controlled by cavitation when deformation is by grain boundary sliding creep (T =450ºC, $\dot{\varepsilon} = 3\times10^{-4}\text{s}^{-1}$). Taken from [58].

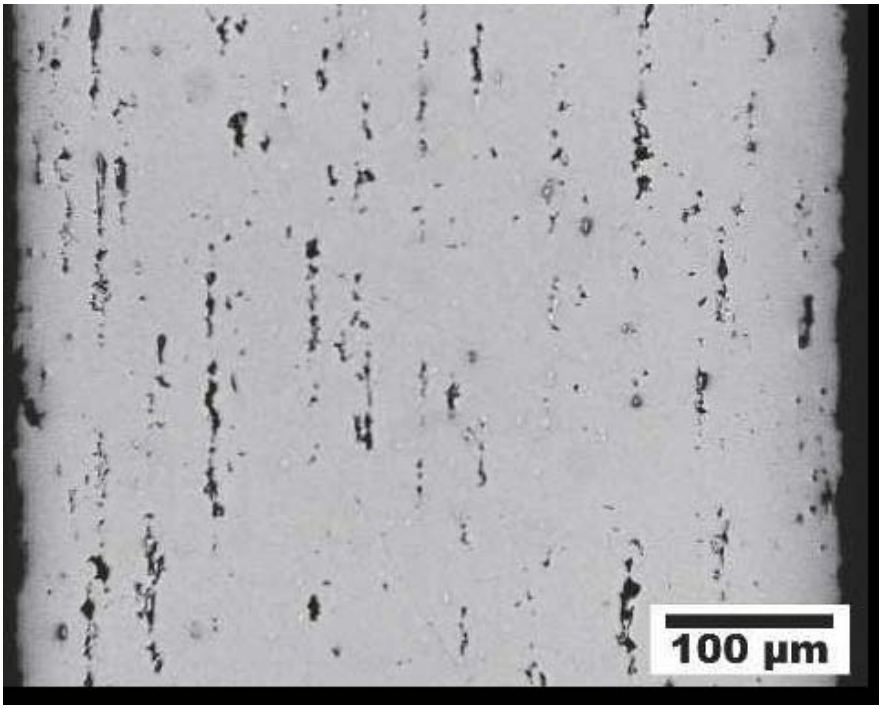

(a)

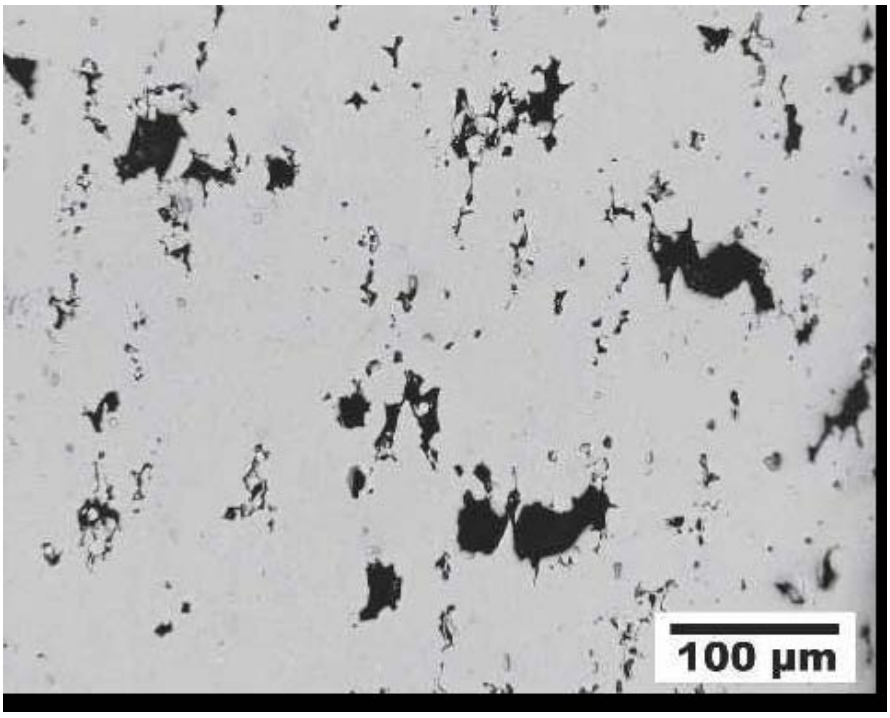

(b)

Figure 1-10 Micrographs of an Al AA5083 material show cavity morphology deformed in (a) dislocation creep regime (T = 450ºC, $\dot{\varepsilon} = 3\times10^{-2}\mathrm{s}^{-1}$) and (b) grain boundary sliding regime (T = 450ºC, $\dot{\varepsilon} = 3\times10^{-4}\mathrm{s}^{-1}$). Taken from [58].

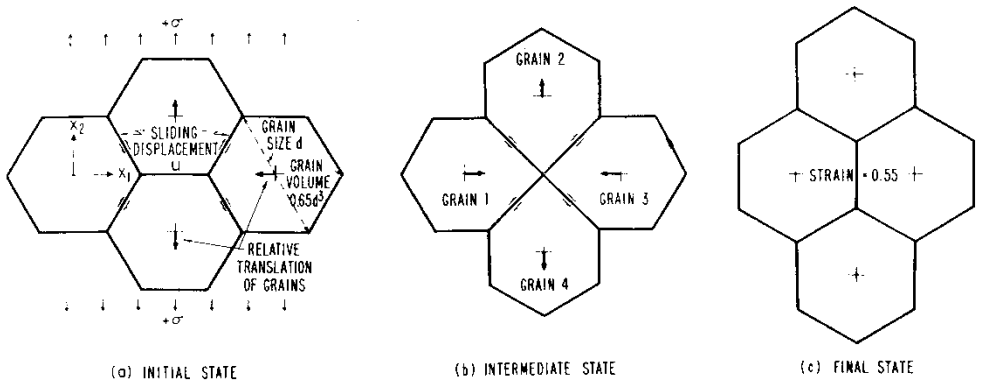

Figure 1-11 Unit step of the deformation process in a neighbor switching mechanism. A group of four grains moves from the initial, through the intermediate state to the final state. The initial and final states of the polycrystal are thermodynamically identical, although it has suffered a true strain $\varepsilon_0 = 0.55$. In so doing, the grains suffer accommodation strains and translate past each other by sliding at their boundaries [14].

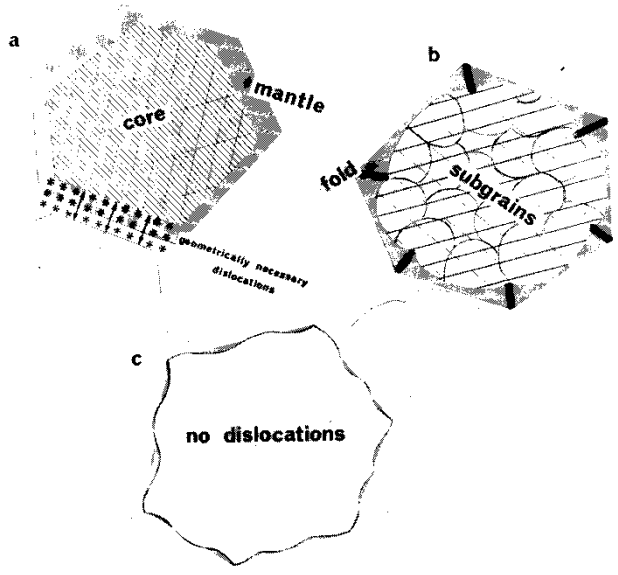

Figure 1-12 "Core and Mantle" model for the deformation of grains in a polycrystalline specimen showing the effect of decreasing stress (or strain rate) upon the nature and proportion of these two zones [23]. The stress decreases in the order of a, b, and c.

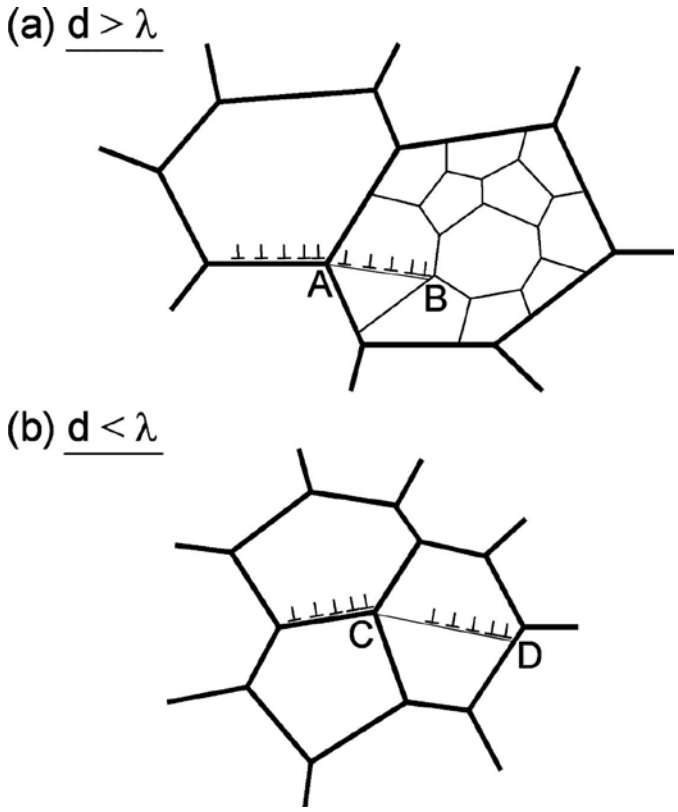

Figure 1-13 A unified model for Rachinger grain boundary sliding under (a) conventional creep conditions when d > λ and (b) superplastic conditions when d < λ .[27].

Chapter 2: Microstructural Finite Element Model for Superplasticity

A suitable model is the key to understand the deformation and failure mechanisms of superplastic materials. Early works towards developing the constitutive models for superplastic materials in the past few decades are mostly focused on developing rate equation for superplasticity to model region II of the superplastic stress-strain rate curve, where grain boundary sliding is believed to be the main deformation mechanism. A number of models were proposed based on different postulated grain boundary sliding mechanisms including grain boundary sliding accommodated by diffusion [13, 14, 16, 17, 29] and grain boundary sliding accommodated by dislocation slip [18-25, 27, 59]. These models often are derived from a volumetric approximation of the creep rate and include some microstructural quantities, such as grain size and Burger's vector. These models give great insight to the mechanism of grain boundary sliding and superplasticity. Each model has its own strength and weakness, and some models give satisfactory comparison to experiments. However, the nonhomogeneity of superplastic flow at grain level is ignored in these models and the microstructure is reduced to a main grain diameter. Recent experiments have shown that in superplastic material the amount of grain boundary sliding depends on the nature of the individual grain boundaries and the microstructure, hence the deformation in superplastic materials is highly nonhomogenous.

Furthermore, most of the models are focused on region II of the superplastic stress-strain rate curve and thus cannot be directly used in prediction of the whole stress-strain rate curve within a wide range of strain rate and cannot predict the mechanism transition.

To describe the effect of grain level heterogeneities such as grain size distribution or texture evolution, microstructural models that are able to take detailed microstructure features such as crystallographic orientation of the grains, grain shape, grain size distribution and nature of individual grain boundaries into account are needed. These microstructure models for superplastic flow are relatively rare in the literature, partly because the complexity of mechanisms of superplastic flow, and partly because the difficulty of treating grain boundaries. Chandra and coworkers [60-64] recently developed a self-consistent micromechanical model which computes the strain fields of individual grains depending on their crystallographic orientation. In this model each grain is considered as an inclusion embedded in a matrix. Blandin and Dendievel [65] proposed a mesoscale model that assumes the macroscopic deformation of a given microstructure is resulted from shear of groups of grains with the axis goes through them that is 45 degree to the tension axis. They found that different macroscopic behaviors depending on the grain size distribution as well as the degree of dispersion of large grains through the material. Pan and Cocks [66] developed a numerical procedure to simulate the grain structure evolution of fine grain materials during superplastic deformation. The simulations are able to capture the main characteristics of microstructural evolution in fine grain materials during superplastic deformation and the grain shape is essentially preserved, remaining equiaxed after a 100% elongation. Onck and van der Giessen [67] studied the effect microstructural variation by changing grain shape on the creep rate of a

solid that is made up of an assembly of hexagonal grains. The grains that are homogenous power law creeping solids and the grain boundaries, which are treated with special grain boundary elements, are capable of free sliding. They found that free grain boundary sliding renders the material to be highly sensitive to microstructural variation-random microstructural variation relative to regular hexagonal grains invariably leads to an increase of the enhancement of creep rate due to sliding. Simone et al [68] presented a generalized finite element method for the analysis of polycrystals with explicit treatment of grain boundaries which are inserted into finite elements by exploiting the partition of unity property of finite element shape functions.

Recently, Bower and Wininger [54] developed a two dimensional microstructure based finite element model that rigorously accounts for fully coupled grain interior dislocation creep, grain boundary diffusion and grain boundary sliding. It is capable of predicting the constitutive relation of the superplastic deformation based on a microstructure, tracing the microstructural evolution of the material during the deformation and computing the contribution of each deformation mechanism to the total plastic stain. These capabilities enable us to look for the initial microstructure that produces the desired formability of the material.

The model was initially developed for two dimensional plain strain deformation and was used to predict the effect of microstructure or microstructural quantities on the constitutive relation of the material ([69], Chapter 3, [70]) and void growth in superplastic materials (Chapter 4). A detailed large deformation description of the model with the description of a method to update the microstructure change in the solid can be found in Bower and Wininger [54]. This chapter will give a small strain description of

the Bower-Winnger model expanded to three dimensions. The finite element model serves as a tool to study the deformation and failure mechanisms of superplastic material in this dissertation, but its capabilities are not limited to superplastic materials. An example of the application of the three dimensional model will be given at the end of this chapter to demonstrate the capability model beyond the scope of this dissertation.

1.4 Finite Element Method Formulation

The model idealizes a polycrystal as an assembly of grains, separated by sharp grain boundaries that are mobile due to microstructure change, as illustrated in Figure 2-1. Plasticity in the solid occurs by three fully coupled mechanisms: the dislocation activities within the grains, grain boundary diffusion and grain boundary sliding. Inside the grains, plastic deformation occurs by the slip of lattice dislocations. Each grain is modeled as a single crystal, for example, to model Al each grain is a centered cubic single crystal with twelve (111) [110] slip systems. The plastic deformation of the polycrystal can also occur by grain boundary diffusion, ie, Coble creep. The grain boundaries provide a path for stress driven mass transport. A third contributor to the total plastic deformation of the polycrystal is grain boundary sliding, which is defined as the relative displacement of adjacent grains in the tangential direction of the grain boundaries due to the resolved shear stress on the boundary. The three deformation mechanisms will be described respectively in the following.

1.4.1 Intragranular Dislocation Creep

The grains themselves are idealized as elastic-plastic single crystals deformed by dislocation creep. In general random orientations are assigned to the polycrystal as the initial texture. The standard crystal plasticity constitutive law is adopted here to model the thermally activated dislocation creep within the grains. The total strain rate in the solid is decomposed into elastic and plastic parts,

$$\dot{\varepsilon}_{ij} = \dot{\varepsilon}^e_{ij} + \dot{\varepsilon}^p_{ij} . \tag{2.1}$$

The elastic strain rate is related to the Cauchy stress rate through the linear elastic constitutive equations,

$$\dot{\varepsilon}^e_{ij} = C_{ijkl}\dot{\sigma}_{kl} . \tag{2.2}$$

The plastic strain rate is the sum of the shearing rate on all of the slip systems within the single crystal,

$$\dot{\varepsilon}^p_{ij} = \sum_{\alpha=1}^{N} \dot{\gamma}^\alpha (q^\alpha) \frac{1}{2}\left(s^\alpha_i m^\alpha_j + m^\alpha_i s^\alpha_j \right), \tag{2.3}$$

where $\dot{\gamma}^\alpha$ is the shear rate on slip system α, N is the number of slip systems, s^α_i and m^α_i denote the slip direction and slip plane normal, and q^α is the resolved shear stress, $q^\alpha = s^\alpha_i \sigma_{ij} m^\alpha_j$. There are numerous models for dislocation creep that describes the relation between $\dot{\gamma}^\alpha$ and q^α, among which is the traditional creep laws of thermally dislocation climb-plus-glide proposed by Frost and Ashby [71] ,

$$\dot{\gamma}^\alpha = \dot{\gamma}_0 sign(q^\alpha) \left(\frac{q^\alpha}{\tau_0} \right)^2 \exp\left[-\frac{\Delta\Psi}{kT} \left\{ 1 - \left(\frac{|q^\alpha|}{\tau_0} \right) \right\} \right], \tag{2.4}$$

where, $\dot{\gamma}_0$ is a characteristic slip rate, τ_0 is the slip system strength, $\Delta\Psi$ is the activation energy for dislocations to escape pinning points, T is the temperature and k is the Boltzmann constant. The activation energy varies with temperature as

$$\Delta\Psi = \Delta\Psi_0\left(1+\frac{300-T}{2T_M}\right), \tag{2.5}$$

where, T_M is the solid's melting temperature, and $\Delta\Psi_0$ is the activation energy at $T = 300\text{K}$.

The above creep law is used in the calculations of chapter 2. Later in Chapter 4 and Chapter 6 we switched to a power-law relationship between $\dot{\gamma}^\alpha$ and q^α to better approximate the solute drag behavior in aluminum alloy AA 5083,

$$\dot{\gamma}^\alpha = \dot{\gamma}_0\left(\frac{q^\alpha}{\tau_0}\right)^\Lambda, \tag{2.6}$$

where $\dot{\gamma}_0$ is a characteristic shear strain rate, τ_0 is a flow stress, and n is the stress exponent.

Strain hardening is ignored in all the calculations .

1.4.2 Grain Boundary Diffusion

The chemical potential that drives the mass diffusion along the grain boundaries is approximated by

$$\mu = -\Omega\sigma_n, \tag{2.7}$$

where Ω is the atomic volume and σ_n is the normal stress acting on the grain boundary plane. Grain-boundary diffusion is thus driven by the gradient of the normal stress in the grain boundary plane and the diffusional flux is given by the Fick's law,

$$\mathbf{j} = -\frac{\delta D_0 \exp(-Q_{GBD}/kT)}{kT}\nabla_s \mu = \frac{\delta D_0 \exp(-Q_{GBD}/kT)}{kT}\nabla_s \sigma_n, \qquad (2.8)$$

where $D_0 \exp(-Q_{GBD}/kT)$ is the grain boundary diffusivity, δ is the thickness of the layer in which diffusion is assumed to take place, k is the Boltzmann constant, T is the temperature, and ∇_s denotes the gradient in the grain boundary plane.

In the grain boundary diffusion process, atoms detach from regions of the grain boundary that are subjected to compressive stress and migrate to regions that are under tensile stress so as to reduce the total free energy of the system. This causes a discontinuity in the velocity field across the grain boundaries: material points in the grains adjacent to the boundary approach one another in regions of compressive stress and separate in regions of tensile stress. The velocity discontinuity resulted from grain boundary diffusion is normal to the grain boundary and is given by the law of mass conservation,

$$[v_n] = \left(\dot{u}_i^+ - \dot{u}_i^-\right) n_i = -\nabla_s \cdot \mathbf{j}, \qquad (2.9)$$

where $\dot{u}_i^+$ and $\dot{u}_i^-$ are the velocity of the material points belong to the adjacent grains (+) and (-) respectively, and n_i is the normal vector of the grain boundary. The velocity discontinuity is thus related to normal grain boundary stress by substituting (2.8) into (2.9)

$$[v_n] = \left(\dot{u}_i^+ - \dot{u}_i^-\right) n_i = -\frac{\Omega \delta D_0 \exp(-Q_{GBD}/kT)}{kT}\nabla_s^2 \sigma_n. \qquad (2.10)$$

The above equation will be used as one of the constraints on the grain boundary displacement/velocity discontinuity in the finite element method.

The mass flux can be exchanged between grain boundaries through the triple junctions or between grain boundary and free surfaces through the surface junctions in the polycrystal. At the triple grain junctions, the normal stress acting on the three grain boundaries that meet at the junction must be equal, to satisfy continuity of chemical potential. Similarly, the normal stress acting on grain boundaries that terminate at a free surface (such as a void surface) is related to the curvature of the surfaces.

1.4.3 Grain Boundary Sliding

The grain boundaries allow neighboring grains to slide relative to one another in response to a shear stress. Similar to grain boundary diffusion, grain boundary sliding causes velocity field discontinuities that are tangential to the grain boundaries in the polycrystal. We assume that grain-boundary sliding is a thermally-activated process and a linear-viscous constitutive equation is used to relate the relative sliding velocity of two adjacent grains to the resolved shear stress along the grain boundaries:

$$\left[v_t\right] = (\dot{u}_i^+ - \dot{u}_i^-)t_i = \frac{\Omega v_0 \exp(-Q_{GBS} / kT)}{kT}\tau \qquad (2.11)$$

where t_i is the components of the unit vector along the direction of the resolved shear stress in the grain boundary plane, $\eta_0 = \Omega v_0 \exp(-Q_{GBS} / kT)/kT$ is the grain boundary fluidity (the inverse of the grain boundary viscosity), v_0 is a characteristic sliding velocity, and Q_{GBS} is the activation energy for grain boundary sliding, and $\tau = \left|\boldsymbol{\sigma n} - \boldsymbol{n}\boldsymbol{\sigma n}\right|$ is the magnitude of the resolved shear traction acting on the grain boundary plane.

1.4.4 Mechanical Equilibrium

Consider a polycrystal with volume V subjected to traction p_i^* prescribed on boundary $(\partial V)_p$ and prescribed velocity (displacement) elsewhere on the boundary. The objective is to solve the velocity **v** that is continuous within the grains and is discontinuous across the grain boundaries Γ. The virtual work principle that is generalized to include velocity discontinuity across the grain boundaries due to grain boundary diffusion and grain boundary sliding is,

$$\begin{aligned}&\int_{V_t}\sigma_{ij}\delta v_{i,j}\mathrm{d}V-\int_{(\partial V_t)^*}p_i^*\delta v_i\mathrm{d}A+\int_{\Gamma_t}\sigma_n(\delta v_i^+-\delta v_i^-)n_i\mathrm{d}A\\&+\int_{\Gamma_t}\tau_\alpha(\delta v_i^+-\delta v_i^-)t_i^\alpha\mathrm{d}A=0\\&(\alpha=1,2)\end{aligned}\qquad(2.12)$$

where t_i^α ($\alpha=1,2$) are two arbitrary but orthogonal tangential unit vectors in the grain boundary plane, τ_α is the resolved shear stress in t_i^α.

The above equation is further modified to enforce the constraints of grain boundary diffusion (2.10) and grain boundary sliding (2.11) as Lagrange multiplier,

$$\begin{aligned}&\int_{V_t}\sigma_{ij}\delta v_{i,j}\mathrm{d}V-\int_{(\partial V_t)^*}p_i^*\delta v_i\mathrm{d}A+\int_{\Gamma_t}\sigma_n(\delta v_i^+-\delta v_i^-)n_i\mathrm{d}A+\int_{\Gamma_t}\tau_\alpha(\delta v_i^+-\delta v_i^-)q_i^\alpha\mathrm{d}A\\&+\int_{\Gamma_t}\left[(v_i^+-v_i^-)n_i+\frac{\Omega D_0\delta\exp(-Q_{GBD}/kT)}{kT}\nabla_s{}^2\sigma_n\right]\delta\sigma_n\mathrm{d}A\\&+\int_{\Gamma_t}\left[(v_i^+-v_i^-)q_i^\alpha-\frac{\Omega\eta_0\exp(-Q_{GBS}/kT)}{kT}\tau_\alpha\right]\delta\tau_\alpha\mathrm{d}A=0\end{aligned}\qquad(2.13)$$

Using $(\nabla_s{}^2\sigma_n)\delta\sigma_n=\nabla_s\cdot(\sigma_n\delta\sigma_n)-\nabla_s\sigma_n\cdot\nabla_s\delta\sigma_n$ and applying divergence theorem on the above equation we obtain

$$
\begin{aligned}
&\int_V \sigma_{ij}\delta v_{i,j}\mathrm{d}V - \int_{(\partial V)^*} p_i^*\delta v_i \mathrm{d}A + \int_\Gamma \sigma_n(\delta v_i^+ - \delta v_i^-)n_i \mathrm{d}A + \int_\Gamma \tau_\alpha(\delta v_i^+ - \delta v_i^-)t_i^\alpha \mathrm{d}A \\
&+\int_\Gamma (v_i^+ - v_i^-)n_i\delta\sigma_n \mathrm{d}A + \oint_{\partial\Gamma} j_i n_i^s \delta\sigma_n \mathrm{d}s \\
&-\int_\Gamma \frac{\Omega D_0 \delta \exp(-Q_{GBD}/kT)}{kT}\nabla_s\sigma_n\cdot\nabla_s\delta\sigma_n \mathrm{d}A \\
&+\int_\Gamma \left[(v_i^+ - v_i^-)t_i^\alpha - \frac{\Omega\eta_0\exp(-Q_{GBS}/kT)}{kT}\tau_\alpha\right]\delta\tau_\alpha \mathrm{d}A = 0
\end{aligned}
\tag{2.14}
$$

where $\partial\Gamma$ denotes the edge of the grain boundary faces and n_i^s is the normal of the edge.

Equation (2.14) is then solved using finite element discretization for the velocity (displacement) field v_i together with the grain boundary stresses (σ_n, τ_α). To do this, two kinds of elements are used to mesh the polycrystal. The grains themselves are meshed with 6 noded triangles elements (in two dimension) or 8 noded bricks elements (in three dimensions). These elements only have the displacement degree of freedoms. After the grains are meshed, extra nodes are added to generate the interface elements. Figure 2-2 shows a sketch of the interface element in three dimensions. Each hybrid element contains 12 nodes and can be divided into three layers. 8 of them are displacement nodes in the upper and lower layers connected to either the upper or lower grain. The 4 nodes in the middle layer are stress nodes and have normal and shear grain boundary stress as their degree of freedoms. All three layers are coinciding in space, hence, no thickness for the interface element.

1.4.5 Strain Rate Computations

A principal goal of our computations is to calculate the contribution to the total strain rate from each of the three possible mechanisms (dislocation creep, grain boundary

sliding, and diffusion) that can contribute to plastic flow. This is done after obtaining the solution of the boundary value problem in the above section. The contributions can be computed from the relative velocity of sliding and separation on grain boundaries and the shearing rates on the slip systems within the grains. By definition

$$\dot{\varepsilon}_{ij}^{sliding} = \frac{1}{V}\int_{\Gamma}[v_t]\frac{1}{2}\left(n_i t_j + t_i n_j\right)\mathrm{d}A \qquad \dot{\varepsilon}_{ij}^{diffusion} = \frac{1}{V}\int_{\Gamma}[v_n]n_i n_j \mathrm{d}A$$
$$\dot{\varepsilon}_{ij}^{plastic} = \frac{1}{V}\int_{V}\sum_{\alpha}\dot{\gamma}^{\alpha}\frac{1}{2}(s_i^{\alpha}m_j^{\alpha} + s_j^{\alpha}m_i^{\alpha})d\ V \qquad . \qquad (2.15)$$

1.5 An Application of the 3D Model: Sn Whisker Growth

This section gives an example to illustrate the capability of the finite element model of coupled grain interior plasticity and grain boundary diffusion/sliding. The above model is used to investigate the growth of Sn whisker from the surface of Sn thin film coated on Cu substrate [72]. This thin film structures is widely used in electronic conductors and the growth of the whiskers can pose a serious threat to the reliability of electronic components. It is generally accepted that whiskers form to relax compressive stress generated by nucleation and growth of Cu/Sn intermetallic compound (IMC) within the Sn film [72]. However it is unclear why whiskers still form even when another stress relaxation mechanism, dislocation activities of the Sn grains, is active.

We proposed a model of whisker growth by adding periodic distribution of 'soft' grains in the Sn thin film, which is illustrated in Figure 2-3. The polycrystalline Sn film is modeled as a collection of periodic hexagonal columnar grains. The length of hexagon side is L, and thickness of the film is h_f. The grains themselves are deformed

plastically and diffusion occurs along the grain boundaries. Each grain is modeled as isotropic elastic-plastic solid with Young's modulus E, Poisson's ratio ν. Within each unit cell, a grain with plastic yield stress, σ_w, which is lower than the yield stress of the surrounding grains, σ_y, is placed in the center. The film is subjected to a uniform volumetric compressive strain rate, $\dot{e}$, to mimic a thermal strain rate or the volumetric strain rate generated by Cu/Sn IMC growth. The lower face of the film is bonded to the substrate, and the upper face is assumed to be passivated by oxidation (no surface diffusion occurs). Room temperature deformation is considered. The value of the parameters used in the simulation is listed in Table 2-1. During the deformation, stress gradient formed around the soft grain. This drives the material flux toward the soft grain from the surrounding grains. The soft grain is observed to be extruded from the film to form whiskers due to the mass accumulation, seen in Figure 2-3. The extruded height of the whisker grain represents the amount of strain accommodated by whisker growth. This amount increases as the applied strain rate decreases. Stress relaxation due to whisker growth results in a region with no plastic strain. At fast strain rate (Figure 2-3a), the film is overall yielded and the whisker growth relaxes plastic strain only in the immediate neighboring grains of the whisker. As strain rate increases (Figure 2-3b), the radius of stress relaxation increases and the whole film is relaxed by whisker growth with sufficiently low strain rate (Figure 2-3c).

The normalized whisker growth rate, $\mathrm{d}\tilde{h}/\mathrm{d}e$, as a function of $\eta \equiv (kTL^3\dot{e})/(\Omega\delta D_{gb}\Delta\sigma_y)$, for three different whisker density ρ_w in Figure 2-4. Note that η represents the comparison of applied strain rate to the diffusivity of the film. The dash

lines are from finite element simulations and the solid line is from an analytical solution from [72]. The growth rate of the whisker is independent of the whisker density when the applied strain rate is large compared to the diffusivity (large η, or fast IMC growth). The growth rate increases as η decreases until the relaxation radius by grain boundary diffusion is large enough to cover the entire film.

1.6 Summary and conclusions

A finite element method rigorously accounts for the grain interior plasticity, grain boundary diffusion and grain boundary sliding is given in this chapter. The method can be used to predict the constitutive response and microstructure evolution during deformation due to coupled mechanisms based on microstructural simulations. It can also be used to predict the contribution of each mechanism to the total plastic strain. The model is extensively used in the study of deformation and failure mechanisms of superplastic materials in the subsequent chapters of this dissertation. The two dimensional Bower-Wininger model is expanded and implemented in three dimension and The application of the finite element model on the growth of Sn whiskers on Cu substrates is also given as an example to demonstrate the capabilities of the finite element model beyond superplastic deformation.

Table 2-1 Parameters used in the simulations of whisker growth.

Parameter Name	**Value**
Grain size L	1.0 μm
Film thickness h_f	2.0 μm
Young's modulus E	50 GPa
Poisson's ratio ν	0.36
Temperature T	300 K
Yield stress σ_y	15 Mpa
Yield stress of whisker grains σ_w	13.5 MPa
Grain boundary diffusivity D_{gb}	4.3×10^{-9} cm^2s^{-1}
Grain boundary thickness δ	5×10^{-10} m
Atomic volume Ω	2.7×10^{-29} m^3

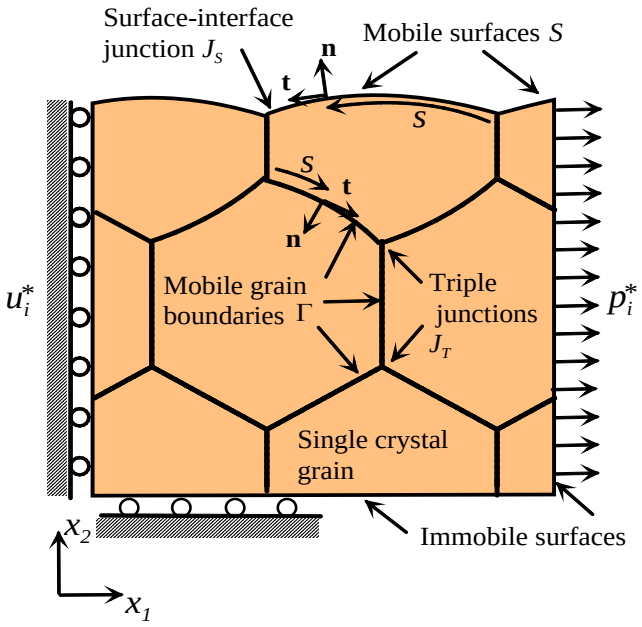

Figure 2-1 A two dimensional sketch of the finite element model. The solid is idealized as an assembly of grains separated by sharp grain boundaries. The grains themselves are modeled as single crystals, and the grain boundaries are capable of diffusion and sliding.

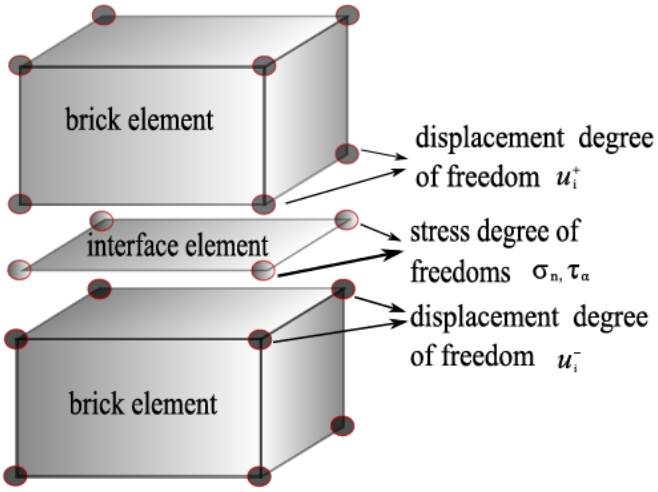

Figure 2-2 A schematic of interface element in three dimension. Each interface element contains 12 nodes and can be divided into three layers. 8 of them are displacement nodes in the upper and lower layers connected to either the upper or lower grain. The 4 nodes in the middle layer are stress nodes and have normal and shear grain boundary stress as their degree of freedoms.

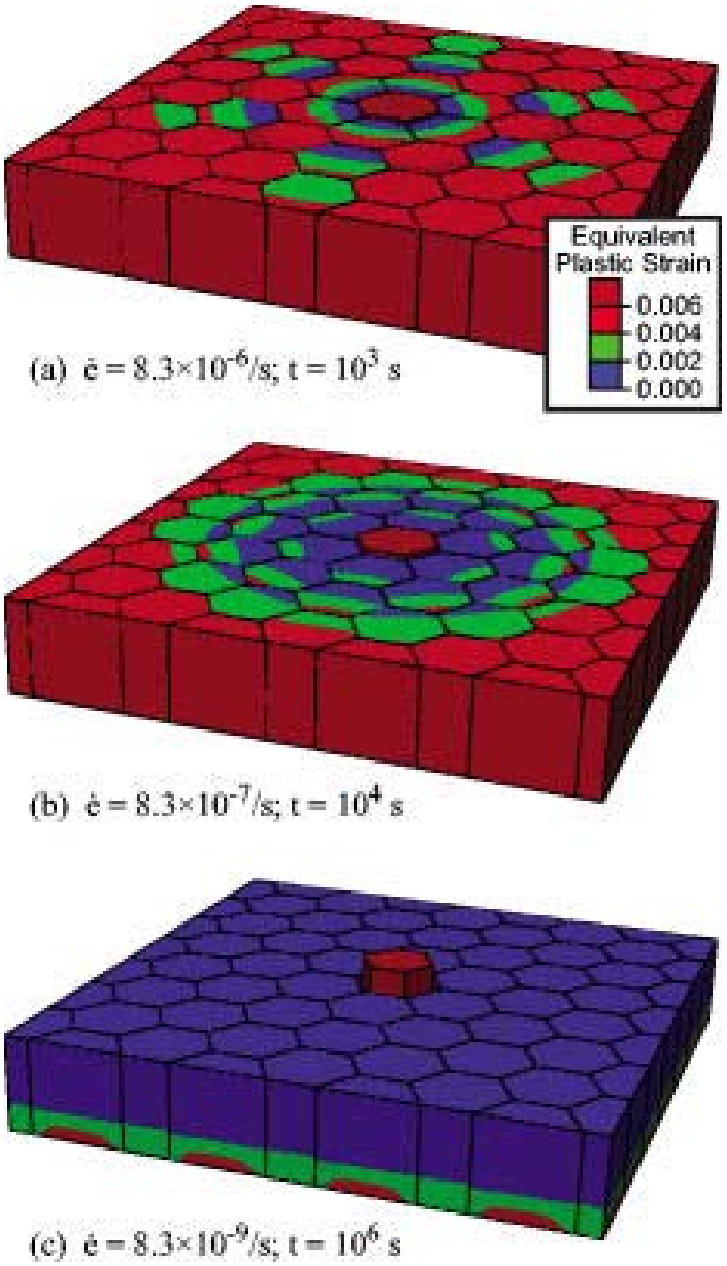

Figure 2-3 Distribution of plastic strain surrounding the whisker grain during steady state growth. The periodic cell surrounding a single whisker grain is shown. The rate of applied strain decreases from (a) to (c) but all three plots are snapped at the same strain. (Taken from [72]).

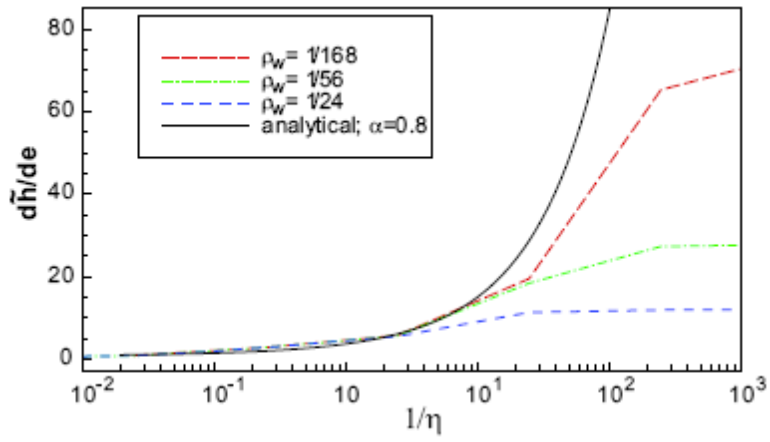

Figure 2-4 Normalized whisker growth rate as a function of $\eta \equiv (kTL^3\dot{e})/(\Omega\delta D_{gb}\Delta\sigma_y)$. Note that the applied strain rate decreases from left to right. (taken from [72]).

Chapter 3: Effect of A Threshold Stress for Grain Boundary Sliding on Constitutive Response of Al AA5083 at Elevated Temperature

The model described in Chapter 2 was calibrated by experimental data for aluminum alloy 5083. The finite element model itself can be applied to a variety of materials but 5083 is chosen because it is the most widely used material in quick plastic forming.

The finite element model is calibirated by the experimental data of AA 5083 of a 7 micron grain size at temperature of 450°C measured by Kulas et al [73]. Most of the parameters in the model, including the atomic volume, elastic constants, slip system strength and grain boundary diffusion activation energy are taken from standard references. The sliding fluidity η_0 of the grain boundaries was estimated using the Raj-Ashby model [13] of grain boundary sliding. This leaves four parameters to fit the experimental data: the grain boundary diffusion pre-exponential D_0, the characteristic slip rate $\dot{\gamma}_0$ together with the slip strength τ_0 in the slip law (these two are not independent). These parameters were chosen so that the simulations match the experiments in two aspects:

1. The simulations match the variation of flow-stress with strain rate measured in polycrystalline AA5083 with a 7micron grain size (shown in Figure 3-2). The data

showed a standard power-law relation between strain rate and stress of the form $\dot{\varepsilon} = A\sigma^n$ where A and n are functions of strain rate and grain size. For a fixed grain size of approximately 7 μm and temperature of 450°C, it was observed that at slow strain rates ($\dot{\varepsilon} < 10^{-3} s^{-1}$), the stress exponent has a value $n \approx 2.7$, while at fast strain rates ($\dot{\varepsilon} > 10^{-3} s^{-1}$), $n \approx 4$.

2. The simulations predict a transition in deformation mechanism from grain boundary sliding creep to dislocation creep at a strain rate of $10^{-3}s^{-1}$ for the material with 7 micron grain size, in order to match the texture observations of Agarwal et al. [74]. Measurements of texture evolution at various strain rates showed that at strain rates below 10^{-3} s^{-1} the texture remains random while at strain rates above 10^{-3} s^{-1} a strong texture develops, suggesting a transition in deformation mechanism at a strain rate around 10^{-3} s^{-1}.

Agarwal et al [57] systemically compared the predictions of the Bower-Wininger model with experimental measurements of plastic flow in 5083 under quick plastic forming conditions. The model was found to predict behavior that was in good qualitative and quantitative agreement with experimental data. In particular, (i) the simulations predicted a transition in deformation mechanism from grain-boundary-diffusion-mediated sliding at slow strain rates, to solute drag dislocation creep, assisted by grain-boundary sliding, at fast strain rates; (ii) the model correctly predicted the influence of grain size on both the mechanism transition and the strain rate sensitivity of the solid; and (iii) the model predicted a transition in rate sensitivity with strain rate that qualitatively matched the experimental measurements. However, as shown in Figure 3-2, simulations were found to substantially over estimate the strain rate sensitivity of the

solid at low strain rates, giving a strain rate exponent that was higher than the experimental value.

The most likely explanation for this discrepancy between theory and experiment is that the simulations over-simplified the sliding response of grain boundaries. The model used a simple linear viscous relation between the sliding velocity and resolved shear stress. However, both experiments [47] and atomic-level simulations [32] suggest that the behavior of actual grain boundaries is significantly more complex. In particular, there is strong (direct and indirect) experimental evidence to suggest that there is a threshold stress for grain boundary sliding [47, 55, 56, 75]. Similarly, molecular dynamics simulations of grain boundaries show that sliding occurs only if the resolved shear stresses exceed a critical magnitude [32]. Estimates of the threshold stress for grain boundary sliding vary, and suggest it is a function of temperature, grain size and grain boundary misorientation.

In this chapter, our objective is to extend the finite element model of Bower and Winiger to include a threshold stress for grain boundary sliding, and to compare the predictions of the extended model with experimental data. We find that even a small threshold stress (1MPa) substantially increases the flow stress at low strain rates, and also reduces the strain rate sensitivity. As a result, the model predictions are in agreement with experimental data over the full range of strain rate.

1.7 Simulation Procedures

A microstructure containing 18 grains as illustrated in Figure 3-1 was used in the simulations. The model idealizes a polycrystal as an assembly of grains, separated by sharp grain boundaries. The grain structure was taken from a section through a representative sample of AA5083 with 7 μm grain size – the microstructure is identical to that used in the simulations reported by Agarwal et al [57]. Each grain is modeled as a face centered cubic single crystal. The grain boundaries permit sliding, and also provide a path for stress driven mass transport. The material is subjected to boundary loading that is intended to approximate plane-strain uniaxial tension. Symmetry conditions are applied on boundaries at $x_2 = 0$ and $x_1 = 0$; the top surface of the microstructure, $x_2 = h$, is taken to be free of traction; and the solid is subjected to a constant strain rate of $\dot{\varepsilon}_{11} = \dot{\varepsilon}^{\infty}$ by displacing the boundary at $x_1 = L$.

In order to resolve the discrepancy between the simulations and experiments, we made modifications to the constitutive relation of grain boundary sliding in the model described in Chapter 2 to include a threshold stress. We assume that grain-boundary sliding is a thermally-activated process, which is driven by shear tractions $\sigma_t = \sigma_{ij} t_i n_j$ acting on the grain boundary. A linear-viscous constitutive equation with a threshold stress, instead of (2.11), is used to relate the relative sliding velocity of two adjacent grains to the resolved shear stress along the grain boundaries. In two dimension,

$$\left[v_t\right] = (\dot{u}_i^+ - \dot{u}_i^-)t_i = \frac{\Omega v_0 \exp(-Q_{GBS} / kT)}{kT}\tau_e \qquad (3.1)$$

where t_i is the components of the unit vector along the tangential direction of the grain boundary, $\eta_0 = \Omega v_0 \exp(-Q_{GBS}/kT)/kT$ is the grain boundary fluidity (the inverse of the grain boundary viscosity), v_0 is a characteristic sliding velocity, and Q_{GBS} is the activation energy for grain boundary sliding, and τ_e is the effective shear stress acting on the grain boundary. The effective shear stress is given by

$$\tau_e = \begin{cases} \tau - \sigma_{th}, & \tau \geq \sigma_{th} \\ 0, & \tau < \sigma_{th} \end{cases} \tag{3.2}$$

where τ is the magnitude of the resolved shear traction acting on the grain boundary, $\tau = \sigma_{ij} n_i t_j$, with n_i being the components of the normal unit vector to the grain boundary, and σ_{th} is the threshold stress for grain boundary sliding. A resolved stress that is lower than the threshold stress does not induce grain boundary sliding, while if the stress exceeds the threshold, the sliding velocity increases in proportion to the resolved shear stress.

In simulations without a threshold stress, Agarwal *et al* [57] showed that when representative estimates are used for v_0 and Q_{GBS} grain boundary sliding is so rapid that the constitutive behavior of the solid is insensitive to large changes in grain boundary viscosity. In contrast, our main focus in this paper is to show that the threshold stress σ_{th} has a large influence on the macroscopic constitutive behavior of the polycrystalline.

1.8 Results

Our main goal in this chapter is to show that the discrepancy between measured and predicted stress-v-strain rate behavior for AA5083 reported by Agarwal *et al* [69] can be resolved by including the effects of a threshold stress for grain boundary sliding in the computations.

To this end, Figure 3-3 (a) shows the predicted variation of flow stress with strain rate for the model microstructure in Figure 3-1, for six values of threshold stress (the remaining parameter values are listed in Table 3-1). Evidently, even a small threshold stress (1MPa) substantially increases the flow stress at low strain rates. The threshold stress has a diminishing effect at higher strain rates; for threshold stress 1 ~ 4MPa, the dominant effect is at strain rate below 1.1×10^{-3} s^{-1}. However, large threshold stress (100MPa) has influence on flow stress across the whole range of strain rate interested here. The effect of threshold stress on the stress exponent *n* is illustrated in Figure 3-3 (b). The threshold stress significantly increases the stress exponent at low strain rates, and with a threshold stress of order 3 ~ 4MPa the predicted stress exponent is close to the experimentally measured data. In addition, for threshold stress values 1 ~ 3MPa the stress exponent has a local minimum at strain rate of order $\dot{\varepsilon} \approx 10^{-4}$ s^{-1}. A similar minimum is observed in experimental data.

Figure 3-3 (c) shows the contribution to the total plastic strain rate from the three deformation mechanisms (dislocation creep, grain boundary sliding, and diffusion), for three values of threshold stress. For modest values threshold stress grain boundary sliding is the dominant deformation mechanism at low strain rates, but for strain rates

exceeding 10^{-3} s^{-1} dislocation creep dominates. Below the transition, increasing the threshold stress reduces grain boundary sliding and increases dislocation creep, without affecting the contribution to the total plastic strain from diffusion. For a sufficiently large threshold stress (100MPa), the grain boundary sliding mechanism can be totally suppressed: in this case dislocation creep is the dominant deformation mechanism for the full range of strain rates considered here.

The critical strain rate where dislocation creep gives a larger contribution to the total strain than grain boundary sliding can be taken as a rough measure of the transition between the two deformation regimes: this suggests that reducing the threshold stress from 2MPa to zero increases the critical strain rate by approximately a factor of 2. Grain boundary engineering through alloying or appropriate processing thus has the potential for increasing hot formability by promoting grain boundary sliding.

Finally, Figure 3-4 compares the measured (from Kulas et al [73]) and predicted flow stress as a function of strain rate for AA5083 specimens with 7 μm and 10 μm grain sizes, for a material with threshold stress 1 MPa and other constitutive parameters listed in Table 3-1. A threshold stress of 1MPa was found to give a good fit between theory and experiment over the full range of strain rates. The simulations slightly overestimate the strain rate sensitivity at high strain rates $\dot{\varepsilon} > 10^{-2} s^{-1}$. This is because equation (2.4) is not the most accurate representation of solute drag in AA 5083 at high strain rate. This discrepancy can easily be resolved by replacing (2.4) by a power-law constitutive relation for dislocation creep, and this was done in Chapter 4 and Chapter 6.

1.9 Conclusions

The microstructure finite element model is calibrated against the experimental measurement of Al AA5083 and used to estimate the influence of a threshold stress for grain boundary sliding on the relationship between macroscopic flow stress and strain rate for the material when subjected to plane strain uniaxial tension at 450°C. We find that:

1. As previously reported in Agarwal et al [57], the simulations predict a transition in deformation mechanism from grain boundary sliding to dislocation creep at a critical strain rate approximately $\dot{\varepsilon} \approx 5 \times 10^{-4}$ s-1.
2. The flow stress-v-strain rate predicted by our simulations conform to the standard creep law $\dot{\varepsilon} = A\sigma^n$ where A and n are functions of strain rate and grain size.
3. In the dislocation creep regime, our simulations predict a stress exponent $4 < n < 5$. In this regime, the flow stress and stress exponent are only weakly sensitive to the threshold stress for grain boundary sliding.
4. In the grain boundary sliding regime, both flow stress and stress exponent are highly sensitive to the threshold stress. A threshold stress of 2 MPa can increase the stress exponent n from 1.5 to 2.7; and increases the flow stress by a factor of 2.
5. The critical strain that leads to a transition from grain boundary sliding to dislocation creep is sensitive to the threshold stress: reducing the threshold stress from 2MPa to zero increases the critical strain rate by approximately a factor of 2.
6. When a threshold stress is included in our polycrystal model, good agreement is obtained between measured and predicted flow stress as a function of strain rate for

strain rates in the range $10^{-5} < \dot{\varepsilon} < 10^{-1}\ s^{-1}$, and resolves a discrepancy between theory and experiment reported in Agarwal et al [69].

Table 3-1 Values for material parameters used to fit experimental data with simulations.

Parameter	**Value**
Grain size L	7 or 10 μm
Atomic volume Ω	1.66×10^{-29} m^3
Melting temperature T_M	933 K
Young's modulus E	70 GN m^{-2}
Poisson's ratio ν	0.3
Shear modulus μ	26.9 GN m^{-2}
Characteristic strain rate $\dot{\gamma}_0$	0.42×10^6 s^{-1}
Slip system strength τ_0	65 MN m^{-2}
Activation energy at 300 K $\Delta\psi_0$	2.97×10^{-19} J
Grain boundary diffusion pre-exponential δD_0	9.9×10^{-14} m^3 s^{-1}
Grain boundary diffusion activation energy Q_{GBD}	1.34×10^{-19} J
Grain boundary sliding pre-exponential η_0	259.5 m s^{-1}
Grain boundary sliding activation energy Q_{GBS}	1.34×10^{-19} J

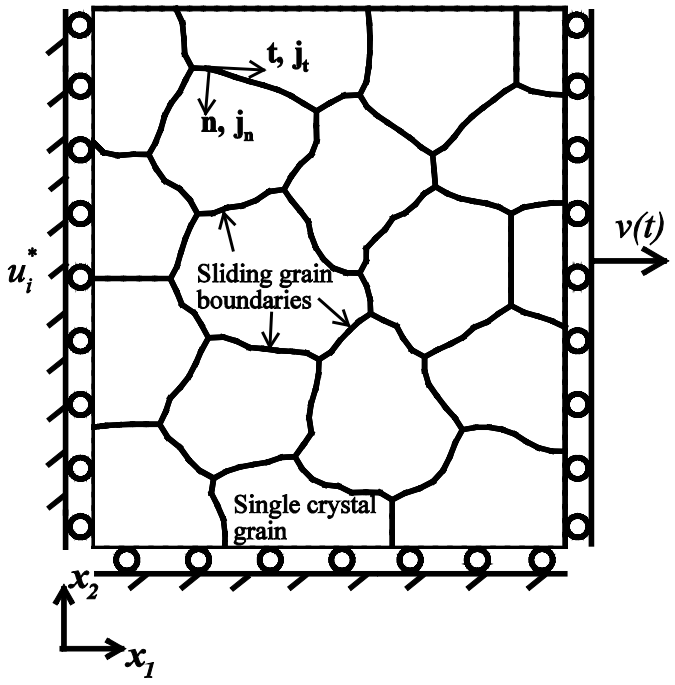

Figure 3-1 A sketch of the microstructure used in simulations.

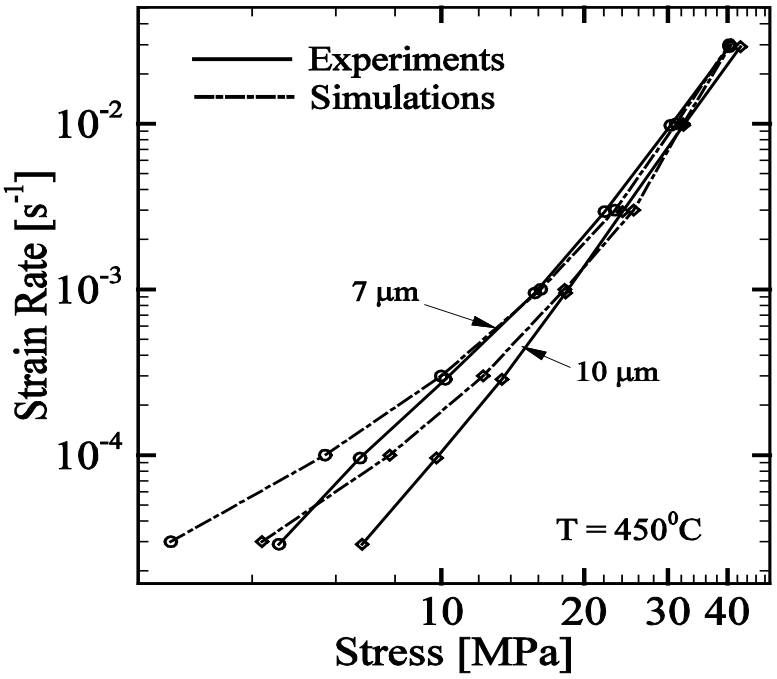

Figure 3-2 Comparison of simulations without threshold stress and experiments of flow stress as a function of strain rate. Taken from [69].

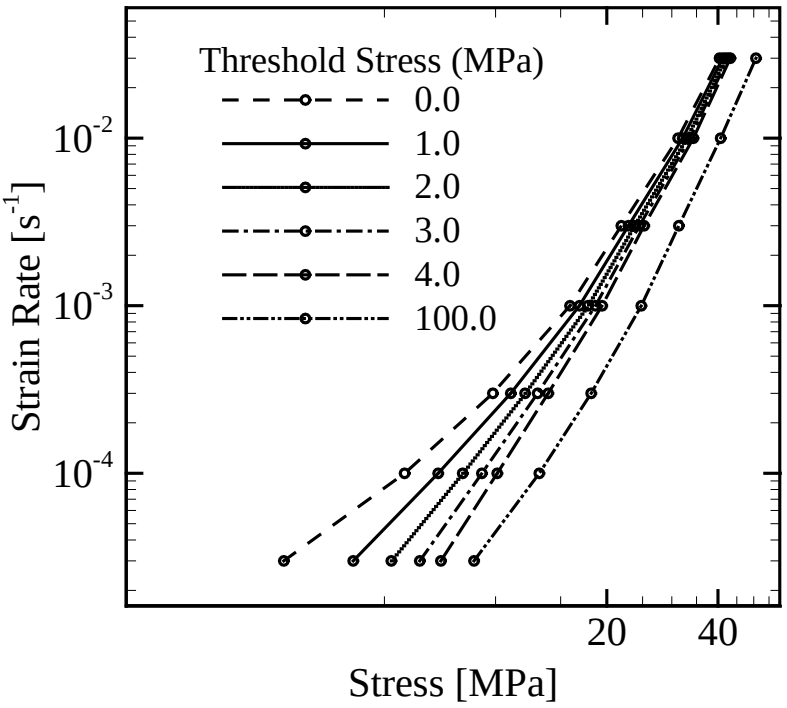
Threshold Stress (MPa)
0.0
1.0
2.0
3.0
4.0
100.0
Strain Rate [s-1]
10-2
10-3
10-4
20
40
Stress [MPa]

(a)

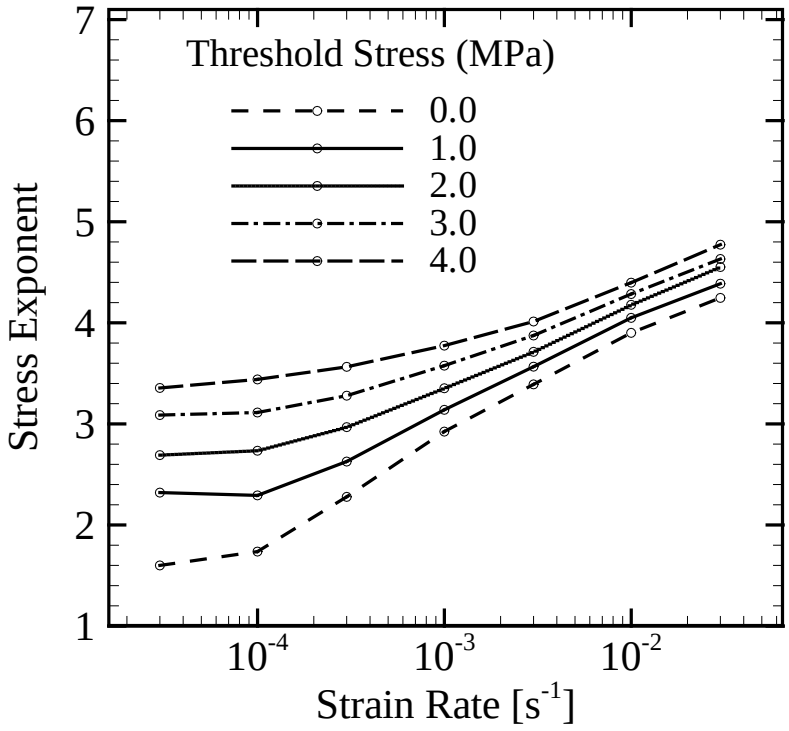
Threshold Stress (MPa)
0.0
1.0
2.0
3.0
4.0
Stress Exponent
7
6
5
4
3
2
1
10-4
10-3
10-2
Strain Rate [s-1]

(b)

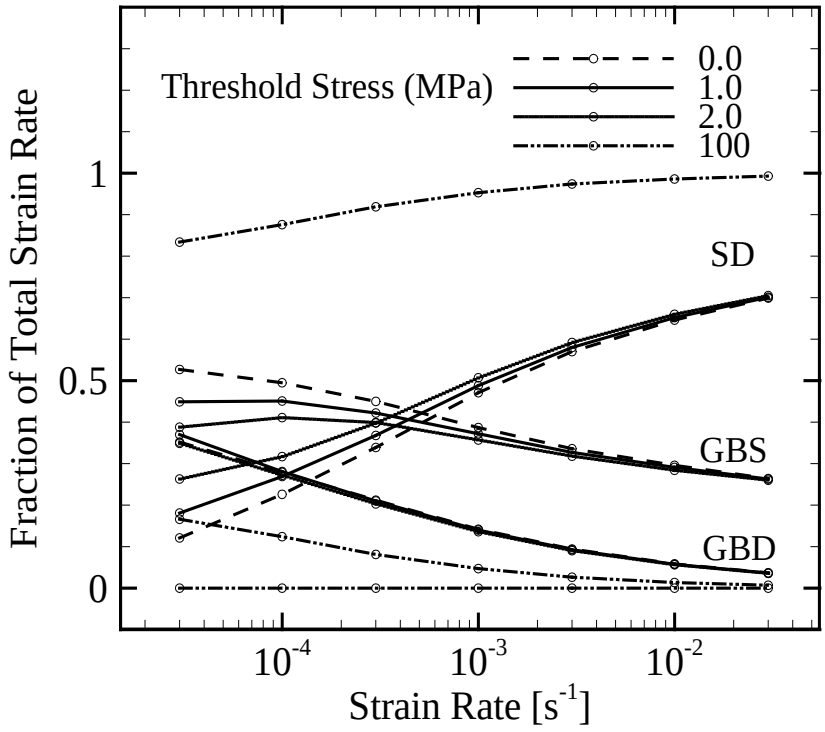

(c)

Figure 3-3 (a) Influence of threshold stress on stress versus strain rate curves. (b) Influence of threshold stress on stress exponent. (c) Influence of threshold stress on contribution from different deformation mechanisms.

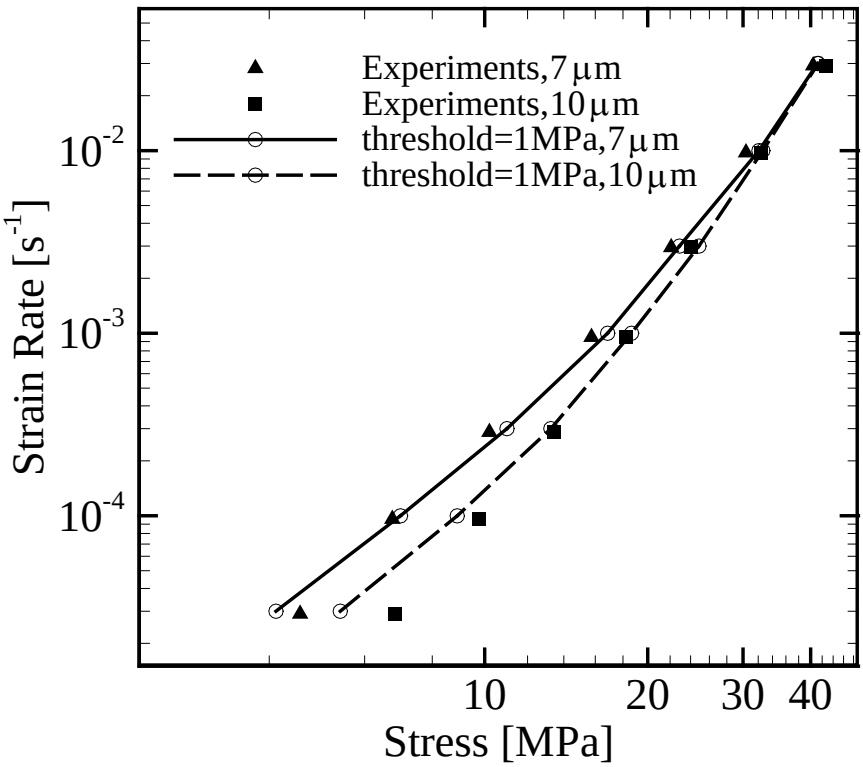

Figure 3-4 Comparisons of strain rate versus flow stress curves of simulations with experiments strain rate versus flow stress with threshold stress 1.0 MPa and other parameters in Table 1. Experimental data is from [73].

Chapter 4: Void Growth in Superplastic Aluminum Alloys at Elevated Temperature

Materials that are suitable for superplastic forming or quick plastic forming are prone to failure by the nucleation and growth of voids during forming. This is partly because the particulate grain refiners provide a high density of void nucleation sites, and is partly an undesirable consequence of the enhanced grain boundary sliding and diffusion that occurs in a fine-grained solid. Cavitation has been reported in deformation of a wide range of superplastic materials, including many Al alloys [58, 76-94], Mg based alloys [77, 81, 95-98] and Tin alloys [99]. Under certain conditions, extensive cavity growth and coalescence occur, forming inter-granular cracks and causing the material to fail prior to the occurrence of a plastic instability (such as necking) [58, 78]. Even when flow localization controls failure, final fracture generally occurs as a result of cavity growth and coalescence in the necked region.

Experimental studies show that the cavity growth rate can be influenced by many factors, including temperature [87, 90, 93, 97], grain size [58, 78], loading strain rate [58, 87, 90, 97], stress state [84], and strain [87, 95, 97]. In general, experiments suggest that fine grained materials are more prone to failure by cavitation and that void growth rates increase with temperatures and decrease with strain rate. Experiments also suggest that at least two different mechanisms may contribute to void growth. At low temperatures, or

high strain rates, dislocation creep is the dominant deformation mechanism. Under these conditions, cavities coalesce along the tensile axis and form string-like morphology [58, 78, 97]. In contrast, at high temperatures and low strain rates, when grain boundary sliding is the main flow mechanism, cavities coalesce in a more isotropic manner [58, 78, 97] and submicrometer fibers are observed on fracture surfaces and within surface cavities that form during deformation [58, 93, 94, 96]. It is believed that at high temperatures and low strain rates voids grow primarily by a diffusive process in which atoms detach from the surface of the cavity and diffuse into grain boundaries attached to the void or into the surrounding matrix, while at low temperatures, or high strain rates, void growth occurs as a result of dislocation creep in the surrounding grains.

A number of theoretical models have been developed with a view to predicting the void growth rate resulting from one or more of these processes (detailed summaries of the literature can be found in recent reviews by Kassner and Hayes [100] and Chokshi [101]. Existing models can be divided into three general types: (i) Models of void growth by plastic flow or creep (which neglect the effects of grain boundaries); (ii) Models of void growth by pure grain boundary diffusion (which idealize the grains as rigid) and (iii) Models which include both mechanisms. Void growth due to creep (see the review of [102] has been considered in both rate-independent plastic solids [103, 104] and in nonlinear viscous solids [105-107]. Models of diffusional void growth, in which grains are assumed rigid, were initiated by Hull and Rimmer [108], who considered the problem of a periodic array of voids along a planar grain boundary. More recently, Cocks and Searle [109] obtained a numerical solution to the void growth rate by grain boundary diffusion in an assembly of hexagonal grains containing a dilute distribution of voids,

with void size much less than the grain size. Models of void growth by coupled grain boundary diffusion and matrix plasticity were proposed by Speight and Beere [110], Edward and Ashby[111], Needleman and Rice[112], Cocks and Ashby[113a] [113b]. More recent studies have focused on the effects of stress triaxiality [114, 115], and the development of constitutive models for cavitating grain boundaries [116-118].

These theoretical studies have provided considerable insight into the mechanisms of void growth during plastic straining: in particular, models predict the general scaling of void growth rates with stress and grain size. All existing models are based on simplified idealizations of the materials microstructure (often using a periodic unit cell), however. From the standpoint of designing materials that are resistant to cavitation, a number of questions remain to be addressed. For example, do unit cell models predict accurately the behavior of a realistic microstructure? Are there particular features of a microstructure that give rise to particularly large void growth rates? In this paper, our objective is to extend existing models by including a more realistic description of the material's microstructure and behavior. To this end, we have adapted Bower and Wininger's [54] two-dimensional finite element model (described in Chapter 2) of deformation in a polycrystal during high-temperature straining, to predict the rate of growth of pre-existing cavities that lie on triple-grain junctions in the solid. The model includes the effects of dislocation creep within the grains, as well as diffusion and sliding on the grain boundaries. The computations account rigorously for the coupling between the various deformation mechanisms, and can therefore predict the dominant contributions to the plastic strain rate in the specimen, as well as the void growth rate, without a-priori assumptions. Although the computations are applicable, in principle, to any material

system, we have chosen to focus attention on 5083. This alloy was selected partly because of its technological importance, and partly because extensive experimental data are available for both its constitutive response [73] and also its cavitation behavior [58].

Our simulations are used to predict the influence of macroscopic loading conditions, and material features such as grain size, cavity size, the sliding resistance of grain boundaries, and the grain structure near the void, on the rate of growth of pre-existing voids in the solid. Void nucleation is neglected in our study partly for simplicity, but mainly because experiments suggest a low resistance to void nucleation in AA5083 due to the high density of second-phase particles in the solid, so that void growth is the limiting failure mechanism in practical applications. Our predictions are shown to be in good qualitative and quantitative agreement with experimental observations of cavitation in aluminum alloys.

1.10 Simulation Procedures

The material is idealized as a two-dimensional assembly of grains, which are separated by sharp grain boundaries, as illustrated in Figure 4-1. The polycrystal contains one pre-existing void, which is assumed to be located at a triple grain junction. The solid undergoes uniaxial tension with constant strain rate. Symmetry boundary conditions are imposed on the boundaries at $x = 0$ and $y = 0$; the boundary at $x = L$ or $y = H$ is displaced horizontally or vertically at the prescribed macroscopic strain rate $\dot{\varepsilon}_0$. Plane strain deformation is assumed.

In all simulations we take the void to be an equilateral triangle, as indicated in the Figure 4-1 (simulations show that the rate of void growth is relatively insensitive to changes in the shape of the void). Results will be reported for voids at several different locations in the microstructure.

At the triple grain junctions, the normal stress acting on the three grain boundaries that meet at the junction must be equal, to satisfy continuity of chemical potential. Similarly, the normal stress acting on grain boundaries that terminate at a void is related to the curvature of the void surfaces. For simplicity, we neglect the surface energy of the void, so that the normal stress must satisfy $\sigma_n = 0$ at the ends of such grain boundaries. In our computations, these constraints are enforced using a penalty method, as described in Bower and Wininger [54].

It is of particular interest to determine the contributions to the total void growth rate that arise from diffusion (due to atoms migrating from the void surfaces into grain boundaries), and a contribution that arises from the deformation of the surrounding grains. Grain boundary sliding does not directly contribute to void growth, but can influence the other two mechanisms. The void growth rate due to diffusion can be computed from the flux of atoms into all the grain boundaries connected to the void

$$\dot{V}^d = \sum_{k=1}^{N} j_k \,, \tag{4.1}$$

where N is the total number of junctions that connect the void surface and grain boundaries. The mass flux through each junction is computed from

$$j_k = \frac{\Omega \delta D_0 \exp(-Q_{GBD})}{kT} \frac{kT}{\partial s} \frac{\partial \sigma_n}{\partial s}. \tag{4.2}$$

The void growth rate due to deformation of the surrounding material is computed from

$$\dot{V}^c = -\int_{\Gamma_v} \dot{u}_i n_i^v d\Gamma_v \tag{4.3}$$

where Γ_v denotes the void surface, $\dot{u}_i$ is the velocity of the void surface, and n_i^v is the unit vector normal to the surface of the void. The total void growth rate is $\dot{V} = \dot{V}^c + \dot{V}^d$. It is important to note that $\dot{V}^c$ quantifies the void growth rate due to motion of the grains. Since the grains experience rigid motion even under conditions of pure diffusional creep, $\dot{V}^c$ cannot be interpreted as a strict measure of the contribution to void growth from dislocation motion.

Since a new constitutive equation of dislocation creep (power law creep) is used in this chapter, the finite element model needs to be recalibrated. We have used the same procedure described in Chapter 3 to determine values for material parameters in our model that represent the alloy AA5083. Most of the parameters in the model, including the atomic volume, elastic constants, and grain boundary diffusion activation energy are taken from standard references. The sliding fluidity of the grain boundaries was estimated using the Raj-Ashby model [13] of grain boundary sliding. This leaves four adjustable parameters: the grain boundary diffusion pre-exponential δD_0; the stress exponent Λ, the slip strength τ_0 and the characteristic slip rate $\dot{\gamma}_0$ in the slip law. These parameters were chosen to (i) match the variation of flow-stress with strain rate measured by Kulas, et al. [73] in polycrystalline AA5083 with a 7 micron grain size; and (ii) to predict a transition in deformation mechanism from grain boundary sliding creep to dislocation creep at a strain rate of $10^{-3}s^{-1}$, in order to match the texture observations of Agarwal, et al. [74]. The resulting parameter values are listed in Table 4-1.

1.11 Results and Discussion

We next proceed to study the influence of key material variables, such as grain size and the sliding resistance of grain boundaries, as well as key loading parameters such as the applied strain rate, on the rate of void growth with strain in a representative microstructure of AA5083. Our results will be presented as functions of representative variations in these parameters. Before proceeding with detailed simulations, however, it is worth noting that the dimensionless steady-state void growth rate $\dot{V}/V\dot{\varepsilon}_0$ is a function of six dimensionless parameters

$$\frac{\dot{V}}{V\dot{\varepsilon}_0} = f\left(\frac{\eta_0 L^2}{D\delta}, \frac{\dot{\gamma}_0 kTL^3}{\tau_0 \Omega D\delta}, \frac{\dot{\varepsilon}_0 kTL^3}{\tau_0 \Omega D\delta}, \frac{E}{\tau_0}, \frac{a}{L}, \Lambda\right) \tag{4.4}$$

where L is the grain size, $D = D_0 \exp(-Q_{GBD}/kT)$ is the grain boundary diffusion coefficient, E is the Young's modulus, a is the void size and other variables as defined previously. In this expression, the dimensionless void growth rate can be interpreted as the rate of change of void volume with strain. The first dimensionless group represents the rate of grain boundary sliding compared to the rate of grain boundary diffusion. The second parameter quantifies the rate of dislocation creep compared to the rate of grain boundary diffusion. We note also that $\left(\tau_0 \Omega D\delta / \dot{\gamma}_0 kT\right)^{1/3}$ is equivalent to the material length scale l proposed by Needleman and Rice [112], so that the second material parameter can also be regarded as quantifying the grain size compared with this material length scale. The third parameter can be regarded as a normalized strain rate, and represents the applied strain rate compared with the rate of grain boundary diffusion. The

fourth parameter quantifies the ratio of the elastic modulus to the flow stress of the grains; the fifth quantifies the void size compared to the grain size; and the last one is the dislocation creep exponent.

Several qualitative predictions can be made on the basis of these dimensionless groups. For example, the first dimensionless group suggests that reducing the grain size is equivalent to increasing the grain boundary diffusion coefficient compared to the grain boundary fluidity. Similarly, the second dimensionless group suggests that reducing the grain size is equivalent to increasing the rate of grain boundary diffusion compared with dislocation creep. We therefore anticipate a transition from grain dislocation creep dominated behavior to diffusion or grain boundary sliding dominated behavior at some critical grain size, to be determined. Similarly, increasing the applied strain rate is comparable to reducing the flow stress of the grains or the grain boundary diffusion coefficient, and is therefore expected to cause enhanced dislocation creep. These qualitative trends are explored in more detail in the sections to follow.

Our simulations show that the rate of void growth is strongly sensitive to the detailed shape and orientation of the grains near the void. One consequence of this sensitivity is that the rate of void growth is *anisotropic* – that is to say, the void growth rate depends on the orientation of the tensile axis relative to the local microstructure near the void. In fact, in some cases the void growth rate can even differ in sign depending on whether the solid is loaded horizontally or vertically. This behavior will be discussed in more detail in Section 4.2.6. The anisotropy in void growth rate is extremely sensitive to microstructure, but the average void growth rate for solids loaded both horizontally and vertically shows less variation from one location in the solid to another. Consequently, in

the parameter studies to follow we shall report average void growth rates unless explicitly stated otherwise.

1.11.1 Effects of Applied Strain Rate and Grain Size

The formability of AA5083 at elevated temperatures is typically optimized by reducing the material's grain size as far as possible, to ensure that the material has a high strain rate sensitivity and low flow stress, and by selecting an appropriate strain rate for the forming process. The influence of strain rate and grain size on cavitation are therefore of particular interest.

Figure 4-2 shows the void growth rate as a function of the applied strain rate for four different grain sizes. The ratio of void volume V to grain volume V_g was held fixed with $V / V_g = 0.004$ when changing the grain size (in the next section, we show that void growth rate is sensitive to void size, and decreases with V). Note that the void growth rates are reported in normalized form: the ratio $\dot{V} / V\dot{\varepsilon}_0$ can be interpreted as the rate of increase of void volume with strain.

For any grain size, the rate of void growth with strain at low strain rates is typically an order of magnitude faster than at high strain rates. The asymptotic behavior as strain rate is reduced to zero, as well as that for high strain rate, is relatively insensitive to grain size. The transition from fast to slow void growth rates takes place over a relatively narrow range of strain rate, which depends strongly on grain size. For a typical AA5083 alloy with 7μm grain size used for warm forming, the transition occurs at a strain rate of order $10^{-3}s^{-1}$.

The change in void growth rate with strain rate occurs mainly due to a change in the deformation mechanism in the polycrystal. This is illustrated in Figure 4-3, which plots (a) the fraction of strain rates due to dislocation creep, grain boundary diffusion and grain boundary sliding in a material of 7μm grain size (b) the fraction of the growth rate due to diffusion $\dot{V}^d / \dot{V}$ (defined in equation (4.1)) as a function of strain rate, for four values of grain size. Figure 4-3 (a) shows that as strain rate increases the dominant deformation mechanism changes from grain boundary diffusion accommodated by grain boundary sliding to a combination of dislocation creep and grain boundary sliding. Figure 4-3 (b) shows that at low strain rates void growth occurs primarily by grain boundary diffusion, while it occurs by plastic flow of the surrounding grains at high strain rate. The contribution from grain boundary diffusion decreases with increasing strain rate and grain size. Note that in the material with 7μm grain size the void growth rate drops by a factor of 3 in changing strain rate from 10^{-5} to 10^{-3}, but there is no appreciable reduction in the fraction of void growth rate due to diffusion. This indicates that the change of void growth rate with strain rate is mainly associated with the change in deformation mechanism, which occurs at the same strain rate (Figure 4-3 (a)).

Two separate effects are responsible for the sensitivity of void growth rate to grain size. First, in fine grained materials diffusive void growth occurs more readily because material diffuses over shorter distances. This is the process considered by Needleman and Rice [112] in their study of void growth by coupled diffusion and creep: their calculations show that this mechanism tends to increase the void growth rate as the grain size and void size are reduced. In our simulations a second mechanism, which is not present in their model, also operates. The polycrystalline matrix surrounding the void can

be regarded as a power-law creeping material with an effective stress exponent *n* that is sensitive to strain rate (and grain size) [69, 73]. Approximate analytical models of void growth in a power-law creeping matrix [107] predict that void growth rate due to creep increases by approximately a factor of 2 as the stress exponent varies between 1 and 4. Since the effective stress exponent for the polycrystal increases with strain rate, this trend tends to reduce the sensitivity of void growth rate to strain rate.

1.11.2 Effects of Void Size

The normalized rate of growth of a void changes as its size increases. This behavior is illustrated in Figure 4-4 which shows the normalized void growth rate as a function of the void volume (normalized by grain volume), for a specimen subjected to three different strain rates. Results are shown for a material with a 7 micron grain size, with the void at a fixed location in the microstructure.

At strain rates below $10^{-4}s^{-1}$ (when diffusion is the dominant mechanism of void growth) the normalized void growth rate varies inversely with void volume. This is because the volumetric flux leaving the void is determined primarily by the grain structure near the void, and is not influenced greatly by void size and shape. Since the volumetric flux is constant, the normalized void growth rate varies inversely with void volume. This trend matches the predictions of Cocks and Searle [109], who analyzed void growth in a periodic array of rigid hexagonal grains. Their prediction is shown as a dashed line in Figure 4-4: it differs from our results due to the influence of microstructure, which will be discussed in more detail in Section 4.2.6.

The sensitivity of void growth rate to void size decreases as the strain rate is increased. At strain rates exceeding 10^{-2} s^{-1}, void growth occurs primarily by plastic deformation of the grains surrounding the void, and under these conditions the solid can be regarded as a power-law creeping solid. The normalized void growth rate in a power-law creeping material is independent of void size [107]. In our simulations, there is a small sensitivity to void size even when plastic flow is the only mechanism of void growth, since the growth rate of voids that are much smaller than the grain size is determined by the orientation of the grains immediately adjacent to the void, while the rate of growth of voids comparable to, or larger than, the grain size is determined by the collective behavior of the matrix.

1.11.3 Effect of Stress Triaxiality

The effect of stress triaxiality is examined by superimposing a uniform traction in the direction perpendicular to the straining direction. For example, uniform stress is superimposed on the $y = H$ in *y*-direction when the material is loaded with uniform strain rate in *x*-direction. Similarly, when the material is strained in *y*-direction, a uniform stress is superimposed on $x = L$ in *x*- direction. The void growth rate reported in this section is the average in *x*- and *y*-directions. The influence of the anisotropy of void growth rate on stress triaxiality effect will be discussed in Section 4.2.6.

Figure 4-5 shows the void growth rate as a function of triaxiality with three strain rates. The void growth rate is significantly elevated by increased mean stress at all strain rates, however the void growth rate increases more rapid with stress triaxiality at low strain rate than high strain rate in the stress triaxiality range considered here.

The simulations predict a linear dependence of the void growth rate on triaxiality for strain rate of $10^{-6}s^{-1}$ and $10^{-3}s^{-1}$. The prediction for $10^{-6}s^{-1}$ is compared to the solution for hexagonal grains undergoing Coble creep [109]. Our simulations predict much higher anisotropy at zero triaxiality than reported in Cocks. The average growth rate is also higher than predicted by the Coble creep solution under the same positive triaxiality. These differences between our simulation and Cocks solution should be mainly due to the microstructure difference. The effect of microstructure on void growth is discussed in Section 4.2.5.

The simulations predict a power-law dependence on triaxiality at stain rate of $1.0s^{-1}$. The void growth rate is much more sensitive than predicted by a solution of a void in a powerlaw creep solid [107] due to several reasons. First, our simulations are based on plane strain assumption while the Budiansky solution is based on cylinderal symmetry assumption. Second, grain boundary diffusion still contributes a small portion to the total void growth. In this case, the fraction of diffusion growth is about 20-30%.

Figure 4-6 shows void growth rate as a function of stress triaxiality for various grain sizes with strain rate of $10^{-3}s^{-1}$. The simulations predict more rapid increase in void growth rate with triaxiality in fine grained material than coarse grained material. In fine grained material the dependence of void growth rate on triaxiality is linear. As grain size increase the dependence transfers to power law dependence. This is transition is possibly because the void growth is dominated by grain boundary diffusion in fine grained material and by plastic flow of the surrounding grains in coarse grained materials.

1.11.4Effect of Grain Boundary Sliding Resistance

The influence of material parameters on cavitation has been extensively studied in earlier work [103, 107, 112, 119] (see the review of Kassner and Hayers [100]). The influence of resistance to grain boundary sliding, however, has not so far been addressed. Increasing the rate of grain boundary sliding, with a view to producing enhanced strain rate sensitivity, is one approach to improving high-temperature formability of aluminum alloys. It is of particular interest, therefore, to determine the influence of grain boundary sliding on cavitation.

In our model, the resistance to grain boundary sliding is characterized by the fluidity $\eta_0 = \Omega v_0 \exp(-Q_{GBS} / kT) / kT$, equation (2.11), which specifies the relative sliding velocity of two adjacent grains at unit stress. The value of η_0 is difficult to determine accurately: in our computations, its value was estimated using the model developed by Raj and Ashby [13].

Because sliding is volume preserving, it does not directly contribute to cavity growth, although it may tend to promote void nucleation by inducing strain or stress concentrations at the triple grain junctions. Void nucleation is beyond the scope of this study, but we have investigated the influence of grain boundary sliding on void growth rate.

Figure 4-7 shows the normalized void growth rate as a function of grain boundary sliding fluidity for three strain rates (note that high values of fluidity correspond to freely sliding grain boundaries, while boundaries with low fluidity resist sliding). The void growth rate is strongly sensitive to grain boundary fluidity especially at low strain rates: voids grow four times more quickly in a material with sliding resistant grain boundaries than in a solid with freely sliding boundaries with strain rate $10^{-6}s^{-1}$. This is a

counterintuitive result: one might expect that freely sliding grains tend to promote cavity growth, but this is not the case. There are two possible explanations for this behavior. Firstly, in a material with freely sliding grain boundaries, the grains remain essentially rigid if the material is deformed at low strain rates. Under these conditions the stresses remain relatively low, and material flowing out of a void is accommodated by the relative displacement of the grains surrounding the void. When grain boundary sliding is suppressed, the diffusional flow must be accommodated instead by plastic deformation (by dislocation creep) in the interior of the grains. This tends to raise the stresses acting on grain boundaries and so increases the rate of diffusional flow. Secondly, grain boundary sliding increases the effective stress exponent for the creep behavior of the polycrystal. For example, at a strain rate of $10^{-6}s^{-1}$, the stress exponent changes from 1.00 to 3.74 when the freely sliding grain boundaries are replaced by very viscous grain boundaries. Analytical models of void growth in power-law creeping solids [107] predict that the void growth rate increases as the stress exponent increases.

The implication is that grain boundary sliding can be increased to promote formability without risking a detrimental effect on cavitation. Some care is required, however, to ensure that any microstructural changes that are exploited to promote grain boundary sliding (such as increasing the fraction of high angle grain boundaries in the microstructure) do not influence the rate of grain boundary diffusion. Increases in grain boundary diffusivity can greatly enhance cavitation. For example, the faster void growth rates observed in fine grained solids and at low strain rates are caused entirely by an increase in the rate of diffusion, not by enhanced grain boundary sliding.

1.11.5 The Influence of Microstructure

Several results described in the preceding sections suggest that the void growth rates predicted by our computations differ significantly from the results of earlier computations that were based on periodic microstructures. We proceed to explore these discrepancies further.

Our simulations show that cavity growth rates are strongly sensitive to the local grain structure near the void. A striking demonstration of this sensitivity is that void growth rates are sensitive to the orientation of the tensile axis with respect to the underlying microstructure, even though the macroscopic constitutive response of the solid is isotropic.

The anisotropy of void growth is illustrated in Figure 4-9, which variation of void growth rate with strain rate for loading conditions with tensile axis parallel to the *x* and *y* directions. Results are shown for two voids at different locations indicating in

Figure 4-8. For some locations, loading in one direction can cause the void to increase in size, while loading in the opposite direction causes the void to shrink.

The anisotropy in void growth rate observed in our simulations is significantly greater than predicted by previous models. Models of void growth by plastic flow in power-law creeping solids naturally predict no anisotropy. Anisotropy has been detected in the diffusional growth regime: for example, Cocks and Searle [109] observed a small anisotropy in simulations of diffusive void growth in an assembly of rigid hexagonal grains, but showed that the anisotropy is primarily caused by specimen size effects. Specimen size effects were checked as a possible cause of anisotropy in our simulations, but specimen size was found to have no discernable influence.

The anisotropy predicted by our simulations appears to be associated with the detailed grain structure surrounding the void. To show this, void growth rates were computed at several different locations in the grain structure, and for each location, the following measure of anisotropy was evaluated

$$A = 2(\dot{V}_x - \dot{V}_y) / (\dot{V}_x + \dot{V}_y) \tag{4.5}$$

where $\dot{V}_x$ and $\dot{V}_y$ are the void growth rates for straining parallel to the *x* and *y* directions. The void locations are illustrated in

Figure 4-8, and the anisotropy *A*, together with the average void growth rate $(\dot{V}_x + \dot{V}_y) / 2\dot{V}\dot{\varepsilon}_0$ are summarized in

Table 4-2.

There is clearly a substantial variation in anisotropy from one location in the microstructure to another. The average void growth rate shows less variation, although the average void growth rates in different locations of the microstructure can differ by over a factor of two, indicating a strong influence of local grain structure.

At low strain rates, the average void growth rate shows a clear correlation with the size of the grains adjacent to the void. Locations with the highest growth rate (c, f and g) are in regions with small grains; while voids with the slowest growth rate (a, b and d) are located near at least one, and most cases several, large grains.

It is more difficult to correlate the anisotropy in void growth rate with specific microstructural features. The possible sources of anisotropy include:

1. The crystallographic orientation of the grains near the void
2. The shape and size of the void;
3. The orientation of the grain boundaries connected to the void;
4. The size and geometry of the grains adjacent to the void;

We have conducted a large number of simulations in an attempt to identify the role of each variable. It was difficult to see clear trends in the data: each feature of the microstructure appears to influence the anisotropy, but no single mechanism plays a dominant role. At high strain rates, where deformation and void growth occur primarily as a result of dislocation creep (plasticity) in the grains, the anisotropy is relatively insensitive to the geometry of the grain boundaries; but is strongly sensitive to the orientation of the grains near the void, and is also influenced more weakly by the shape and size of the void. It is clear that in this regime the anisotropy is associated primarily with the anisotropy of slip in the grains near the void. At low strain rates, the anisotropy is insensitive to the crystallographic orientation of the grains and is also weakly sensitive to the shape and size of the void. However, in this regime the anisotropy is strongly sensitive to the geometry of the grain boundaries connected to the void, and the size and geometry of the grains adjacent to the void. At low strain rates the anisotropy appears to be associated with uneven volumetric flow of material through the grain boundary network, possibly augmented by grain boundary sliding.

The processes that give rise to anisotropy at high strain rates (where plasticity dominates void growth), and those that produce anisotropy at low rates (where diffusion dominates) need not give rise to anisotropy with the same sign. In one case, void growth may be more rapid when the solid is loaded in the horizontal direction; in the other, growth may be rapid for vertical loading. This accounts for the transition in anisotropy with strain rate observed in Figure 4-9, for example.

Although it is difficult to identify specific microstructural features that control the orientation dependence of void growth rate, the anisotropy is clearly determined by the

details of the grain geometry in the neighborhood of the void, and is insensitive to microstructure far from the void. To show this, we have computed the changes in void growth rate that resulting from small changes in the grain geometry. In each simulation the location of a single triple junction in the grain structure was changed, as indicated in Figure 4-8. The void growth rate before and after each change in the microstructure is given in Table 4-3. It appears that the void growth rate is sensitive only to perturbations that are less than 3 grain diameters away from the void.

1.11.6 Comparison to Experiment

A qualitative experimental confirmation of the effects of grain size and strain rate on cavitation in AA5083 is shown in Figure 4-10. The micrographs show failure morphology in AA5083-H18 with several different grain sizes, tested at a range of strain rates. The material tested had a nominal composition of (Al - 4.6w/o Mg – 0.8w/o Mn – 0.1w/o Cr). The samples with different grain sizes were prepared by critical strain annealing. Specifically, samples were first recrystallized for 15 min. at 500ºC to produce a substantially strain-free condition with an average grain size of approximately 7.0 μm. Following cold rolling reductions of 0 to 80%, the material was recrystallized at 450ºC to produce a larger grain size than the initial starting structure. Materials were evaluated in three different conditions representing average grain sizes of 7.0, 22.3, 81.7 μm.[1] All specimens were strained to failure at 450 ^{0}C and constant nominal strain rate.

[1] Grain size was measured using ImagePro™software following ASTM standard E112 with concentric circles. Grain size is represented as an average linear intercept length.

For the fine-grained (7.0 μm) material, significant cavitation is observed at $0.0003s^{-1}$ and $0.001s^{-1}$. These samples show uniform deformation up to fracture, with no evidence of macroscopic necking. In contrast, at strain rates exceeding $0.01s^{-1}$, significant necking is observed, and cavities can only be found near the fracture surface. In specimens with 7 μm grain size, theory predicts a reduction in cavity growth rate by a factor of 2.2 to 1.2 with V/V_g between 0.004 and 0.229 as strain rate is increased from 0.001 s^{-1} to 0.01 s^{-1}, in qualitative agreement with experiment. Similarly, experiments show a clear reduction in the density and size of voids in materials with larger grain sizes.

Quantitative measurements of cavity volume fraction as a function of strain in AA5083 have been reported by Kulas, et al. [58]. They show that, for strains in the range $0.8 < \varepsilon < 2.2$ the relationship between void volume fraction and strain can be fit by an expression of the form

$$V_f = V_0 \exp(\eta' \varepsilon) \tag{4.6}$$

where η' and V_0 are constants. This implies that the normalized rate of change of void volume fraction satisfies $\dot{V}_f / V_f \dot{\varepsilon} = \eta'$ (equal to our measurement of normalized void growth rate). They report that the normalized growth rate is 5.4 at $3 \times 10^{-4} s^{-1}$, and decreases to 1.7 at a strain rate of $3 \times 10^{-2} s^{-1}$ and above. Our results predict that the cavity growth rate depends on void size. If we assume that the average void size is constant with $V/V_g = 0.229$ in the experiments due to nucleation of new voids, our simulations predict normalized void growth rate of 8.77 at strain rate $3 \times 10^{-4} s^{-1}$ and 5.46 at strain rate $3 \times 10^{-2} s^{-1}$, in good agreement with the experimental data.

Direct measurements of cavity size as a function of strain have also been reported by Bae and Ghosh [87]. Their data are compared with the predictions of our simulations in Figure 4-11. The simulations clearly capture all the main features of experimental observations, including a rapid rate of growth for small voids; an increase in growth rate with strain rate; and an earlier transition from fast to slow growth at high strain rates. The quantitative rate of growth predicted by our model is also in good agreement with the experimental data.

1.12 Conclusions

Finite element simulations have been used to conduct a systematic study of the mechanisms of void growth in polycrystalline Al AA5083 during elevated temperature straining. The model includes the effects of grain interior dislocation creep, grain boundary diffusion and grain boundary sliding, and modeled a realistic two dimension microstructure consisting of 236 grains. The simulations were used to predict the effects of loading conditions, material parameters and microstructure on the rates and mechanisms of void growth. The principal conclusions of our simulations are:

1. A threefold increase in the rate of void growth (normalized by void volume) with strain occurs in a typical AA5083 material with 7μm grain size as the strain rate is reduced from $10^{-2}s^{-1}$ to 10^{-3} s^{-1}. Outside this range, void growth rates are relatively insensitive to strain rate.
2. The increase in void growth rate at low strain rates is caused primarily by a transition from void growth by plastic flow (at high rates) to a combination of plastic flow and

grain boundary diffusion (at intermediate rates) to pure grain boundary diffusion (at low strain rates). The transition occurs at higher strain rates in coarse-grained materials: for example, increasing grain size to 15 μm reduces the critical strain rate at the transition by two orders of magnitude;

3. The growth rate of cavities with strain decreases as their size increases. The sensitivity to void size is greatest for low strain rates where diffusion is the dominant growth mechanism, and
4. Increasing the rate of grain boundary sliding (by increasing the fluidity of the grain boundaries) retards void growth, especially at low strain rates. This is because grain boundary sliding tends to relax the stresses on grain boundaries. This is a counterintuitive result, and suggests that grain boundary sliding can be increased to improve formability without significantly increasing void growth rates. Increased grain boundary sliding may promote void nucleation, however, which has not been addressed in our study.
5. Our simulations show that void growth rates are strongly sensitive to the detailed grain structure near the void. One consequence of this sensitivity is that void growth behavior is strongly sensitive to the orientation of the tensile axis. Several causes have been identified that contribute to the anisotropy. At high strain rates (where dislocation creep dominates), the anisotropy is due primarily to the anisotropic nature of dislocation creep in the grains adjacent to the void, and thus is determined by the orientations of the grains near the void. At low strain rates, the anisotropy is a consequence of uneven diffusional flow through the grain boundary network surrounding the void. We have not so far been able show a clear correlation of the

anisotropy with specific microstructural features.

6. The void growth rates predicted by our simulations are in good qualitative agreement with experimental measurements of cavity volume fraction and cavity size during elevated temperature straining of Al alloys.

Table 4-1 List of parameters used in simulations.

Parameter	Value
Grain size L	7 μm
Temperature T	723 K
Atomic volume Ω	1.66×10^{-29} m^3
Young's modulus E	70 GPa
Poisson's ratio ν	0.3
Characteristic strain rate $\dot{\gamma}_0$	5.2 s^{-1}
Slip system strength τ_0	65 MPa
Stress exponent of slip Λ	4.5
Grain boundary diffusion activation energy Q_{GBD}	1.34×10^{-19} J
Grain boundary diffusion pre-exponential δD_0	9.9×10^{-14} m^3 s^{-1}
Grain boundary sliding fluidity η_0	4.74×10^{-14} $m^4 J^{-1} s^{-1}$

Table 4-2 Growth rate of a void of fixed size and shape at different locations in the microstructure with $V/V_g = 0.002$ and grain size 7 micron.

	$\dot{\varepsilon}_0 = 10^{-6}$ s^{-1}				$\dot{\varepsilon}_0 = 1.0$ s^{-1}			
Triple junction	$\frac{\dot{V}_x}{V\dot{\varepsilon}_0}$	$\frac{\dot{V}_y}{V\dot{\varepsilon}_0}$	A	$\frac{\dot{V}_x+\dot{V}_y}{2V\dot{\varepsilon}_0}$	$\frac{\dot{V}_x}{V\dot{\varepsilon}_0}$	$\frac{\dot{V}_y}{V\dot{\varepsilon}_0}$	A	$\frac{\dot{V}_x+\dot{V}_y}{2V\dot{\varepsilon}_0}$
a	573.83	-110.24	2.95	231.79	14.73	17.46	-0.17	16.09
b	476.19	-25.04	2.22	225.57	18.95	4.38	1.25	11.66
c	452.71	153.25	0.99	302.98	2.23	32.87	-1.75	17.55
d	315.48	21.79	1.74	168.63	9.59	16.22	-0.51	12.90
e	307.96	340.18	-0.10	324.07	22.60	5.63	1.20	14.11
f	100.04	463.34	-1.29	281.69	24.40	5.75	1.24	15.07
g	44.42	512.86	-1.68	278.64	30.17	8.56	1.12	19.36
h	201.54	268.74	-0.29	235.14	20.29	0.83	1.84	10.56
Average			0.57	256.07			0.53	14.66
Standard Deviation			1.68	50.13			1.21	2.97

Table 4-3 Void growth rate before and after perturbations in the microstructure at various distances relative to the void. The void is held fixed at location g with strain rate 10^{-6}s^{-1}, $V/V_g = 0.002$, and grain size 7 micron.

Perturbation location	$\frac{\dot{V}_x}{V\dot{\varepsilon}_0}$	$\frac{\dot{V}_y}{V\dot{\varepsilon}_0}$	A	$\frac{\dot{V}_x+\dot{V}_y}{2V\dot{\varepsilon}_0}$	Change in A	Change in $\frac{\dot{V}_x+\dot{V}_y}{2V\dot{\varepsilon}_0}$
Before perturbation	44.42	512.86	-1.68	278.64	N/A	N/A
A, 1	15.18	565.88	-1.90	290.53	-12.75%	4.27%
A, 2	14.51	540.71	-1.90	277.61	-12.75%	-0.37%
B	101.94	459.03	-1.27	280.49	24.27%	0.66%
C	73.86	488.78	73.86	488.78	12.27%	0.96%
D	39.92	518.45	-1.71	279.19	-1.96%	0.20%
E	42.59	515.06	-1.69	278.82	-0.80%	0.07%

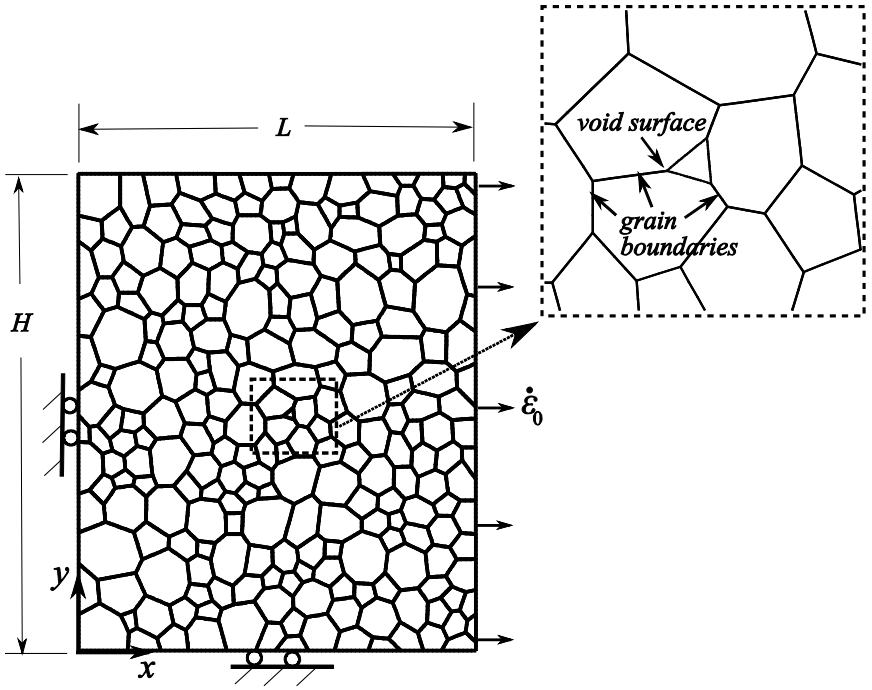

Figure 4-1 A representative microstructure consists of 236 grains used in the finite element simulations.

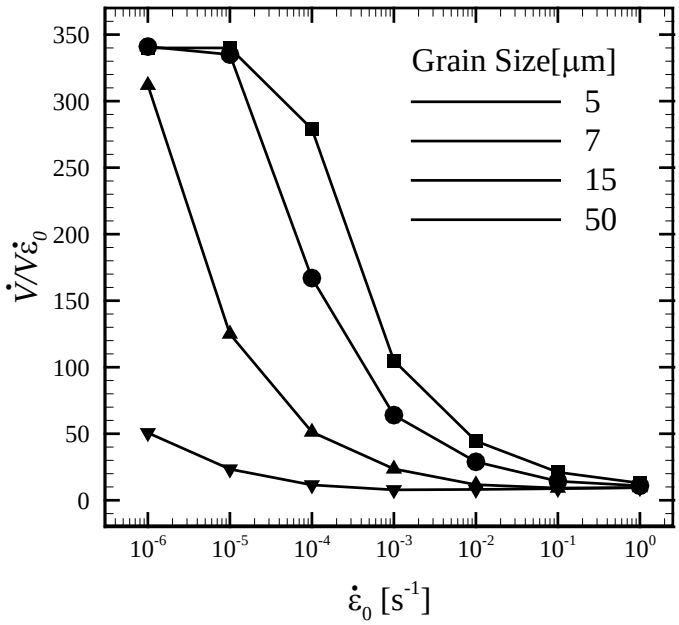

Figure 4-2 The effects of grain size and strain rate effect on the rate of change of void size with strain. The ratio of void volume V to grain volume V_g is 0.004.

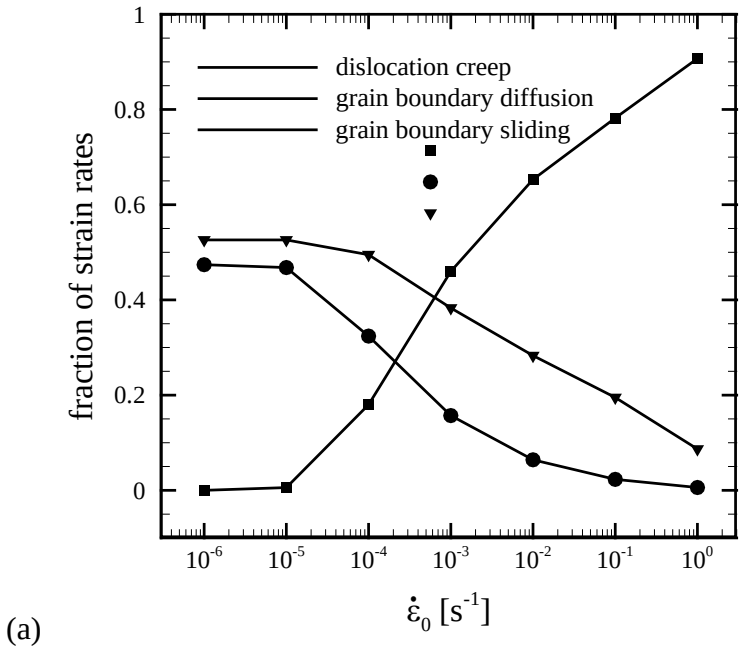

(a)

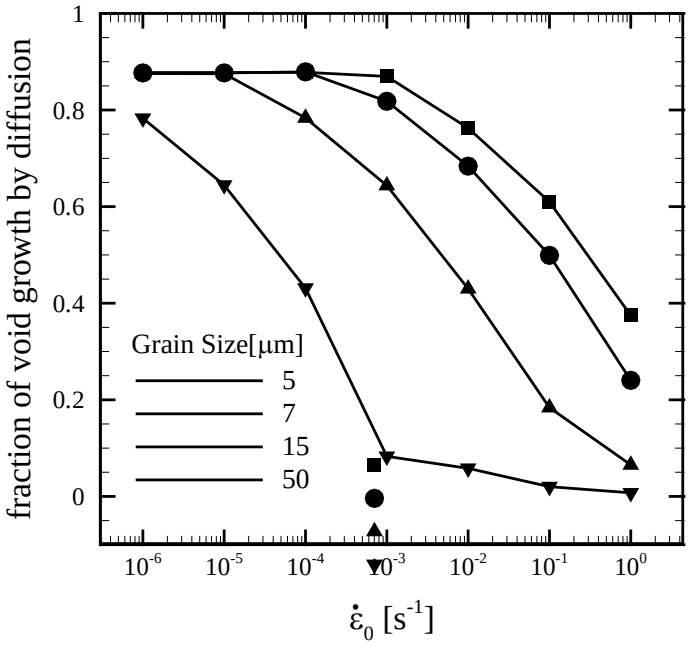

(b)

Figure 4-3 Mechanism of (a) deformation and (b) void growth. (a) shows the fraction of strain rates due to dislocation creep, grain boundary diffusion and grain boundary sliding in the material of 7 micron grain size. (b) shows the grain size and strain rate effect on predicted fraction of diffusional void growth rate. $V / V_g = 0.004$.

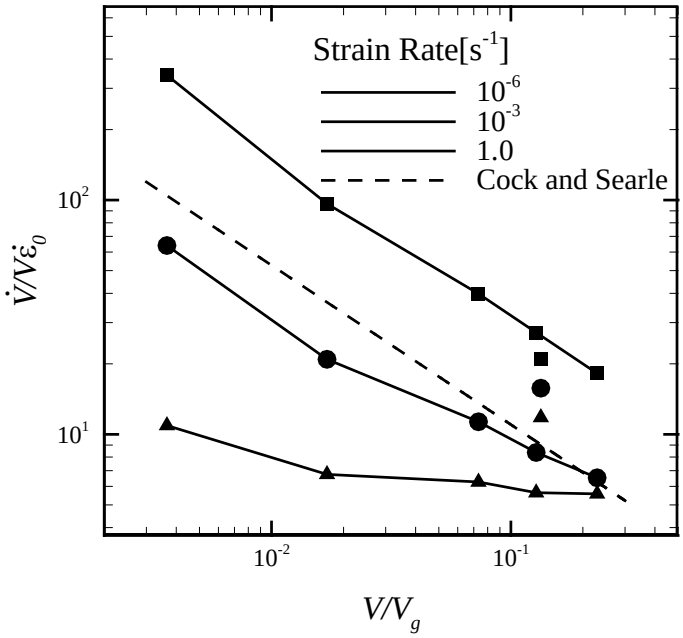

Figure 4-4 Void size and strain rate effect on void growth rate (The data is computed with a material with 7 μm grain size).

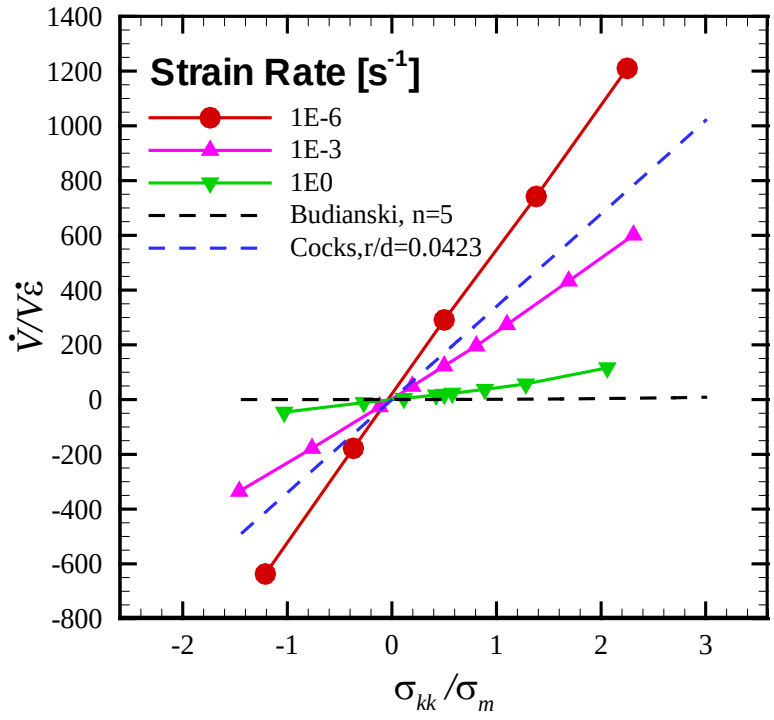

Figure 4-5 triaxiality effect on void growth rate under various loading strain rates.

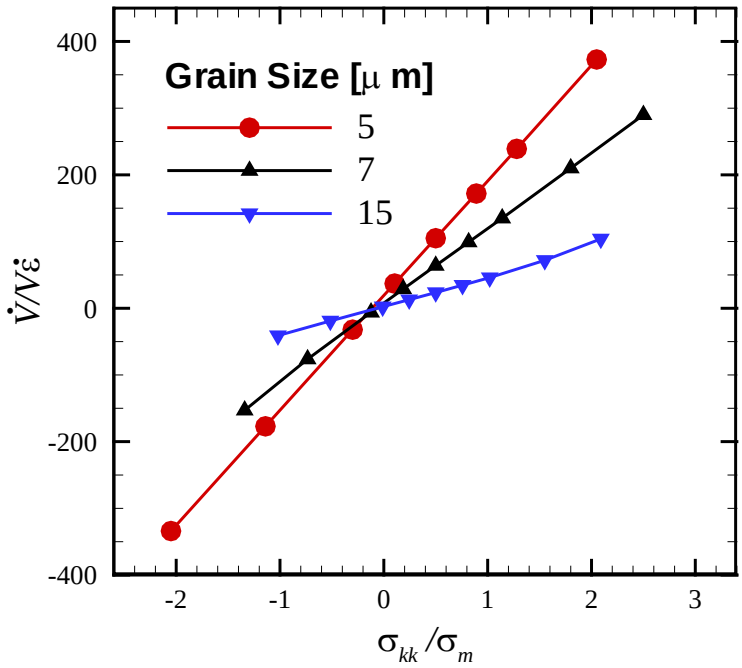

Figure 4-6 Normalized void growth rate as a function of normalized remote mean stress with various grain size.

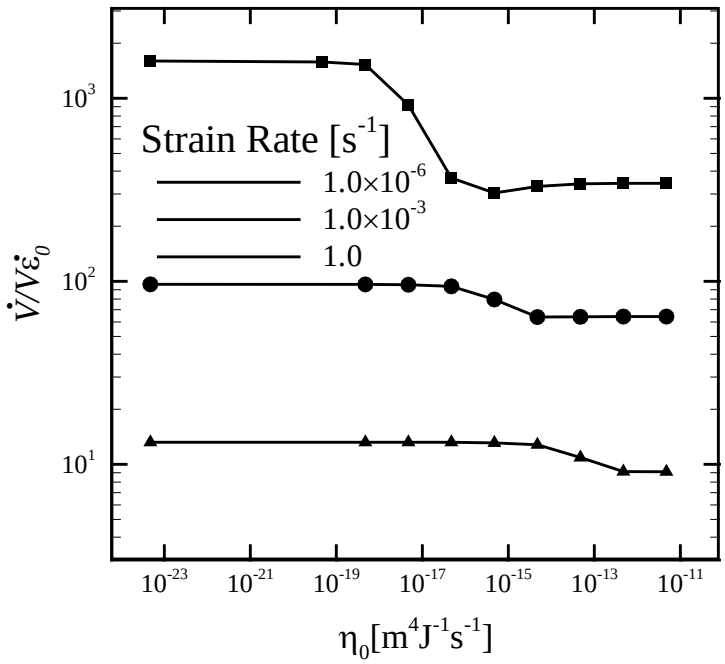

Figure 4-7 The influence of grain boundary fluidity on normalized void growth (with 7 micron grain size and $V/V_g = 0.004$).

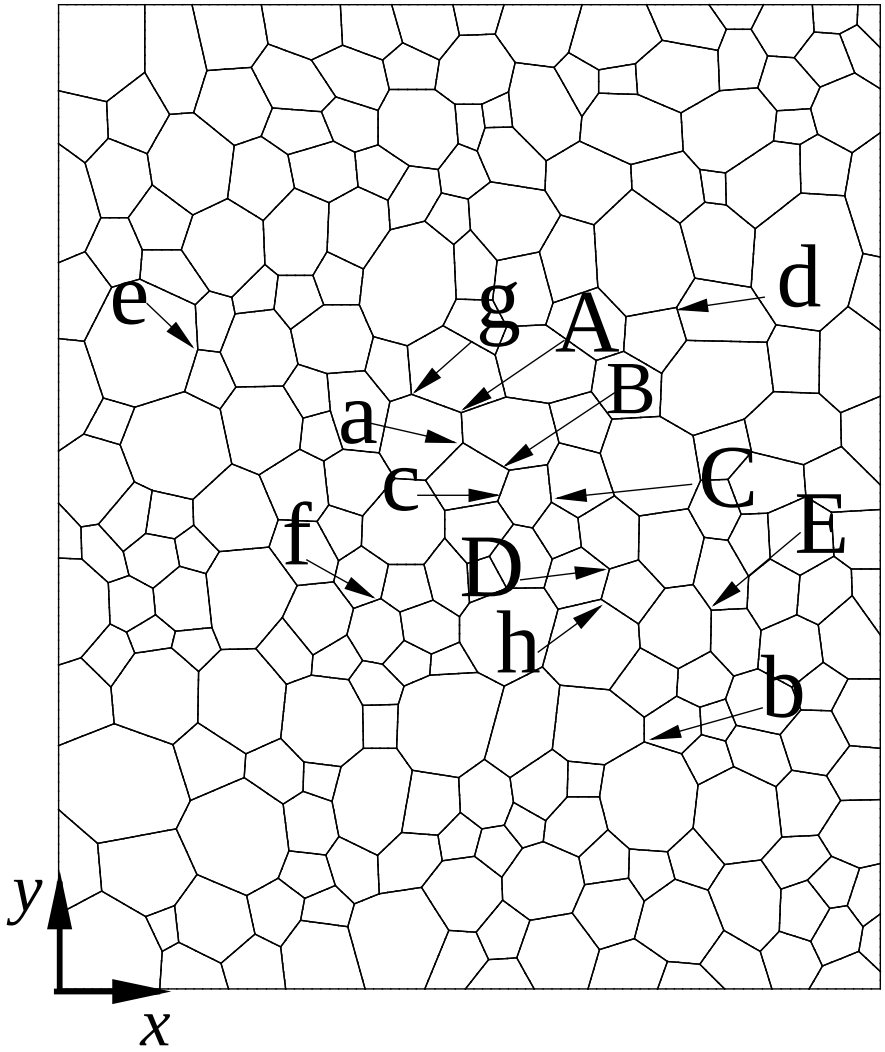

Figure 4-8 Locations of cavities (shown in lower case letters) and perturbations (shown in capital letters) in simulations used to probe the microstructure effect on void growth.

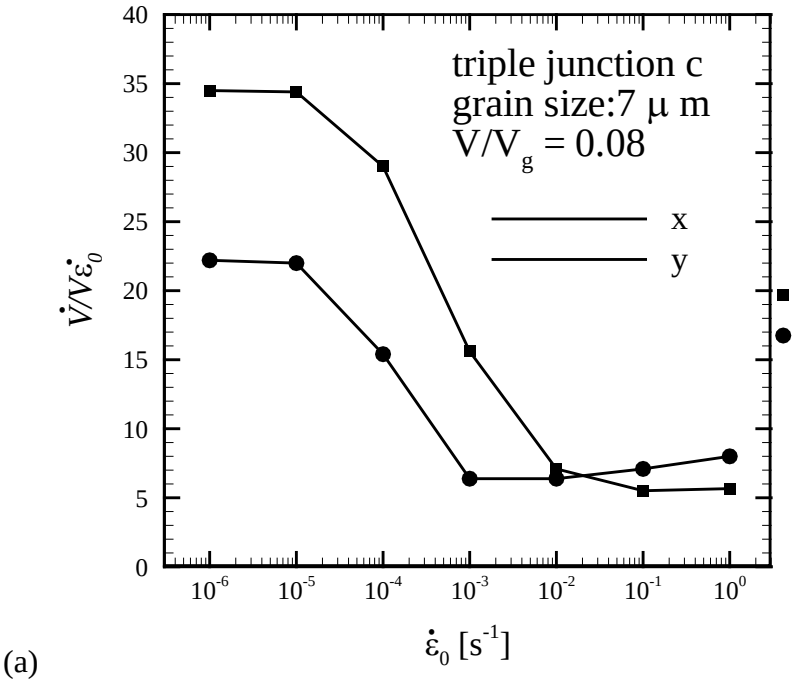

(a)

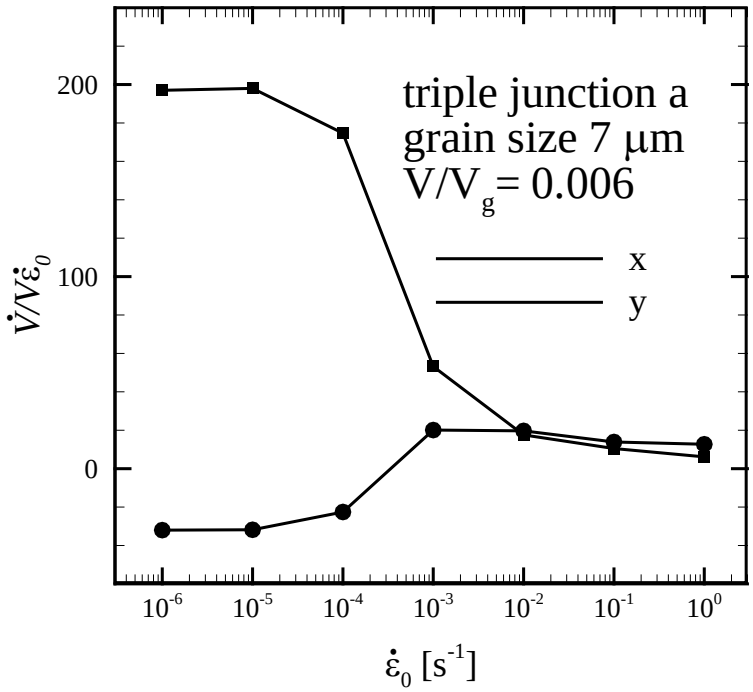

(b)

Figure 4-9 Void growth rate as a function of strain rate at two locations indicated in Figure 4-8. Results are shown for uniaxial straining in the horizontal (x) and vertical (y) direction.

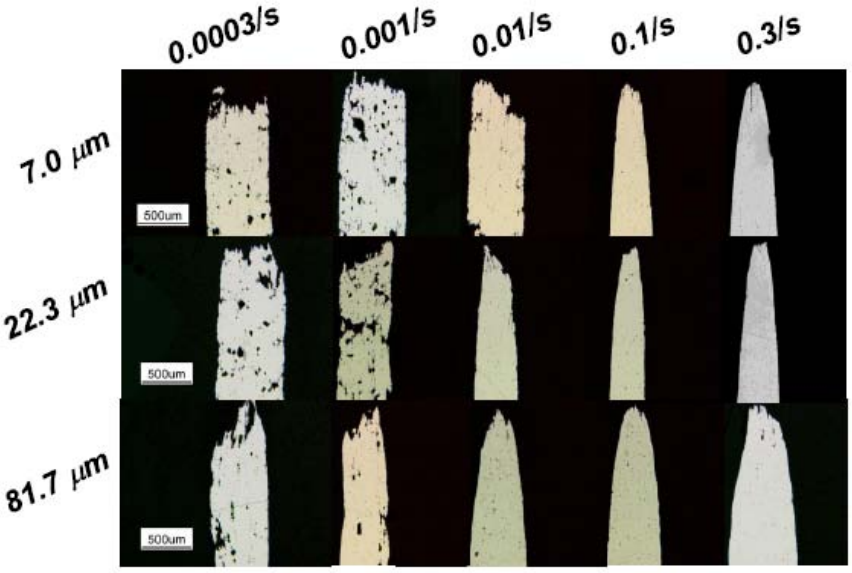

Figure 4-10 Experimental observations of the effect of grain size and strain rate on failure morphology and cavitation behavior of AA5083 at 450ºC.

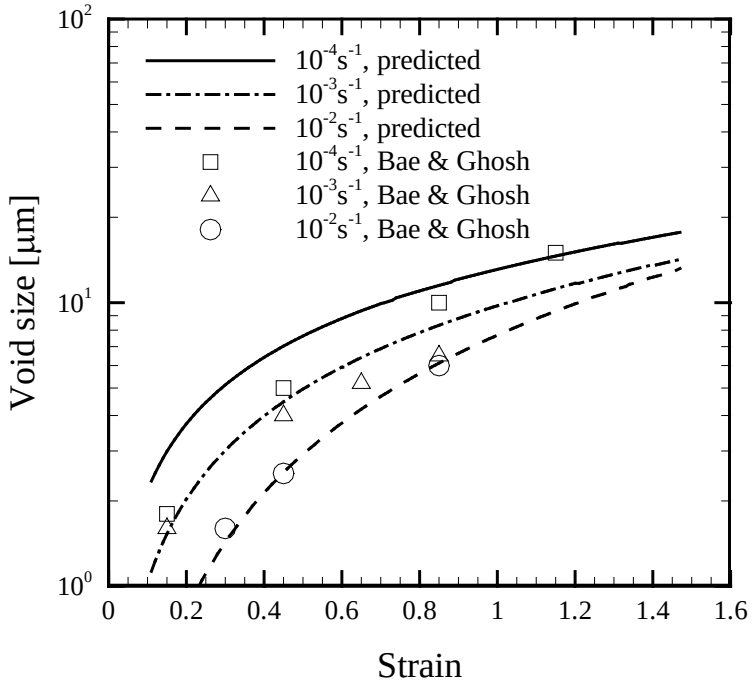

Figure 4-11 Void size as a function of strain with three strain rates. Initial void size is assumed to be 0 in the theoretical predication.

Chapter 5: Effect of Vacancies, Si and Mg impurities on Grain Boundary Sliding of Al Bicrystals at Elevated Temperature

Microstructure based simulations (Chapter 3 and Chapter 4) have demonstrated that grain boundary sliding contributes majority of the total strain during superplastic deformation. it is desirable to engineer the grain boundaries through techniques such as alloying to increase the contribution of grain boundary sliding to the total deformation and achieve improved formability. This requires fundamental understanding of the grain boundary structures and grain boundary sliding. In addition, the microstructure finite element model (Chapter 2) will be applicable to design microstructures for tailored formability, if the key parameters used in the model such as threshold stress studied in Chapter 3 can be predicted from atomistic simulations with little empirical data. This chapter examines the effect of grain boundary segregated vacancies and solute atoms (Si and Mg) on the sliding of a variety of grain boundaries at elevated temperature using molecular dynamics simulations.

It's well known that grain boundaries are often considered to be the sink or the source of defects that greatly influence the deformation behavior of polycrystalline materials. At elevated temperature (which is usually required for fine structure superplasticity and quick plastic forming), vacancies and impurities have great tendency

to segregate to grain boundaries due to energetic minimization [120]. Atomistic calculations [121-124] have also demonstrated that the vacancy formation energy at most lattice sites in the vicinity of grain boundaries in Al is lower than the its formation energy in the bulk, so these sites around grain boundaries will act as the sink for vacancies at the equilibrium state. Experimentally excess vacancies are found in grain boundaries in an Al-Mg-Mn alloy during superplastic deformation [125-127]. Vacancies in the vicinity of grain boundaries could also be produced by some procedures used to refine grain size [128, 129], which is often needed in the preparation of superplastic materials because superplasticity requires fine grain size. It is also common that the addition elements in superplastic alloys segregate to grain boundaries, either at equilibrium or during the deformation. In commercial purity Al AA5083 alloys, Si is the main segregant to the grain boundaries, and the concentration of Si at the grain boundaries increases with strain and decreases with deformation temperature [130]. Li et al [131] shows that the Si segregates to the Al grain boundaries and the segregants becomes more uniformly distributed in the grain boundaries with ultrasonic melt treatment. Equilibrium segregation of Sn and Zr to grain boundaries was observed at Al grain boundaries in a polycrystalline Al-Mg-Mn-Sn alloy at 450-550ºC [130, 132]. Mg was found to segregate to the grain boundaries at equilibrium [133] but depletes during the plastic deformation [130, 134]. It is thus important to understand the role of the segregated point defects during grain boundary sliding to provide helpful insight to grain boundary engineering.

While vacancies are known to have influence on grain boundary migration [135], direct experimental demonstration of their effect in grain boundary sliding is absent. Data for the effects of solute atoms on boundary sliding are available for both

polycrystalline Al alloys and individual grain boundaries by testing bicrystal or tricrystals, but are sometimes contradictory. Vetrano et al. [130, 134, 136] observed that Sn segregates to grain boundaries and enhances grain-boundary sliding in an Al-Mg polycrystalline material. Green et al. [137] measured an increase in creep rate from the acceleration of grain boundary sliding by Cu additions to an AA5083-based polycrystalline Al alloy. Weinberg [40] investigated the effects of small alloying additions of Cu (0.06–0.23%), Si (0.10%) and Fe (0.03–0.08%) in experiments on tricrystals and found no effect other than an inhibition of sliding by an addition of 0.08% Fe. Kato [43] studied sliding in bicrystals of Al-Cu solid solutions and noted that small Cu additions (0.2%) reduced boundary sliding, but this effect did not increase significantly with additional Cu (up to 0.5%). Mima, Oka and Nishi [138] studied bicrystals of Al individually alloyed with Mn (0.02–0.76%), Cu (0.06–3.92%), Mg (0.05–1.8%) and Zn (0.07–8.1%). They observed that small additions of Mn, Cu and Mg reduced sliding, but Zn reduced sliding to a lesser extent. However, sliding was enhanced at higher Mg and Zn concentrations, with large Zn additions increasing the sliding rate beyond that of the unalloyed material. Halliday and Beevers [44] studied boundary sliding in bicrystals of Al-Cu solid solutions (0.05 and 0.30% Cu), but observed no significant effect on sliding from Cu additions. Study of Zn bicrystals by Maruyama, Wananabe and Oikawa [139] showed a dramatic decrease in sliding at elevated temperature with Al solute doping. These results establish the fundamental importance of point defects on boundary sliding and demonstrate that in-depth understanding on how these point defects interact with grain boundaries and by what mechanism the defects affect the grain boundary sliding are clearly needed.

Some efforts have been made toward understanding the role of vacancy on grain boundary sliding. Molteni et al [140] used density function theory simulations to study grain boundary sliding by rigidly shifting one grain again the other. They found a variety of sliding behaviors, including coupling to migration, that depend not only on the delocalized character of the metallic bonding, but also on the boundary geometry, the local order, and the presence of a vacancy near the boundary. Lu et al. [123] studied a single vacancy in the vicinity of the grain boundary on grain boundary sliding and migration in Al by the Gamma-surface method. The simulation was done for quasi–static sliding by shifting the top grain rigidly relative the bottom grain and grain boundary energy is calculated after each step. They found that the existence of the vacancy hinders the grain boundary motion by tripling the energy barrier for grain boundary sliding and migration. The same approach was used to study the interaction of a vacancy and the grain boundary during quasi-static sliding at elevated temperature in both Al [141] and Cu [142, 143] Σ5(210)[001] grain boundary. In Al it was found that the grain boundary energy profile in the presence of a vacancy at the first plane (where the formation energy is lower than the bulk formation energy) is very similar to that of the clean grain boundary and is accompanied by grain boundary migration. On the other hand, a vacancy placed at the grain boundary plane (where the formation energy is higher than the bulk formation energy) increases the grain boundary energy during the sliding and leads to no migration. Similar results were found in Cu except that when the vacancy is placed at the grain boundary plane the interface will migrate so that to leave the vacancy in the first layer to minimize the grain boundary energy. Wang et al [144] studied the effect of three types of vacancies defects(point vacancy, line vacancy and cracks) on the

tensile and shear behavior of a bicrystal copper grain boundary and found that these defects strong influence on the interfacial behaviours. Specifically, vacancies near the grain boundary are found to lower the tensile strength of the structure but are found to have a more complicated effect on the shear strength. The weakening or strengthening effect of the vacancies when the structure is under shear is found to depend on the location of the vacancies. Monk el al [145] study the sliding of a S = 5 [001](310) symmetrical tilt boundary in bcc Fe with molecular dynamics simulations and found that vacancies and interstitials act as preferred nucleation sites for partial grain boundary dislocations that is needed for grain boundary sliding to occur. In addition, some atomistic simulations [146, 147] indicate that grain boundary unit structures with free volume which are similar to vacancies in the grain boundaries, play important role on grain boundary sliding by triggering atomic shuffling.

These studies give great insights to the role of vacancy in grain boundary sliding. However, there are a number of limitations to the current understanding of the effect of vacancies on grain boundary sliding. First, most calculations have focused on interaction of single vacancies and special grain boundaries, the effect of vacancy on general grain boundaries with various structure and energy is not yet addressed. Second, a lot of work is done with quasi-static energy minimization along the sliding path way and deduce the effect of vacancies on sliding by interpreting the vacancy effect on the grain boundary energy (the gamma-surface approach [120]). By quasi-statically forcing a relative displacement to the adjacent grains the sliding is confined to one specific path. This method is valid at zero or low temperature but it is questionable for the effect of vacancies at elevated temperature because the increasing number of possible sliding paths

due to the diffusion of vacancies. Finally, most of these works are done at zero or finite temperature. This is only suitable to materials what exhibits superplasticity at low temperature, such as nanocrystalline materials. Existence of vacancies at elevated temperature also will significantly affect the kinetic properties of the boundary, for example the diffusivity. The kinetic effect of vacancies on grain boundary sliding is still not yet addressed. For our interest of elevated temperature superplasticity, it is thus important to understand the interaction of vacancies with grain boundaries at elevated temperature.

Understanding of the effects solute atoms have on grain-boundary plasticity is very limited. Namilae et al. [30] studied sliding of symmetric tilt Al grain boundaries with molecular dynamics simulations and found that the magnitude of sliding shows a clear dependence on grain boundary energy, with high energy grain boundaries slide more. They also found that a Mg solute atom at particular positions near the grain boundaries will slightly increase the grain boundary energy and speculated that this will increase the ease of sliding. Atomistic simulations by Liu et al. [148] studied the segregation of Mg in $\Sigma 11(113)$ grain boundary and indicated that Mg atom prefers to occupy the 'looser' site at the grain boundary but not the 'tighter' site, and weakens the cohesion of the grain boundary. The implications of the solute Mg atom on sliding mobility are not spelt out.

The current lack of understanding of effect of point defects including vacancies and solute atoms on grain boundary severely limits our ability to engineer new alloys and develop novel thermalmechanical treatments that improves the formability. This chapter use molecular dynamics simulations to study the effect of grain boundary segregated vacancies and Si/Mg impurities on sliding of Al grain boundaries at 750K, respectively.

Previous molecular dynamics simulations [32] found that sliding of Al bicrystals strongly depends on the misorientaion of the adjacent grains, or grain boundary energy. In order to cover grain boundaries with various misorienations and grain boundary energies, we selected one Σ3 symmetric tilt grain boundary and asymmetric tilt grain boundaries with five different misorientation angles. Special attention has been paid to the effect of vacancies and impurities on the critical shear stress for grain boundary sliding to occur (or, the threshold stress) which is found to be a key physical quantity that influences the overall constitutive relation and the formability of the materials when grain boundary sliding is a dominant deformation mechanism [149]. Grain boundary sliding occurs only the resolved shear stress along the grain boundaries is greater than this critical value. Grain boundaries of two different defect concentrations are created and the threshold stresses for grain boundary sliding are estimated for both pure and doped grain boundaries.

1.13 Method of Simulations

Six different bicrystal structures are investigated in this paper, including one symmetric Σ3(111)[110] tilt grain boundary and five asymmetric [110] tilt grain boundaries with misorientation angles of 10°, 25°, 35°, 55°, and 90°. In the coincident-site-lattice (CSL) notation, the Σ3(111)[110] tilt grain boundary is formed through rotation of the two Al grains about the [110] tilt axis by 60°. The boundary is oriented along the (111) plane. The Σ3(111)[110] grain boundary of Al is simulated by the orthorhombic supercell shown in Figure 5-1(a). The supercell contains 2100 atoms

distributed in 50 (111) layers parallel to the grain boundary. The dimensions of the supercell along the [111] [120] [110] directions are 100.00Å, 34.78Å and 17.21Å, respectively. The asymmetric bi-crystal structures have the [110] directions of both grains in parallel and one grain is rotated around its [110] axis to generate tilt grain boundaries with mismatch angles of 10°, 25°, 35°, 55°, and 90°. Each grain boundary structure is non periodic in x-direction, which is perpendicular to the grain boundary plane, and periodic in the grain boundary plane along y- and z- directions. To maintain the periodic boundary condition, a common periodic cell length was chosen along y direction for all asymmetric grain boundaries. Each grain was about 56Å thick along the x direction.

Based on the as-built grain boundaries, some atoms in the grain boundary region are selected randomly and removed to create vacancies, or replaced by substitution impurities. The grain boundary region is defined as the region about 10 Å wide containing the grain boundary plane. This region usually contains about 2-3 layers of atoms on each sides of the grain boundary plane, depending on the specific grain boundary structure. For each grain boundary structure, vacancies or impurities of concentrations of 2% and 15% are introduced to the grain boundary region respectively. The concentration is defined by the number of vacancies or impurities normalized by the number of atoms at the grain boundary zone with 10 Å width.

After the grain boundary structures with vacancies were created, they are relaxed by constant temperature constant stress ensemble (TtN) to reach equilibrium temperature and zero stress. First the structures are relaxed at 300K for 25 ps. During this step, not only the atoms are relaxed locally by thermal vibration, but also the periodic length of the

simulation box in y- and z- direction. The equilibrium structures at 300K are then relaxed again at 750K, which is the desired temperature for grain boundary sliding, for 25 ps. The convergence of the energy is usually achieved within 5 ps and the grain boundary structures are in equilibrium state by the end of the two step relaxation.

The simulations of grain boundary sliding are conducted at 750K with non-equilibrium molecular dynamics. The temperature is kept constant at 750K with Nose-Hoover method [150-152]. Equal and opposite forces that are parallel to the grain boundary plane are applied on the two grains of each structure. As shown in Figure 5-1, constant forces in z- direction ([110]) are applied to the atoms inside the two boxes. Displacement in x- and y- direction of the outmost 1-2 atomic layers along the non-periodic (x-) direction is constrained in order to prevent free surface melting at high temperature and large vibration of the structure in x-y plane. These boundary conditions result a shear stress on the grain boundary. Series of tests were done for each grain boundary with various forces with and the relative displacement of the two grains, *d*, is recorded as a function of time. Threshold stress for grain boundary sliding is estimated using small brackets of applied shear stress. The grain boundary structures are judged to be able to slide when *d* is over 5 Å. On some rare occasions some low energy grain boundaries could initially slide but stop sliding when the grain boundary reaches a second equilibrium configuration. This is classified as no sliding.

The interaction between Al atoms is described by the Modified Embedded Atom Method (MEAM) potential, re-parameterized including the 2^{nd}-nerest neighbors [153]. The new parameters in MEAM potential correctly predict FCC as the lowest energy phase for Al, predicts Al surface energies in good agreement with first-principles DFT

calculations, and predicts melting temperature [32] which are important for high temperature simulations. The interaction of Al-Si and Al-Mg are simulated with MEAM potential by [154] and [155], respectively.

1.14 Results and discussion

1.14.1 Effect of Vacancies

Previously molecular dynamics simulations[32] found that the value of the threshold stress for grain boundary sliding is roughly inversed to the grain boundary energy, that is, grain boundaries with lower energy have higher threshold stress thus are more difficult to slide. Table 5-1 lists the grain boundary energy calculated at 300K for the six pristine grain boundaries in this paper. The grain boundary energy of <110> symmetric tilt boundaries as a function of misorientation has two deep energy cusps at the misorientation angles which correspond to (111)Σ3 and (113)Σ11 symmetric tilt boundaries. The grain boundary energy is calculated at 300K. Due to the coherent structure and good atomic fitting, Σ3 symmetric tilt grain boundary has the lowest grain boundary energy (0.073J/m^2 at 300K) and thus the highest threshold stress. Due to the high resistance on sliding, low energy grain boundaries are the limiting factors of the overall formability of the alloys. It is thus important to understand the sliding mechanisms in these grain boundaries to reduce the overall grain boundary sliding resistance of the material. The five asymmetric tilt grain boundaries all have grain boundary energy that is greater than 0.35J/m^2 and can be categorized as high energy grain boundaries [156]. In this section we will first discuss the effect of vacancies on grain

boundary sliding in the symmetric tilt Σ3 grain boundary. The effect of vacancies on all six grain boundaries and an outlook on vacancy effect in general grain boundaries will be discussed in the second part of this section.

1.14.1.1 Effect of Vacancies on Sliding of the Symmetric tilt Σ3 Grain Boundary

First, it is necessary to examine the distribution of the vacancies in the equilibrium grain boundaries after the two step relaxation. During the relaxation step, especially the relaxation at high temperature (750K), the originally randomly distributed vacancies can diffuse to lower the total energy of the GB structure. Figure 5-2 shows the number of atoms in each atomic layer in the equilibrium structure of the Σ3 grain boundary, with layer 0 as the grain boundary plane. It shows that for both structures the grain boundary layer has the highest concentration of vacancies. The number of vacancies roughly decreases with the distance to the grain boundary plane in each layer. For the structure with 2% vacancies, all the vacancies remained in the two atomic layers closest to the grain boundary plane. For 15% vacancy concentration, the maximum distance between the vacancies and the grain boundary layer is 6 atomic layers. The result indicates that vacancies tend to migrate toward and stay at the grain boundary vicinity and grain boundary is a sink for vacancies, which is consistent with both the vacancy formation energy calculations [121-124] and experimental observations[125].

The simulation results show that vacancies can significantly ease the sliding of Σ3 grain boundary. Figure 5-3 shows the relative tangential displacement of the grains as a function of time for the grain boundaries with or without vacancies when they are subjected to the same resolved shear stress (0.95GPa). This shear stress is not

sufficiently large to result in grain boundary sliding in the pure grain boundary structure, indicated by the fluctuating relative tangential displacement between the two grains. In contrast, the same applied shear stress results in sliding in the two grain boundaries doped with 2% and 15% vacancies. The amount of sliding distance at the same time is significantly larger in the grain boundary with 15% vacancies.

The structures of the three grain boundaries in response to the same applied shear stress(0.95GPa) were examined by taking snapshots of the grain boundaries at t = 0.85ps (shown in Figure 5-4). In the pure grain boundary (shown in Figure 5-4a), there is no significant slip between the two grains. The structure vibrates around an equilibrium position by pure elastic deformation of the grains and this results in the fluctuation of the relative grain displacement recorded in Figure 5-3. Figure 5-4b and c show that grain boundary sliding occurs in both grain boundaries doped with vacancies, however, the two grain boundaries slide in different fashions. In the grain boundary with 2% vacancies, the sliding is localized between two atomic layers in the grain boundary region. Grain boundary sliding occurs by stick slip between these two layers and the crystal structure on both sides of the grain boundary plane is well maintained during sliding. In the grain boundary with 15% vacancies the sliding involves several layers of atoms in the grain boundary region and the grain boundary becomes less ordered during sliding. Figure 5-3 and Figure 5-4 show that grain boundary sliding is much easier to occur when the grain boundaries contain vacancies, and the velocity of sliding becomes faster with larger concentration of vacancies.

The reduction in grain boundary sliding threshold by the presence of vacancies is found to be accompanied by the increase of grain boundary diffusivity. Figure 5-5 plots

the atomic root-mean-square-displacement (RMSD) in x-y plane of the three different structures under the same applied shear stress. The RMSD is given by

$$RMSD_i(dt) = \sqrt{\left\langle \sum_{t=0}^{T-dt} (r_i(t+dt) - r_i(t))^2 \right\rangle} \tag{5.1}$$

where r_i is the displacement of the atoms, dt = 0.1ps and the total time T = 50 ps. The RMSD is a measure of average atomic thermal displacement and hopping distance over time, and its linear slope with time is the measure of diffusion coefficient. The grain boundaries with vacancies show significant enhancement of RMSD in the grain boundary region compared to the pure grain boundary, with the peak of RMSD of grain boundary with 15% vacancies as high as 1.1. Traditionally peak value over 0.7 indicates grain boundary partial melting [32]. As shown in Figure 5-4c, the crystal structure of the grain boundary with 15% vacancies is disordered in the grain boundary region. In contrast, the crystal structure is well maintained in the pure grain boundary and grain boundary with low vacancy concentration under the same shear stress. This indicates that the premelting occurs due to excess vacancies in the grain boundary.

The increased diffusivity is indicated by the frequent vacancy hopping observed in grain boundaries with vacancies both during sliding and when the applied shear stress is below threshold stress(ie, when no sliding occurs). Note that due to the limitation of simulation time we cannot observe a clear direction of flux of the hopping vacancies, but nonetheless these random hopping events have great implications on the role of vacancies in the process of grain boundary sliding. Figure 5-6 contains the snapshots of the atomic layer adjacent to the grain boundary plane (layer number 1 in Figure 5-2) in the 2% vacancy structure during sliding at different time. Vacancy hopping both within the same

atom layer and between layers is observed. Vacancy A and B hop in the grain boundary plane during this time and vacancy C and D are generated from the out of plane hopping of the atoms. Figure 5-7 shows the snap shots of the grain boundary layer of the same grain boundary subjected to a shear stress that is below the threshold stress and with no grain boundary sliding occurs. Similarly with no sliding the vacancies can diffuse both in plane and out of plane.

Previously the effect of vacancy on grain boundary sliding was often studied by examining the change of grain boundary energy profile along the sliding path due to the presence of a single vacancy [123, 141-143] at zero or low temperature. A forced step by step relative displacement is applied on the adjacent grains. The structure is relaxed and the grain boundary energy is recorded after each step. The higher the energy barrier is along the sliding path, the more difficult for the grain boundaries to slide. This method was used to examine the sliding of symmetric tilt Σ5 grain boundary, a special high-energy grain boundary, parallel to the tilt axis in both Al and Cu[123, 141-143]. The results show that a vacancy in the grain boundary vicinity will increase the grain boundary energy barrier along the forced sliding path, and it will hinder the grain boundary sliding.

The threshold stresses of the pure grain boundary, grain boundaries with 2% vacancies and 15% vacancies are found to be 1.18GPa, 0.88GPa and 0.47GPa respectively in our simulation. The great reduction of threshold stress due to vacancies suggests that the energy barrier for grain boundary sliding at zero or low temperature can be overcome by the diffusion at elevated temperature. Vacancy hopping can effectively facilitate new grain boundary sliding path that have lower energy barrier when the grain

boundary is stressed, hence significantly reduce the threshold stress. This invalidates the "rigid-shift-minimization" method to simulate grain boundary sliding at elevated temperature. From another point of view, the stress required for "stick slip" fashioned sliding to occur has to overcome the cohesive energy of the two atomic layers, and this usually require relatively large stress. If the grain boundary contains enough vacancies then the diffusion of these vacancies can significantly reduces the cohesive energy of the atomic layers.

1.14.1.2 Effect of Vacancies on Sliding of General Grain Boundaries

In this section the effect of vacancies on all six grain boundaries used in this study is summarized. Figure 5-8 shows the effect of grain boundary vacancies of two different concentrations on the threshold stress for grain boundary sliding of all six grain boundaries. The threshold stress is plotted as a function of grain boundary energies of corresponding pure grain boundaries at 300K listed in Table 5-1. The overall the effect of vacancies on the threshold for grain boundary sliding in the five high energy boundaries is much less than in the symmetric Σ3 grain boundary, and this effect diminishes with increasing grain boundary energy. The threshold stresses for all the pure and vacancy doped grain boundaries are listed in Table 5-1. The maximum change in the threshold stress due to vacancies in the five asymmetric grain boundaries is 0.13 GPa with 2% vacancies at misorienation angle of 90°. This value is small compared to about ~0.7GPa drop of threshold stress in the symmetric Σ3 grain boundary with 15% vacancies.

The diminishing effect of vacancies on threshold stress with increasing grain boundary energy is consistent with the minimal change of diffusivity of high energy grain

boundaries due to vacancies. Figure 5-9 (a)~(e) shows the comparison of RMSD for pure and vacancy doped grain boundaries under the same applied stress for the five asymmetric grain boundaries. The applied stress is indicated on each plot and their value is the lowest stress where sliding has been observed. First, the initial RMSD at these grain boundaries are already in the ~0.6 region, which makes grain boundary sliding possible with a low stress. These plots show that the maximum value of RMSD in each grain boundary has no significant change due to the vacancies. This indicates that the grain boundary diffusivity is not significantly influenced by the vacancies in these grain boundaries. (It is also interesting to note that around threshold stress, the maximum RMSD of all five grain boundaries except for 25 is around 0.6).

1.14.2 Effect of Si and Mg Impurities

The effect of Si and Mg impurities on the threshold stress for sliding of Al grain boundaries is shown in Figure 5-11. The threshold stress is plotted as a function of the corresponding pure grain boundary energy calculated at 300K (shown in Table 5-1). The results show that Si impurities significantly decrease the threshold stress for grain boundary sliding in the three lower energy grain boundaries and have less effect in the higher energy grain boundaries. The effect of Si impurities is enhanced with increased concentration of Si. For example, the threshold stress of the symmetric tilt Σ3 boundary is decreased by 0.1GPa with 2% Si impurities, and by 0.9GPa (over half of the original value) with 15% Si impurities. The effect of Si impurities is not significant in the grain boundaries with 35, 55 and 25 degrees misorientation. These grain boundaries are more disordered and have very low threshold stress compared to the other three grain

boundaries. The results also show that Mg impurities increases threshold stress in all six grain boundaries by 0.2- 0.3GPa for all the boundaries regardless the concentration of Mg impurities. The relative tangential displacement of the grains as a function of time for pure and impurity doped Σ3 grain boundaries subjected to the same resolved shear stress is shown in Figure 5-10. Under the same shear stress, grain boundary sliding occurs in the grain boundary with Si impurities while the pure grain boundary and the Mg doped grain boundary show no sliding.

The effect of Si and Mg impurities on grain boundary sliding in Al grain boundaries are analyzed from the following two aspects:

First, in equilibrium grain boundary structures, Al atoms around Si impurities have much higher atomic energy than Al atoms around Mg impurities, and the lattice around Si impurities is visibly more distorted due to the interaction between Al and the impurities. Figure 5-12contains the contour plot of atomic energy of pure grain boundaries and grain boundaries with impurities at equilibrium. Although Si atoms has much lower atomic energy and Mg has much higher atomic energy than Al. The solute atoms were removed from the plots to have better comparison of the energy of Al atoms in the grain boundary vicinity. The plots show that the Al atoms in the vicinity of Si impurities have higher energy than the Al atoms in the pure grain boundary. They also show that the energy of atoms in the grain boundaries with Mg impurities is decreased compared to the pure grain boundary. The energy change of Al atoms around the solute atoms suggest that the Si impurities increase the mobility of surrounding Al atoms, and Mg decreases the mobility of the surrounding Al atoms. These observations of the effect of impurities on the equilibrium grain boundaries have great implication on the effect of

impurities on grain boundary sliding. Namelae et al [30] found an increase of Al grain boundary energy with the presence of a Mg impurity atom and that high energy grain boundaries exhibit more sliding in Al symmetric tilt grain boundaries. Our results suggest that the threshold stress for grain boundary sliding is likely to be correlated to how energized the Al atoms in the grain boundary vicinity are, instead of the grain boundary energy itself.

Second, the grain boundaries contains Si impurities have much higher grain boundary diffusivity. The effect of impurities on the grain boundary diffusivity is examined by calculating the root-mean-squared-distance. Figure 5-13 shows the calculated RMSD for the same grain boundaries and loading shear stress as in Figure 5-10. The grain boundary with Si impurities has the highest RMSD in the grain boundary vicinity. This indicates that the Si doped grain boundary has the highest grain boundary diffusivity. In contrast, the Mg doped grain boundary has the lowest grain boundary diffusivity. The change of diffusivity may have the direct influence on threshold stress for grain boundary sliding as discussed in the vacancy section.

To further investigate how the impurities interact with Al atoms, the relative distance of the impurities atoms and their nearest neighbors during sliding is recorded. Figure 5-14 shows the average relative distance over Si or Mg impurities in the grain boundaries normalized by the lattice constant as a function of loading time. The two grain boundaries are of 10 degrees misorientation and are subjected to shear stress 0.71GPa. Grain boundary sliding occurs in both Mg and Si doped grain boundaries under this shear stress. The plot shows that during sliding, the Si impurities separate with their initial nearest neighbors. By the time of 10ps the average distance of Si impurities and

their initial neighbors is over one lattice constant. In contrast, the Mg impurities are cluttered with surrounding Al atoms during sliding. Figure 5-15 shows the snapshot of the corresponding grain boundaries of Figure 5-14 during sliding. For moving boundaries Mg and Si show dramatically different behaviors in terms how they move with respect to their Al neighbors. Grain boundary sliding occurs in the atomic layers containing Si impurities in the Si doped grain boundary. In the Mg doped grain boundary, sliding occurs between the atomic layers that contain no Mg impurities. These results clearly show that Mg impurities form immobile particles with the surrounding Al atoms during grain boundary sliding.

1.15 Conclusions

Molecular dynamics simulations are used to investigate the effect of vacancies, Si and Mg impurities in the grain boundaries on grain boundary sliding. One symmetric tilt grain boundary and five asymmetric tilt grain boundaries are used. The threshold stresses of grain boundary sliding for these grain boundaries with vacancies of two different concentrations are estimated and are compared to the threshold stress for the corresponding pure grain boundaries. The following conclusions can be made from the simulations:

1. Vacancies in low energy grain boundary significantly decrease the threshold stress for grain boundary sliding by increasing the grain boundary diffusivity and that the effect is enhanced by increased concentration of vacancies. Vacancies of 2% concentration decreases the threshold stress of the symmetric tilt Σ3 grain boundary

from 1.18GPa to 0.88GPa, and vacancies of 15% concentration decreases the threshold stress to 0.47GPa. The effect of vacancies is less significant in high energy grain boundaries than in low energy grain boundaries and it diminishes as the grain boundary energy increases.

2. Si and Mg substitution impurities both have great influence on the sliding of Al grain boundaries but they operate by different mechanisms. The effect of Si is similar to vacancies: Si impurities greatly decrease the sliding threshold in high-energy grain boundaries by increasing energy/mobility of surrounding Al atoms and enhancing grain boundary diffusivity. Si impurities have less influence on low energy grain boundaries. Mg impurities increase sliding threshold of all grain boundaries independent of grain boundary energy by forming immobile clusters with surrounding Al atoms.

Table 5-1 List of the grain boundary energy at 300K and threshold stress.

		Threshold Stress (GPa)						
GB name	GB energy (J/m^2)	Pure GB	GB+ 2%V	GB+ 15%V	GB+ 2%Si	GB+ 15%Si	GB+ 2%Mg	GB+ 15%Mg
Σ3	0.07	1.18	0.88	0.47	1.11	0.34	1.27	1.33
110_90	0.43	0.88	1.01	0.93	0.74	0.55	1.14	1.01
110_10	0.45	0.69	0.75	0.69	0.62	0.34	0.80	0.69
110_35	0.51	0.02	0.01	0.08	0.04	0.06	0.07	0.13
110_55	0.52	0.07	0.07	0.04	0.02	0.01	0.07	0.15
110_25	0.55	0.02	0.02	<0.01	0.01	0.04	0.11	0.21

(a)

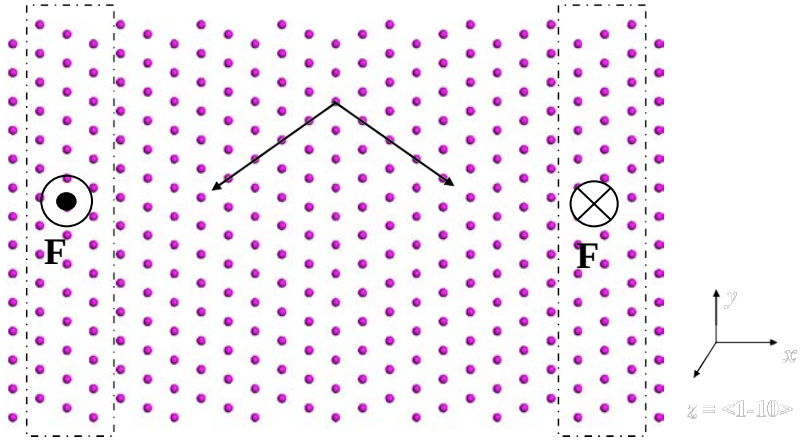

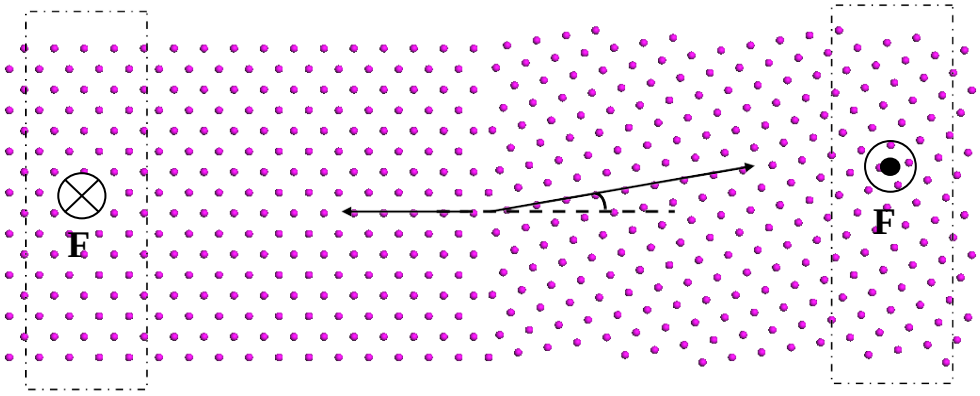

(b)

Figure 5-1 As-built grain boundary structures. (a) symmetric tilt Σ3 grain boundary (b) asymmetric tilt grain boundary with rotation angle θ, θ can be 10, 25, 35, 55 and 90 degree. Each grain boundary structure are divided into three zones along x- direction: fixed zone (the outmost layers on both sides); the force applying zone (indicated by the dash-dot boxes); and the free zone (all other atoms).

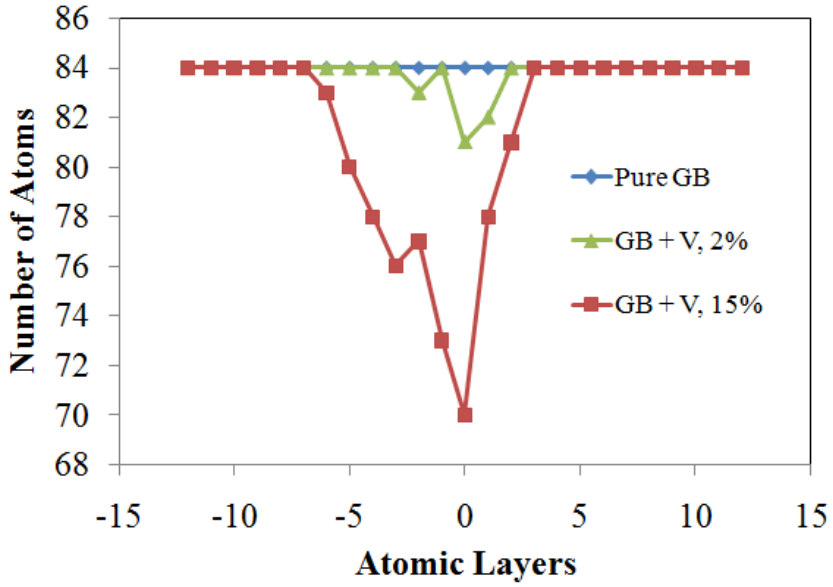

Figure 5-2 Number of atoms in each atomic layer for ∑3 grain boundaries after relaxation.

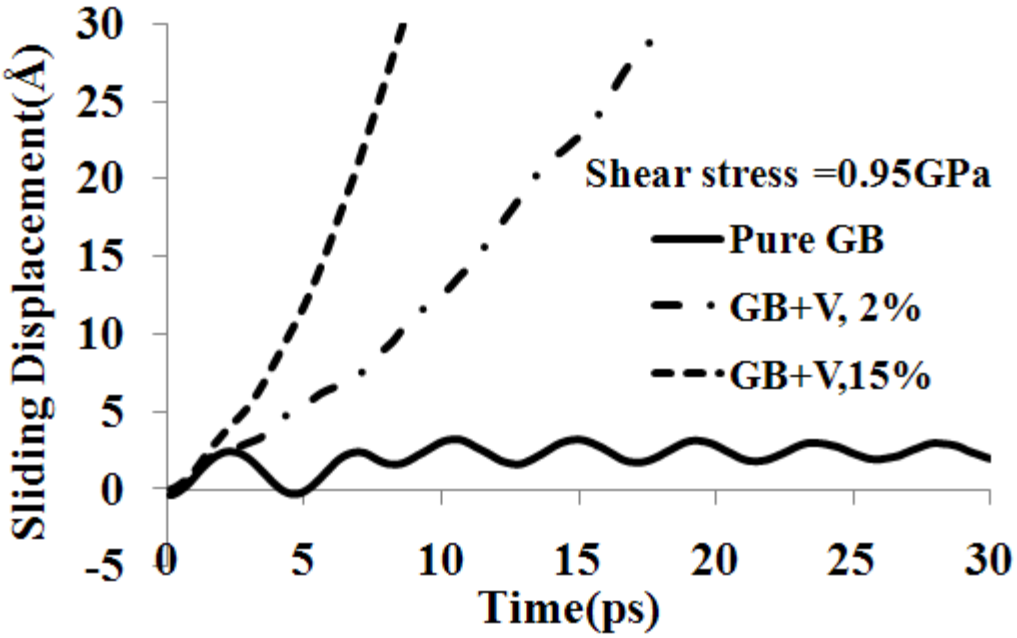

Figure 5-3 Comparison of relative tangential displacement of the grains as a function of time in pure ∑3 grain boundary and grain boundary with different vacancy concentrations.

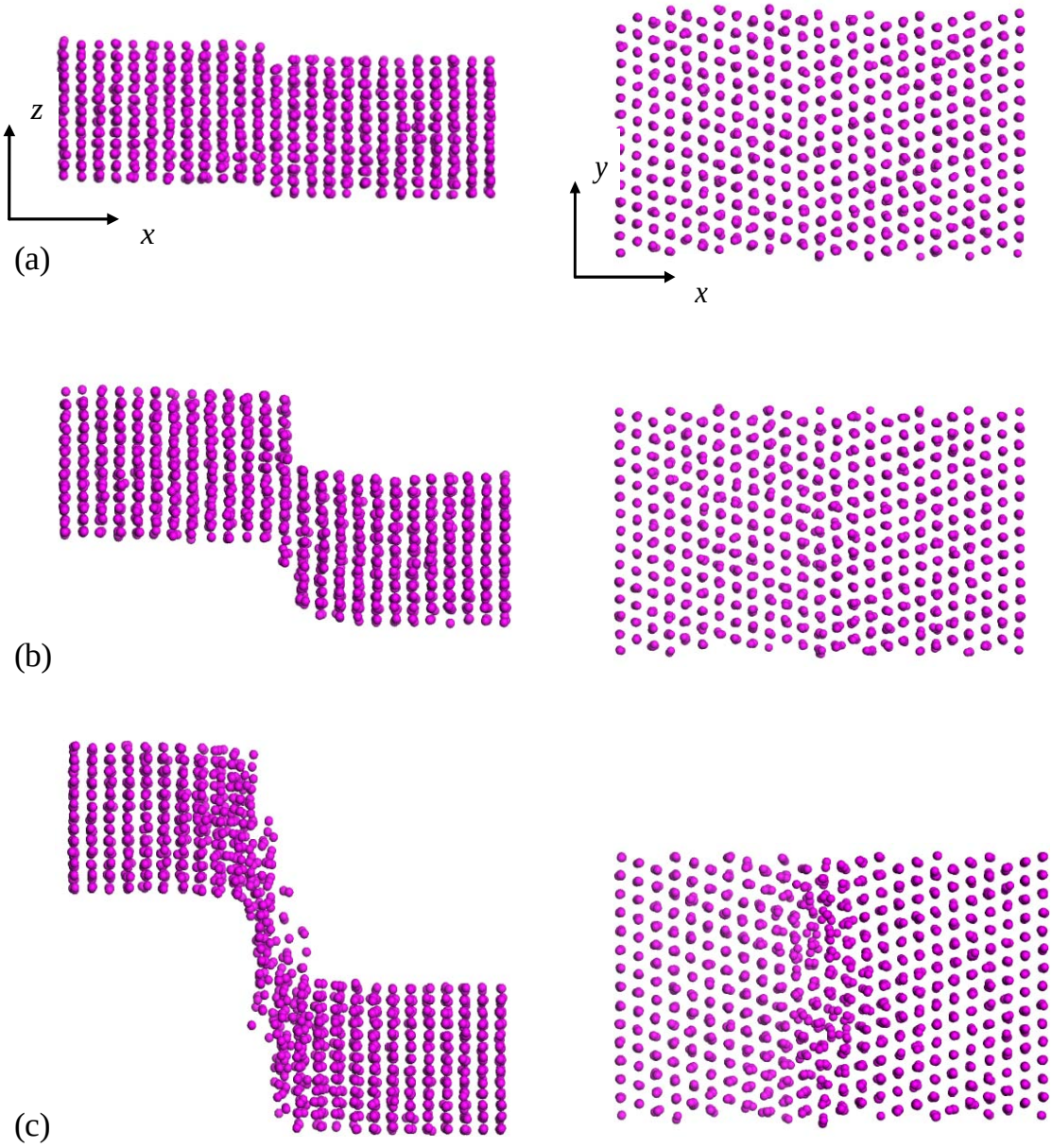

Figure 5-4 Snapshot of grain boundary structure in x-z plane and x-y plane at 8.5ps under shear stress of 0.95 GPa of (a)pure grain boundary (b)grain boundary with 2% vacancies (c) grain boundary with 15% vacancies.

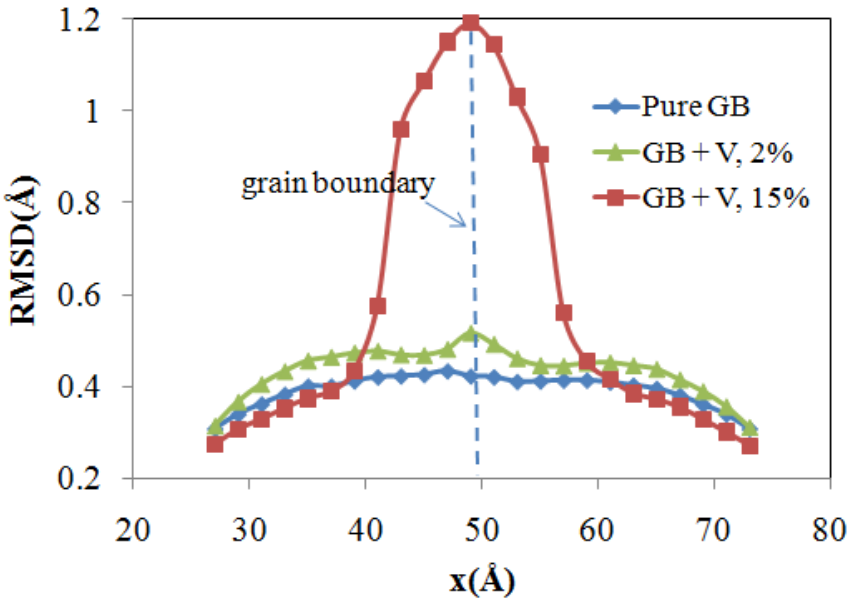

Figure 5-5 Comparison of Root Mean Squared Distance(RMSD) for pure $\Sigma 3$ grain boundary and two vacancy doped grain boundaries under shear stress of 0.95GPa with Δt= 1ps over 50ps.

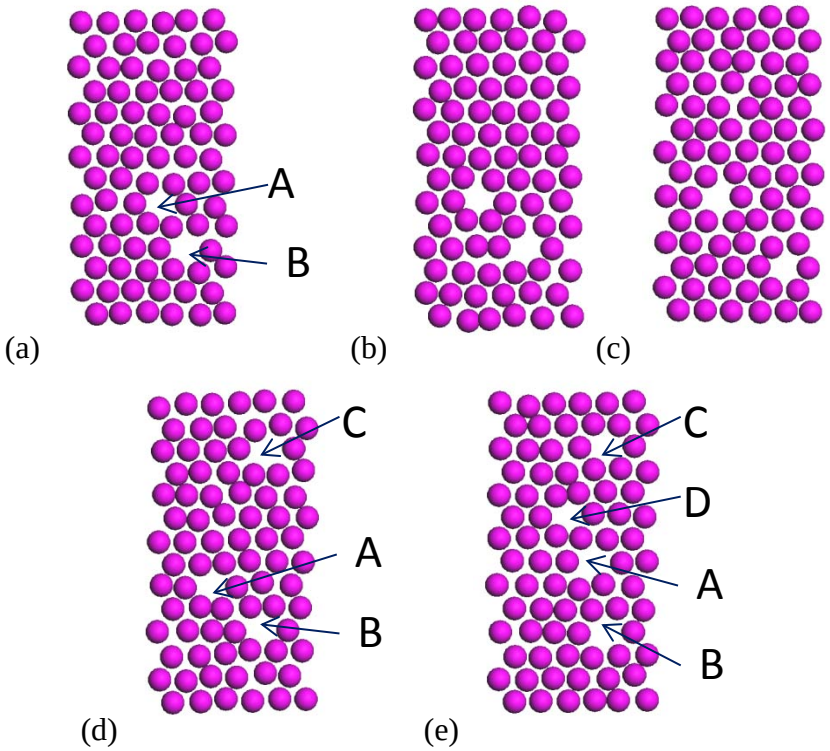

Figure 5-6 Snapshot of the Atomic layer 1 (the layer adjacent to grain boundary layer) in y-z plane of the 2% vacancy structure under stress of 1.08GPa at (a) 0.1ps (b) 3.2ps (c) 4.6ps (d) 17.4ps (e) 20.1ps.

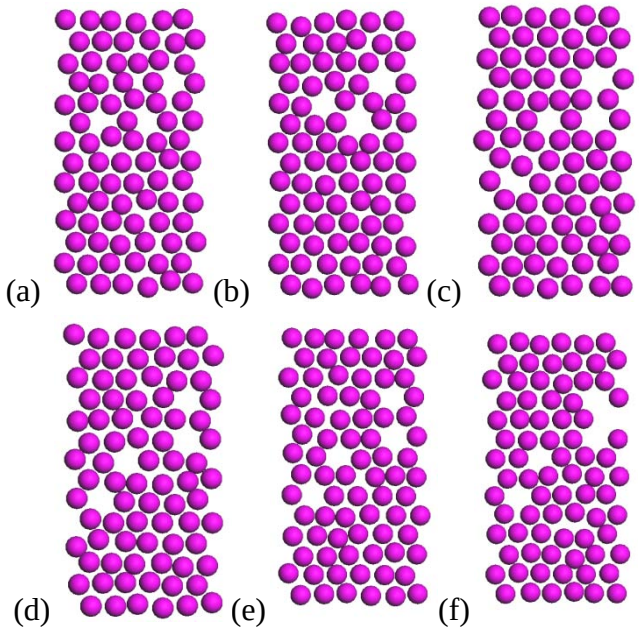

Figure 5-7 Snapshot of the grain boundary layer in y-z plane of the 2% vacancy structure under stress of 0.81GPa at (a) 0.1ps (b) 1.0ps (c) 2.0ps (d) 3.0ps (e) 4.0ps (f) 5.0ps.

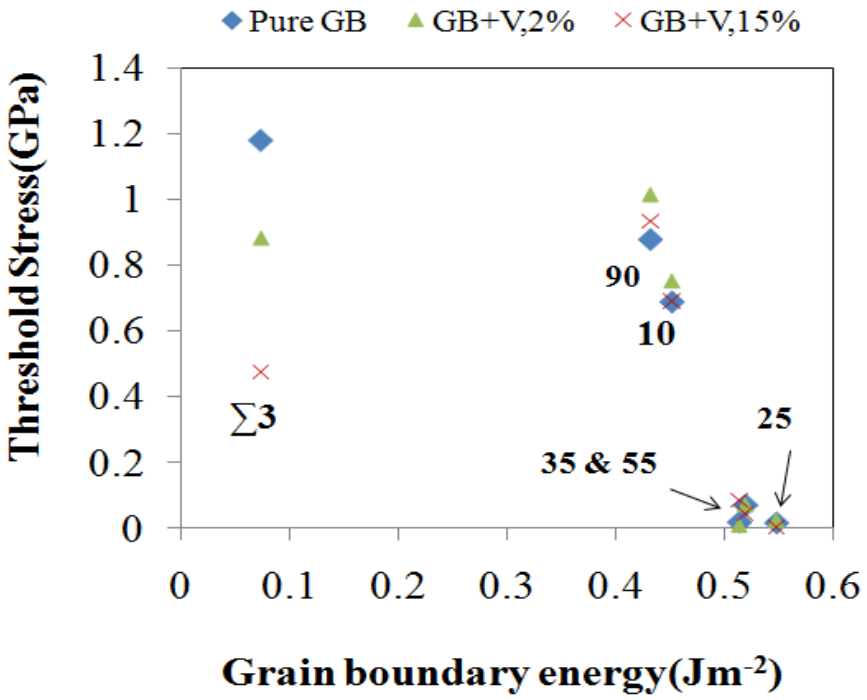

Figure 5-8 Effect of 2% and 15% vacancies on threshold stress for grain boundary sliding for grain boundaries with various misorientation angles.

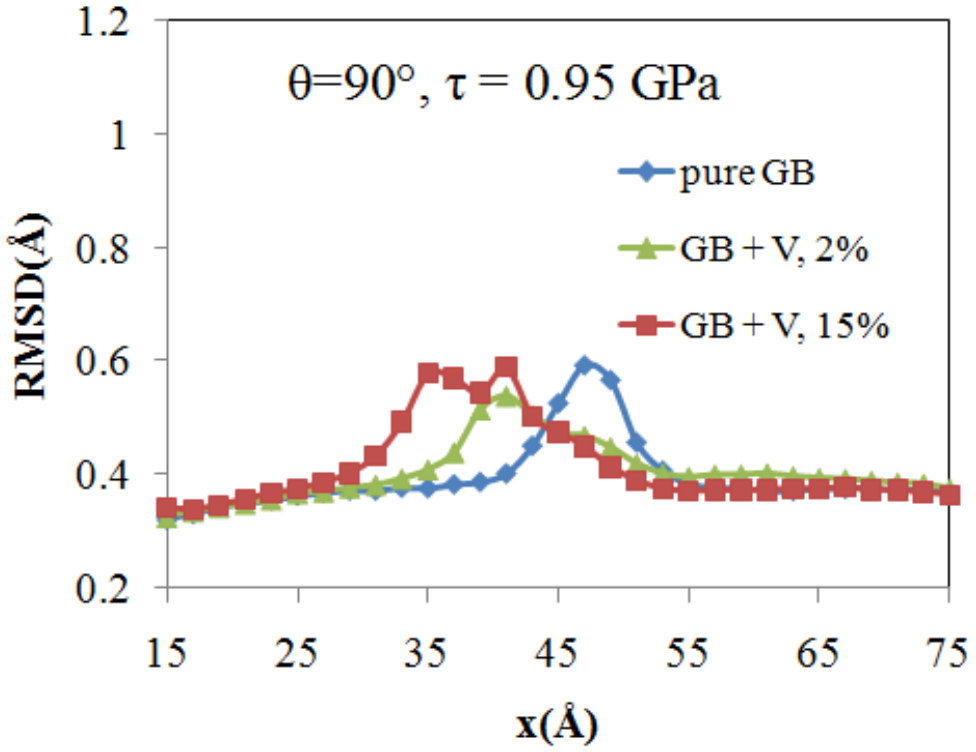
θ=90°, τ = 0.95 GPa
pure GB
GB + V, 2%
GB + V, 15%
RMSD(Å)
x(Å)
1.2
1
0.8
0.6
0.4
0.2
15
25
35
45
55
65
75

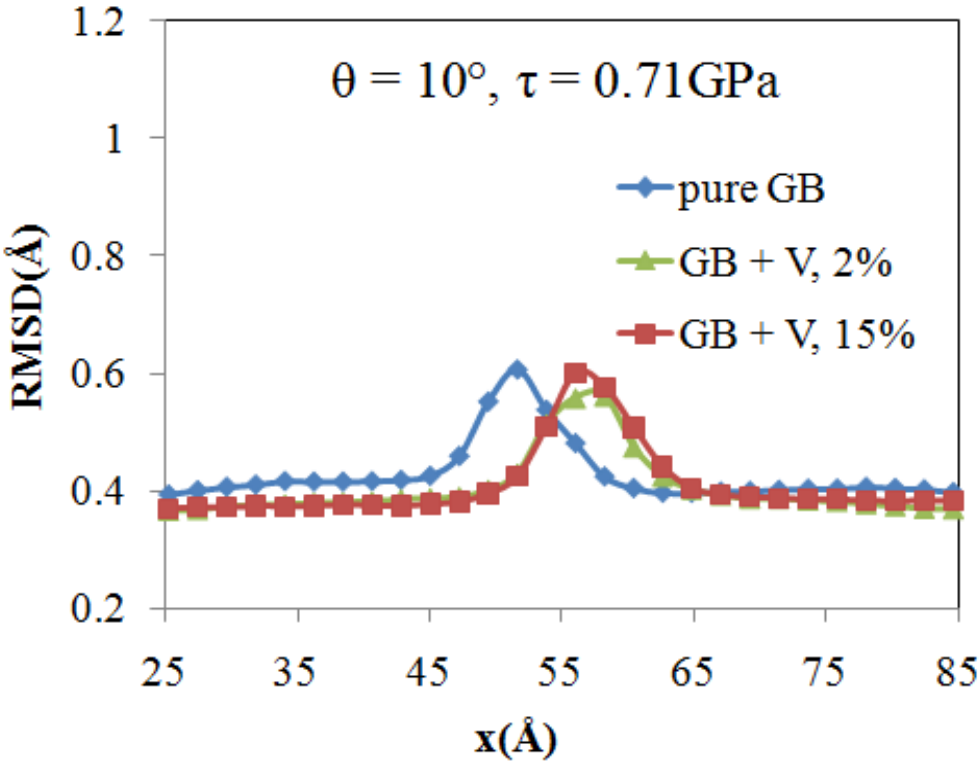
θ = 10°, τ = 0.71GPa
pure GB
GB + V, 2%
GB + V, 15%
RMSD(Å)
x(Å)
1.2
1
0.8
0.6
0.4
0.2
25
35
45
55
65
75
85

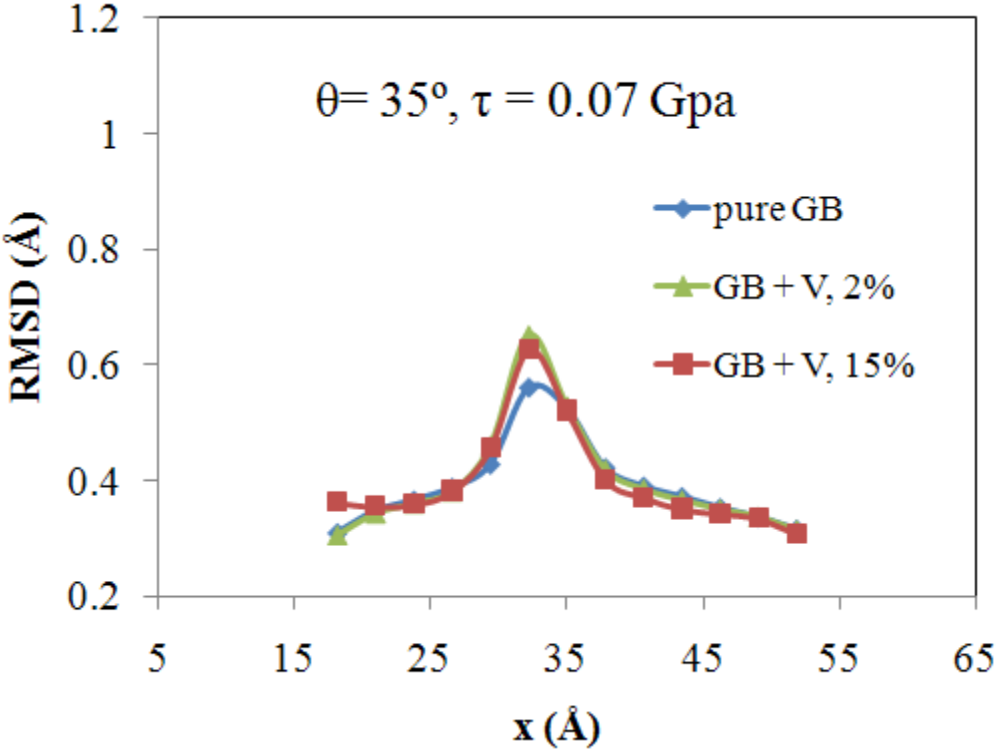
θ= 35º, τ = 0.07 Gpa
pure GB
GB + V, 2%
GB + V, 15%
RMSD (Å)
x (Å)
1.2
1
0.8
0.6
0.4
0.2
5
15
25
35
45
55
65

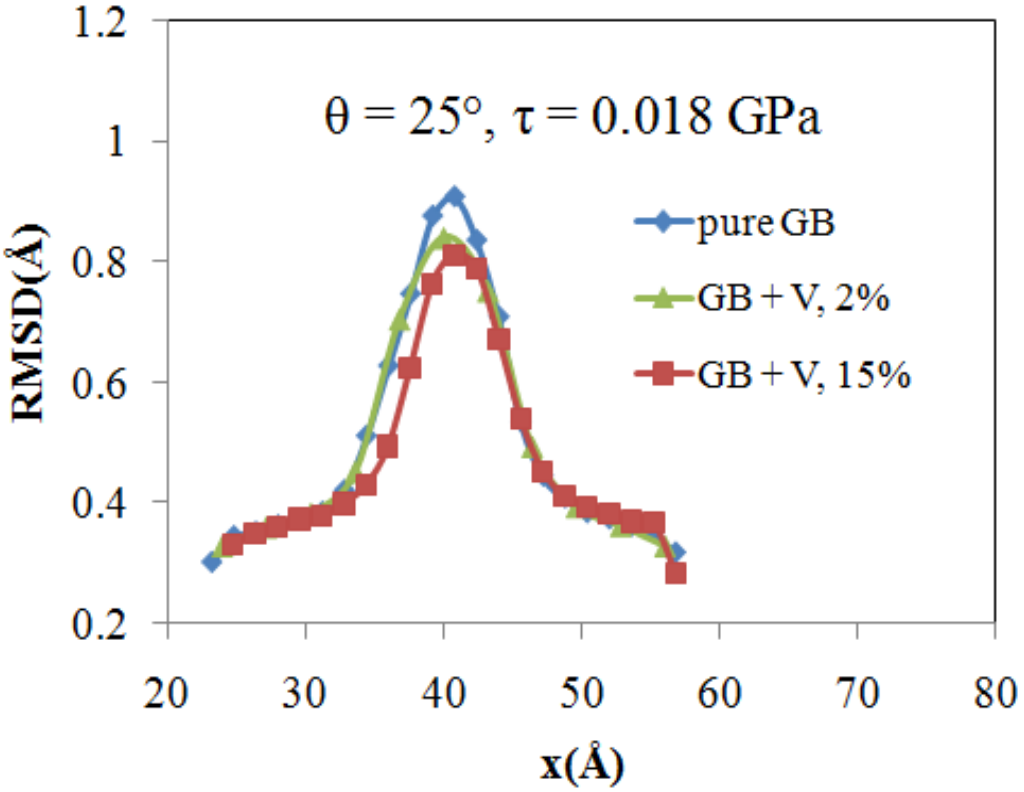
θ = 25°, τ = 0.018 GPa
pure GB
GB + V, 2%
GB + V, 15%
RMSD(Å)
x(Å)
1.2
1
0.8
0.6
0.4
0.2
20
30
40
50
60
70
80

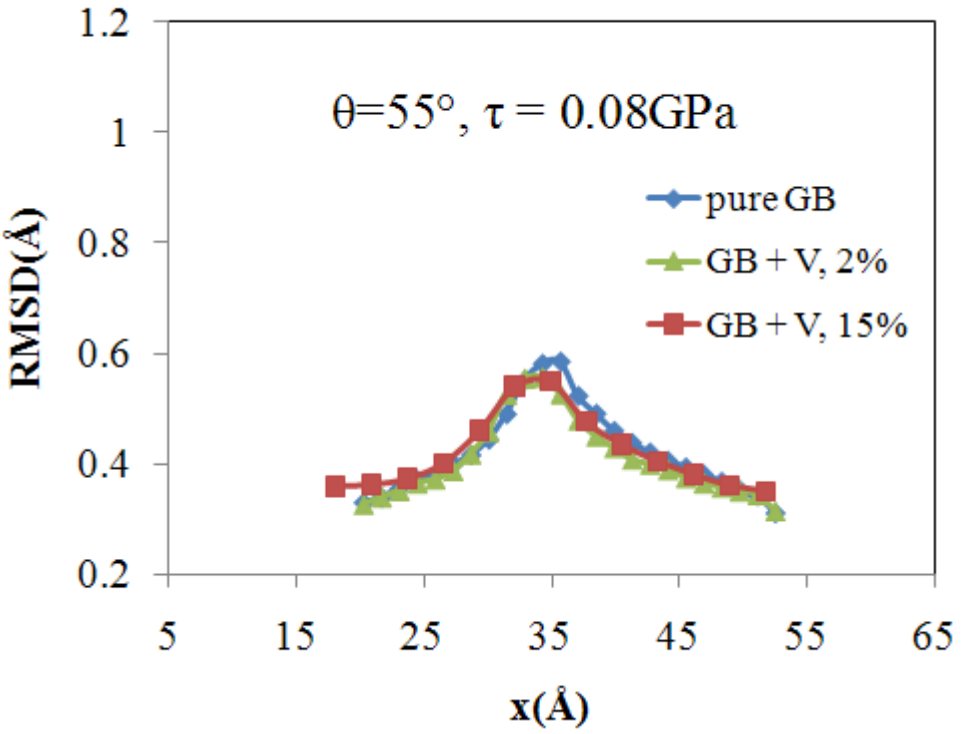

Figure 5-9 Comparison of RMSD for five asymmetric tilt grain boundaries for pure and vacancy doped structures. The pure grain boundaries are blue diamonds, grain boundaries with 2% vacancy are green triangles and with 15% vacancy are red squares. All shear stress are selected to be just above the threshold stress, or close to the threshold stress.

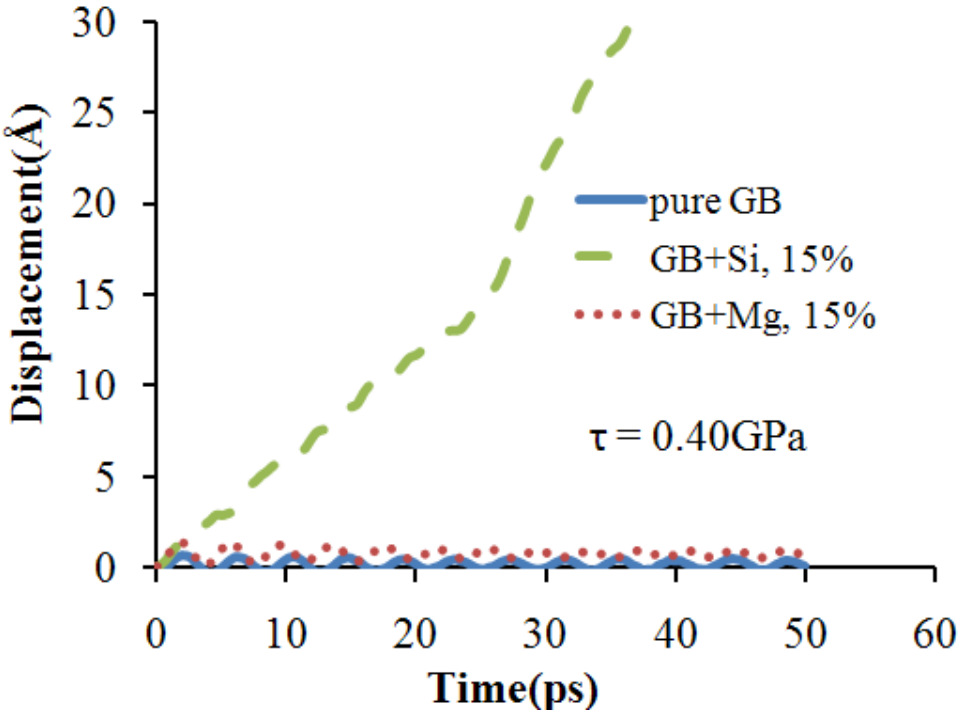

Figure 5-10 Relative tangent displacement of two grains as a function of time for Σ3 grain boundaries.

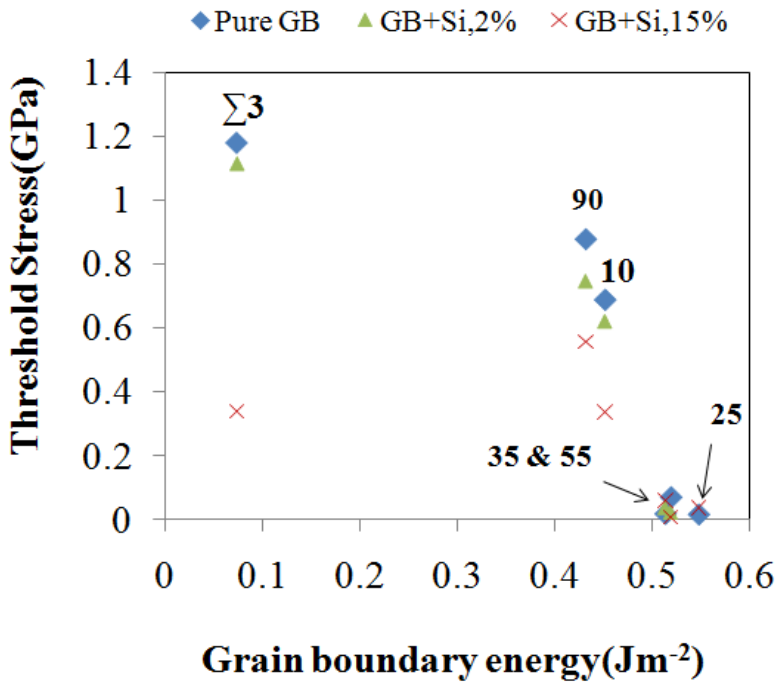

(a)

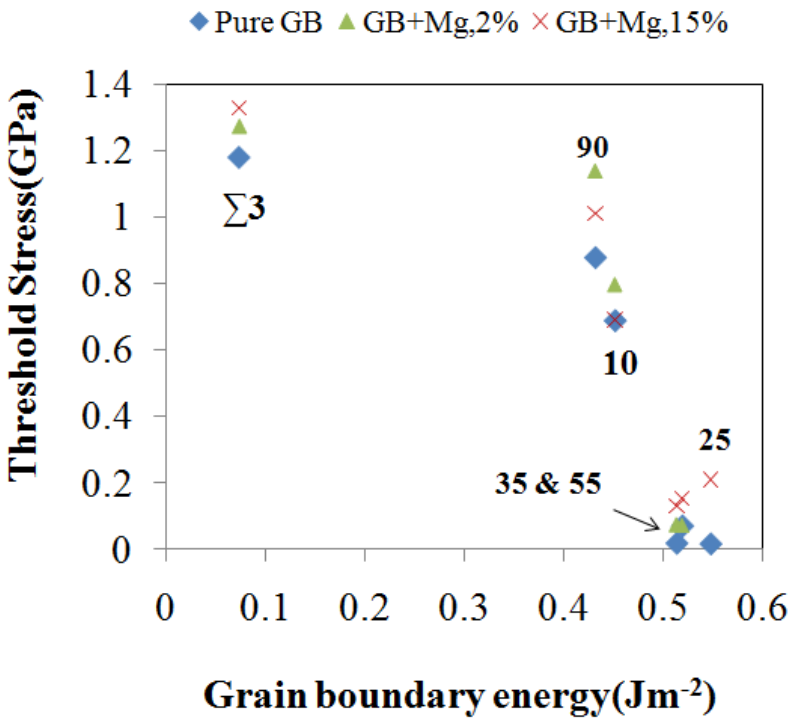

(b)

Figure 5-11 Effect of impurities on threshold stress in all six grain boundaries (a) Si impurities (b) Mg impurities.

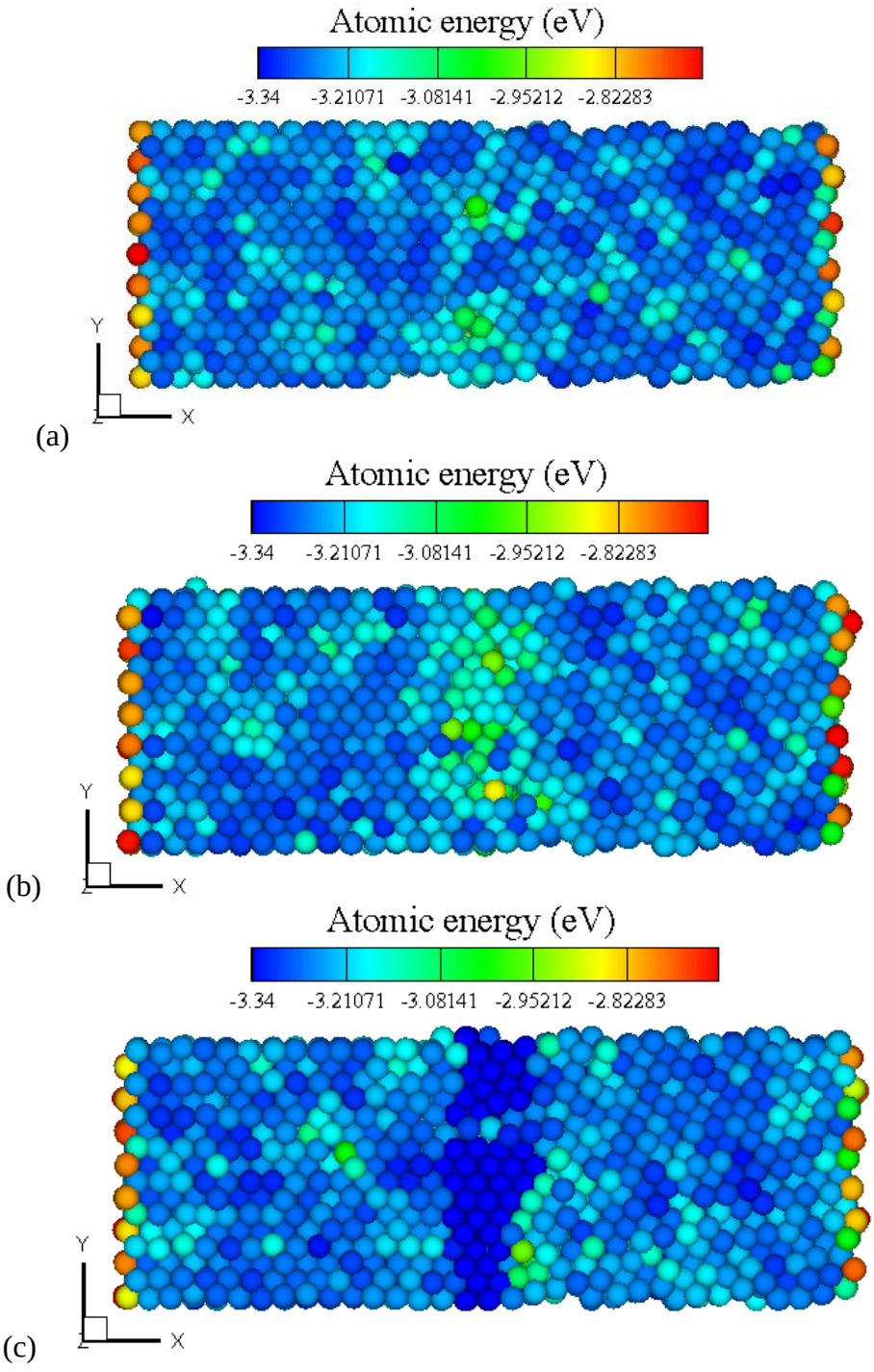

Figure 5-12 Contour plot of atomic energy of the grain boundary with misorientation 10 degrees with 15% solute (a) pure GB (b) Si (c) Mg. Note that the solute atoms are deleted from the structures.

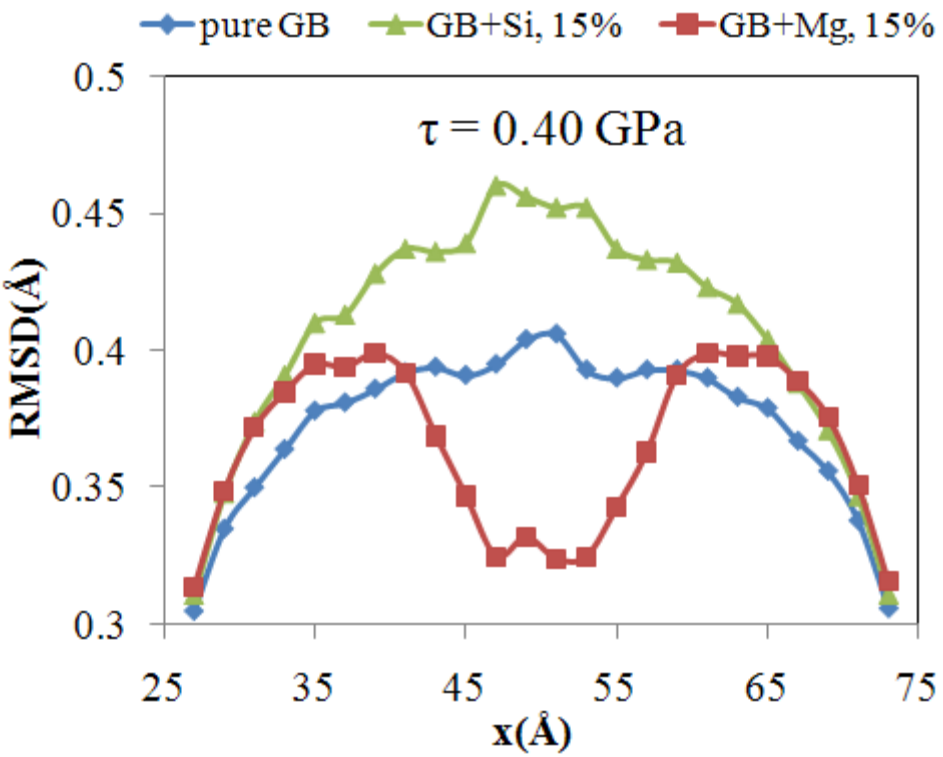

Figure 5-13 Effect of impurities on the RMSD of Σ3 grain boundaries.

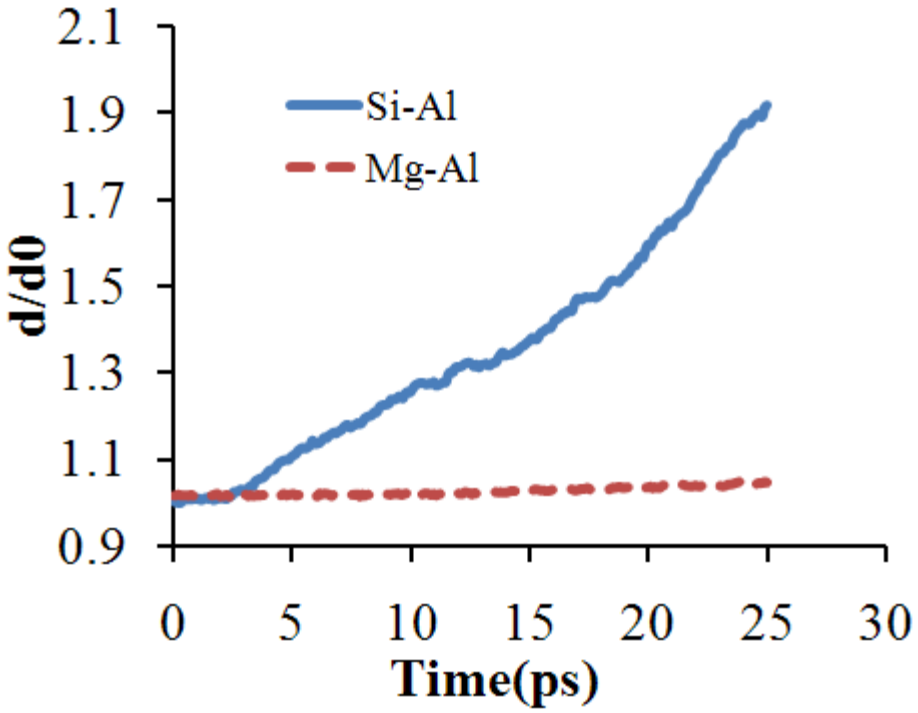

Figure 5-14 Average distance between impurities and their neighboring Al atoms during sliding. misorientation 10 degree with 15% impurities and shear stress = 0.71 GPa.

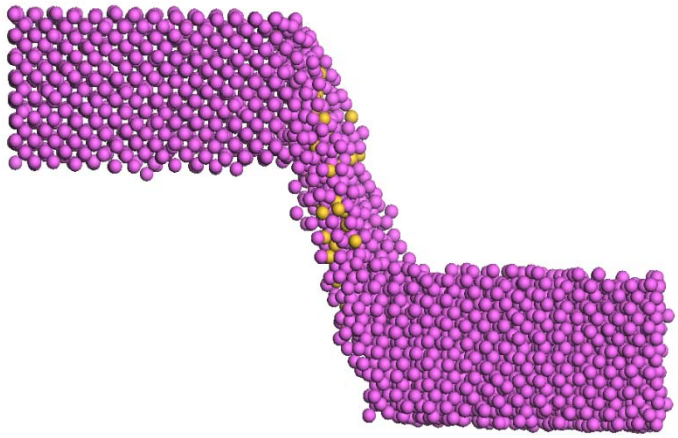

(a)

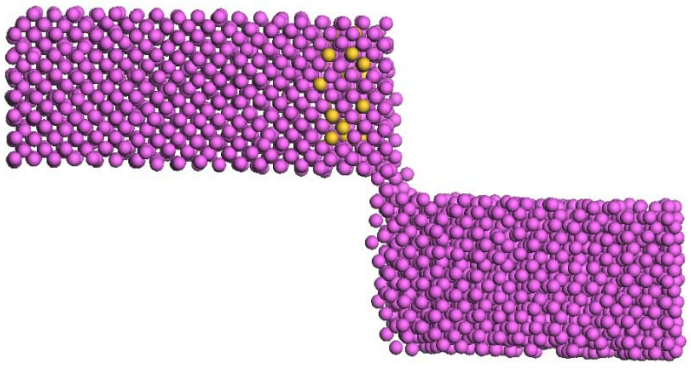

(b)

Figure 5-15 Snapshot of grain boundaries at 25 ps. Misorientation 10 degree with 15% impurities and shear stress = 0.71 Gpa. (a) grain boundary with Si impurities; (b) grain boundary with Mg impurities.

Chapter 6: Effect of Grain Size on Bulge Forming of Al AA5083

The microstructural finite element model (Chapter 2) has been used to predict the constitutive relation of superplastic materials, the contribution of various deformation mechanisms (Chapter 3), and investigate void growth (Chapter 4) in these materials based on grain level microstructures. The ability to predict directly the influence of a materials microstructure features such as grain size or texture on its behavior during a realistic forming process is still lacking.

In this chapter, a multi-scale approach that links the microstructure level simulations to continuum level simulations is devised and used to investigate the effect of grain size on gas pressure bulge forming of Al AA5083 at elevated temperature. The approach is experimentally validated and the results show that the predicted bulge height with the multi-scale approach agrees well with experiments. This multi-scale approach represents a first step toward incooperating microstructure features in the simulations for elevated temperature forming of Al alloys.

1.16 Procedure

The goal of this paper is to validate experimentally a multi-scale approach to predicting the influence of grain size on high temperature forming of AA5083. The multiscale simulations are based on a two step process. First, the microstructure based model, which accounts explicitly for the effects of grain boundary sliding, diffusion and solute drag creep in a model polycrystal of AA5083, is used to predict the uniaxial stress-v-strain rate for materials with grain sizes ranging from 7 to 82 microns. The stress-v-strain rate curves are fit with a phenomenological power-law creep relation, which is then implemented in a commercial finite element code. The finite element simulations are used to simulate dome forming, and also to simulate hot blow forming of a representative 3D part, for materials with each grain size. To validate the predictions, materials with the same range of grain sizes were created and were tested in uniaxial tension, dome forming, and in a representative 3D forming process. A direct comparison was made between

1. the measured uniaxial stress-strain behavior and the predictions of the microstructure based model;
2. the dome height predicted by the multi-scale simulations and the experimental measurements.

1.16.1 Computational

The multi-scale approach consists of two steps of finite element simulations on different length scales.

First, the microstructure based finite method described in Chapter 2 was used to predict the constitutive behavior(ie, the stress-strain rate relationship) of AA5083 materials with various grain sizes. The microstructure shown in Figure 3-1, which was taken directly from a micrograph of the specimen, was used to predict the constitutive relation. This ensured that the grain geometry used in the simulation is independent of the method used to measure grain size. The microstructural model was first calibrated by the measured uniaxial tension stress-strain rate curve of the material with the finest grain size, 7 micron. The method of the calibration was described in Chapter 3 and the resulting list of parameters is listed in Table 6-1. These parameters were selected to fit the predictions of the model to the experimentally measured flow stress-vs.-strain rate curve for AA5083 with a 7.0μm grain size and to meet the condition that the deformation mechanism must transition from dislocation creep to grain boundary sliding at a strain rate of 10^{-3} s^{-1} in the 7.0μm grain size material. In previous studies, the grain boundary fluidity was estimated using the Raj-Ashby [13] model of grain boundary sliding. In this

work, the fluidity was selected to predict the correct flow stress for the 81.7μm grain size material at a strain rate of 10^{-3} s^{-1}. The calibrated microstructure-based model together with the decided parameters was then used to predict the steady state uniaxial flow stress-v-strain rate for materials with the five other grain size, 9.2, 11.2, 22.3, 37.2, and 81.7 micron. These materials were created by scaling the dimensions of the microstructure shown in Figure 3-1 by an appropriate factor.

Second, continuum scale finite element simulations performed with ABAQUS^{TM}6.5.6 was used to simulate the gas-pressure bulge forming to obtain the variation of dome height with grain size. The stress-vs.-strain rate response predicted by the microstructural finite element model was fit by a phenomenological power-law creep equation (for each separate grain size) with the form

$$\dot{\varepsilon} = A_1 \bar{\sigma}^{n_1} + A_2 \bar{\sigma}^{n_2}, \tag{6.1}$$

where $\bar{\sigma}$ is the modulus-compensated flow stress, $\dot{\varepsilon}$ is the strain rate, A_1, A_2 and n_1, n_2 are constants that vary with grain size. The coefficients A_1, A_2 and the exponents n_1 and n_1 in the above equation were determined using the Nelder-Mead method. Here the relative error

$$(\dot{\varepsilon} - \dot{\varepsilon}_{FE})^2 / (N\dot{\varepsilon}_{FE})^2 \tag{6.2}$$

is minimized, with $N > 0$ an arbitrary constant and $\dot{\varepsilon}_{FE}$ computed from the numerical model.

The phenomenological constitutive equation was then used to define the constitutive relation of the materials in continuum scale finite element simulations. The material was idealized as an elastic-viscoplastic solid, with modulus of elasticity 52 GPa and Poisson's ratio 0.33. The plastic response of the material was idealized using a von-Mises flow potential, with effective strain rate vs. stress behavior given by equation (6.1).

The die had a 100 mm inner diameter, a 150 mm wide flange, and a 5 mm fillet radius. The circular sheet, which was clamped along the outer circumference of the die flange, had a 114 mm radius. The sheet thickness was chosen to match the experimental data, listed in Table 6-2. The sheet mesh consisted of membrane elements of type M3D4, whereas the die mesh included 6319 rigid elements of type R3D4. To eliminate the normal direction singularity condition due to the initially flat sheet geometry, an elastic response was assumed at the outset of each simulation by applying a linear ramp to full pressure over one second; the plastic response was subsequently calculated for the duration of the simulation. The pressure applied in each simulation (determined from experiment) was listed in Table 1. In all cases, zero sheet-die friction was assumed and forming was terminated at 1800 s. Failure was not considered in any of the simulations.

It is worth noting that the simulations are independent of the experiments, in that the microstructure-based model was calibrated using data for AA5083 with single grain size (7 micron), and was then used to predict behavior for all other grain sizes. This prediction can thus be verified by independent experiments.

For comparison purposes, a separate set of values for A_1, A_2 and the exponents n_1 and n_1 were also determined by fitting directly to the experimentally measured stress-vs.-strain rate curves, and were used to predict the bulge height.

1.16.2 Experimental

The material used for the present study was 1.6 mm, AA5083-H18 produced with a nominal composition of (Al - 4.6w/o Mg – 0.8w/o Mn – 0.1w/o Cr). Materials were evaluated in six different conditions representing average grain sizes of 7.0, 9.2, 11.2, 22.3, 37.2, and 81.7 μm. Grain size is represented as an average linear intercept length. Grain size was varied by using critical strain annealing. The material was first recrystallized for 15 min. at 500ºC. This produced a substantially strain-free condition with an average grain size of approximately 7.0 μm. Following cold rolling reductions of 0 to 80%, the material was then recrystallized again for 15 minutes at 450ºC to produce a larger grain size than the initial starting structure. The material exhibits classic critical

strain annealing behavior observed in aluminum [157]. Six conditions were selected as shown in Figure 6-1 with images taken through the thickness of the sheet. The rolling direction is horizontal in all images. All six materials had relatively uniform grain distributions through the thickness of the sheet. The sheet thickness varied between 1.05 mm and 1.6 mm depending on the amount of cold reduction. Metallographic samples were aged for 24 h at 150ºC, mounted, polished, and etched by immersion in 10% phosphoric acid solution at 50ºC to reveal the grain boundaries. Grain size was measured using ImagePro™software and ASTM standard E112 with concentric circles.

An Instron model 5568 screw-driven test frame, with an Instron 3119-007 furnace and a Merlin data acquisition system were used for elevated temperature tensile testing. The gage section of each tensile specimen was aligned with the rolling direction. Specimen dimensions were 25.4 mm wide x 63.5 mm long with a 6.4-mm-wide x 25.4-mm-long gage section following ASTM E 2448-06. Each was allowed to equilibrate in the furnace at the 450ºC testing temperature for 15 min. prior to testing. Both constant-strain-rate and step-strain-rate tests were conducted, and each was followed by an immediate water quench**.** The constant-strain-rate tests at 450ºC, performed at 0.0003, 0.001, 0.01, 0.1, and 0.3 1/s, enabled investigation of tensile curve shape, total elongation and work hardening behavior. Results were reported as the average of five specimens

under each test condition. Data are reported as true stress and true strain; however, the true stress values that are shown after the onset of instability are approximate and do not account for localized necking. Step strain rate tests were performed to determine the effect of strain rate on flow stress and the strain rate sensitivity.

Biaxial bulge tests were performed using the experimental procedure detailed in [158]. A 150 mm square blank was used in the test. The blank was placed in the bulge die, allowed to heat to the forming of 450ºC and then clamped. Temperature was monitored using a thermocouple and the nominal preheat time was approximately 5 minutes. A constant gas pressure was then applied as listed in Table 6-2. Forming was terminated after 1800s.

1.17 Results

The measured uniaxial stress – strain rate curves for all six materials are shown in Figure 6-3. The six materials can be classified into three groups according to the uniaxial response. The two fine-grained materials (7.0μm and 9.2μm) exhibit a transition in behavior from a creep stress exponent of ~4 at high rates, where deformation is mainly due to dislocation creep, to ~2 at lower strain rates, where deformation is mainly due to

grain boundary sliding. In contrast, the stress exponent for the three coarse grained materials (22.3μm, 37.2μm and 81.7μm) remains almost constant throughout the strain rate range. The material with grain size 11.2μm represents a transitional material from fine grained type response to coarse grained type response. It should be noticed that at fast strain rates, although both fine grained materials and coarse grained material exhibit a stress exponent of ~4, hence the deformation in both types of materials is dominated by dislocation creep, the flow stress increases with grain size. The steepest increase of flow stress seems to occur between 11.2μm material and 22.3μm material.

The uniaxial response predicted from the microstructure based model is compared for representative fine grained material, coarse grained material and transitional material (7.0, 11.2, and 81.7μm materials) in Figure 6-4. The simulation curve for 7.0μm is calibrated against the experimental data and the flow stress is predicted for materials with other grain size. The prediction for all three materials agrees very well with the experimental results in terms of both the flow stress and the stress exponent. The model successfully captures the following aspects of the experiments:

1. The increase of stress exponent with strain rate for both fine grained material and transitional material;
2. The constant stress exponent for coarse grained material;

3. The dependence of the flow stress on grain size at both low strain rates and high strain rates. The dependence of the flow stress on grain size is further illustrated in Figure 6-5. It is clear from Figure 6-5 that the model predicts satisfactory trends of flow stress at both low and high strain rates.

The microstructure based model also predicts the deformation mechanism of the materials. Figure 6-6 shows the fraction of strain rates due to various deformation mechanisms, which are defined in equation (2.15), for the finest and coarsest grained materials. In the material with 7 micron grain size, the dominant deformation mechanism is grain boundary sliding below strain rate $10^{-3}s^{-1}$, and dislocation creep above strain rate $10^{-3}s^{-1}$. Theoretically, if grain boundary sliding operates alone(with some accommodation mechanism) it results in a stress exponent of 1 or 2, grain boundary diffusion results in a stress exponent of 1, and dislocation creep results in a stress exponent of 4 or 5 [159]. In our microstructure model, all three deformations operate simultaneously and interactively. The transition of the dominant mechanism in fine grained materials results in the overall stress exponent changing from 2 to 4 as strain rate increases in fine grained materials. In contrast, in the material with grain size 81.7 micron, dislocation creep dominants over the whole range of strain rate tested, hence no deformation mechanism transition occurs. This gives a relatively unchanged

overall stress exponent of 4. In addition, at fast strain rate, although dislocation creep dominates in both materials, grain boundary sliding still contributes a considerable amount to the overall deformation. For example, at strain rate of $3 \times 10^{-2} s^{-1}$, grain boundary sliding contributes about 30% to the overall deformation in 7 micron material, while it contributes only 10% in the material with 81.7 micron grain size. This explains the slight change of flow stress with grain size even at fast strain rates.

Biaxial forming was simulated using material models constructed by fitting (a) to the predictions of the microstructure-based finite element model; and (b) to the experimentally measured stress-v-strain rate data. To compare the results with experiments, terminal dome height after 1800 seconds of forming was compared for all conditions and is summarized in Figure 6-7. The predictions for dome height showed good agreement with the experimental results. Both predictions exhibited the same general shape of the curve, showing a decrease in dome height with increasing grain size, which asymptotically approaches some minimum value. The predictions for grain sizes above 10 microns are excellent with the predictions and models being within a few millimeters.

1.18 Conclusions

A multi-scale approach that links the microstructure based finite element model to the continuum scale finite element simulations of elevated temperature forming of Al alloys is proposed. The approach is used to predict the effect of grain size on bulge forming height for AA5083 and the results are compared to experimental measurements. The results of simulations and experiments show encouraging agreement with each other considering the small size of microstructure was used in the microstructural finite element model. The present study represents a first step towards the development of a methodology aimed at incooperating key microstructure features such as grain size, texture and precipiatate/dispersoid directly to predicting high temperature forming of AA5083 through numerical simulation.

Table 6-1 List of parameters used in microstructure based finite element simulations.

Parameter	Value
Temperature T	723 K
Atomic volume Ω	1.66×10^{-29} m^3
Young's modulus E	70 GPa
Poisson's ratio ν	0.3
Characteristic strain rate $\dot{\gamma}_0$	5.2 s^{-1}
Slip system strength g_0	65 MPa
Stress exponent of slip Λ	4.7
Grain boundary diffusion activation energy Q	1.34×10^{-19} J
Grain boundary diffusion pre-exponential δD_0	9.9×10^{-14} m^3 s^{-1}
Grain boundary sliding fluidity η_0	4.74×10^{-14} $m^4 J^{-1} s^{-1}$
Threshold stress σ_{th}	1.0 MPa

Table 6-2 Initial Sheet Thicknesses and Gas Pressures in the continuum level simulations.

Grain Size (μm)	Initial Sheet Thickness (mm)	Gas Pressure (MPa)
7.0	1.60	0.39
9.2	0.80	0.19
11.2	1.04	0.25
22.3	1.27	0.31
37.2	1.38	0.33
81.7	1.44	0.35

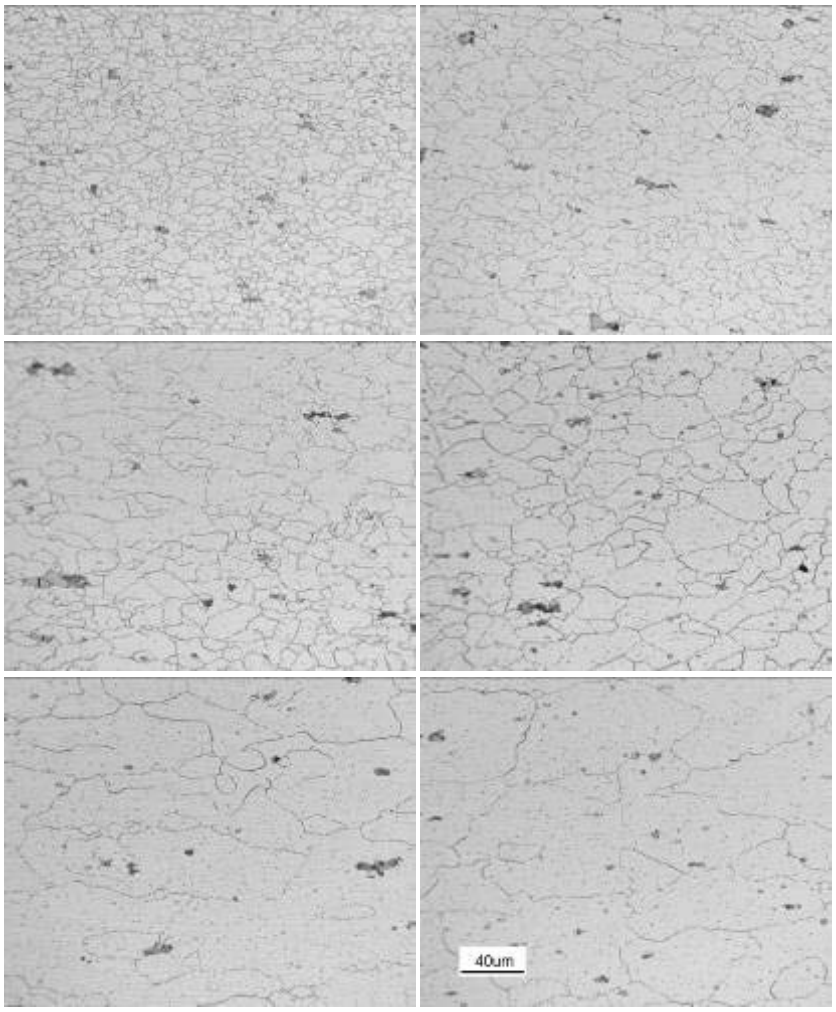

Figure 6-1 Photomicrographs of the grain size conditions: (a) 7μm, (b) 9.2μm, (c) 11.2μm, (d) 22.3μm, (e) 37.2μm and (f) 81.7μm.

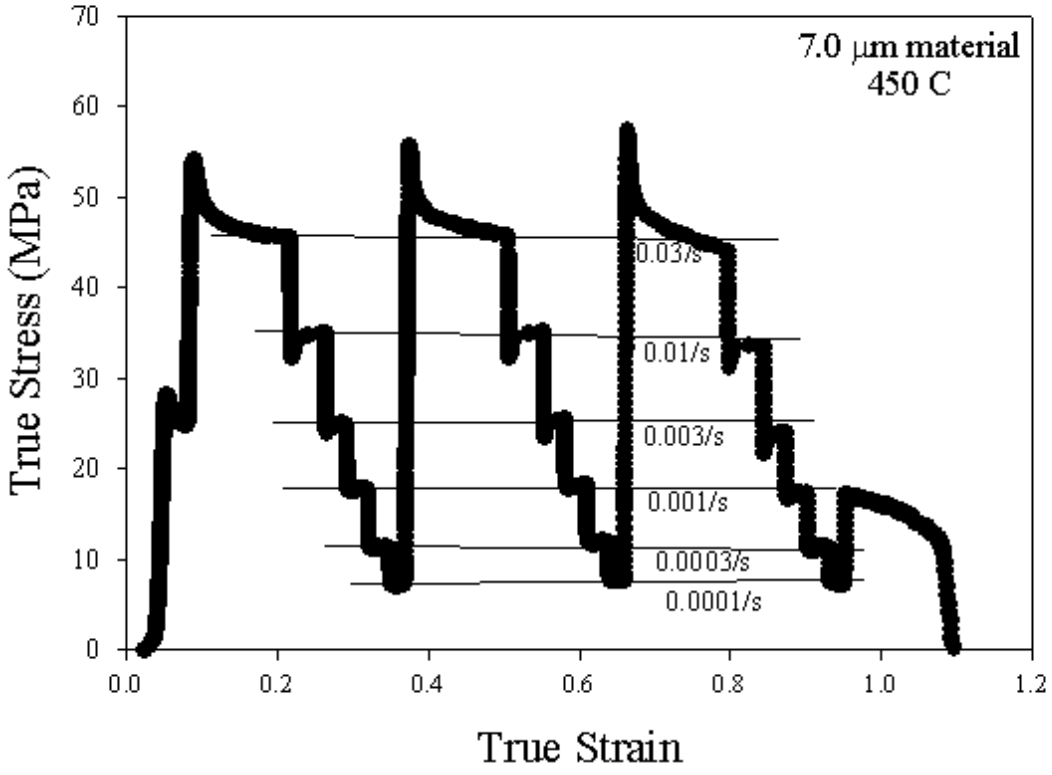

Figure 6-2 Step strain rate test results for 7.0μm grain size at 450ºC. Shows the strain rates tested and resultant flow stress after each strain rate decrement.

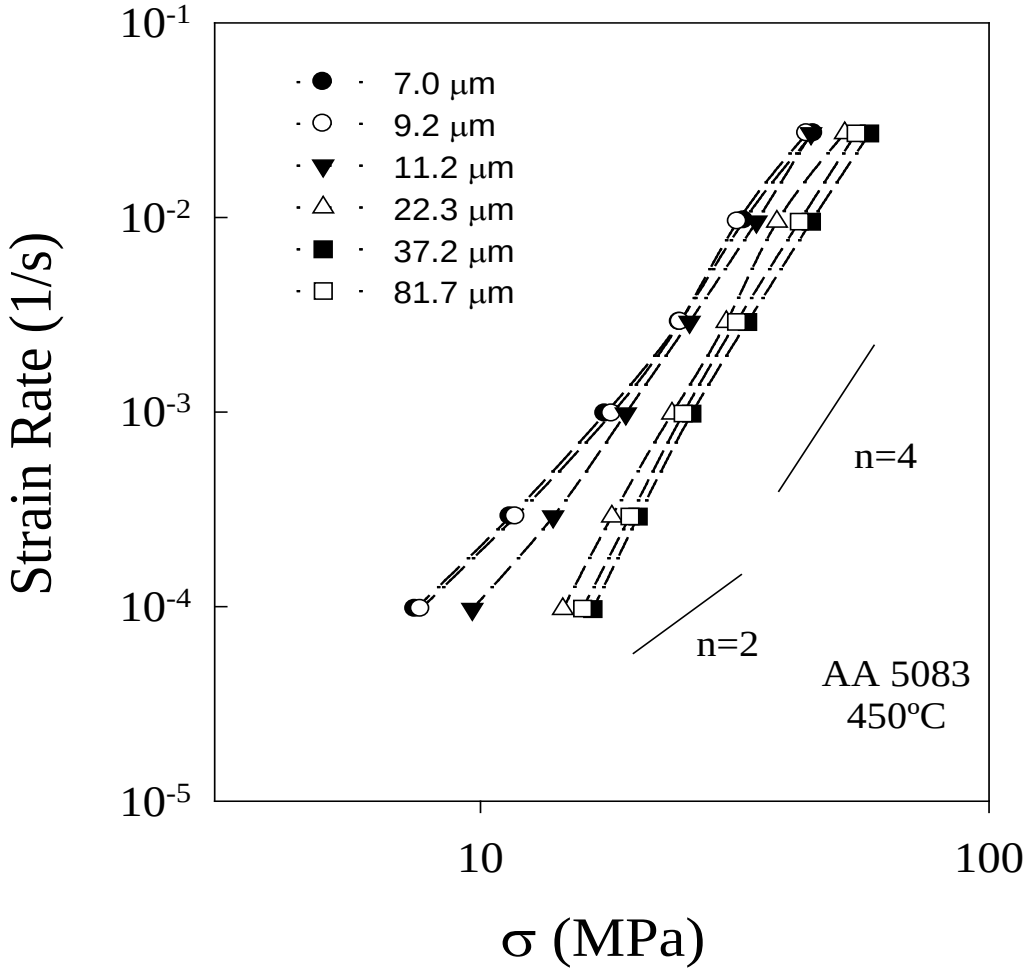

Figure 6-3 Effect of grain size and strain rate on flow stress and creep stress exponent, n, in AA5083 at 450ºC. Data generated using step strain rate testing.

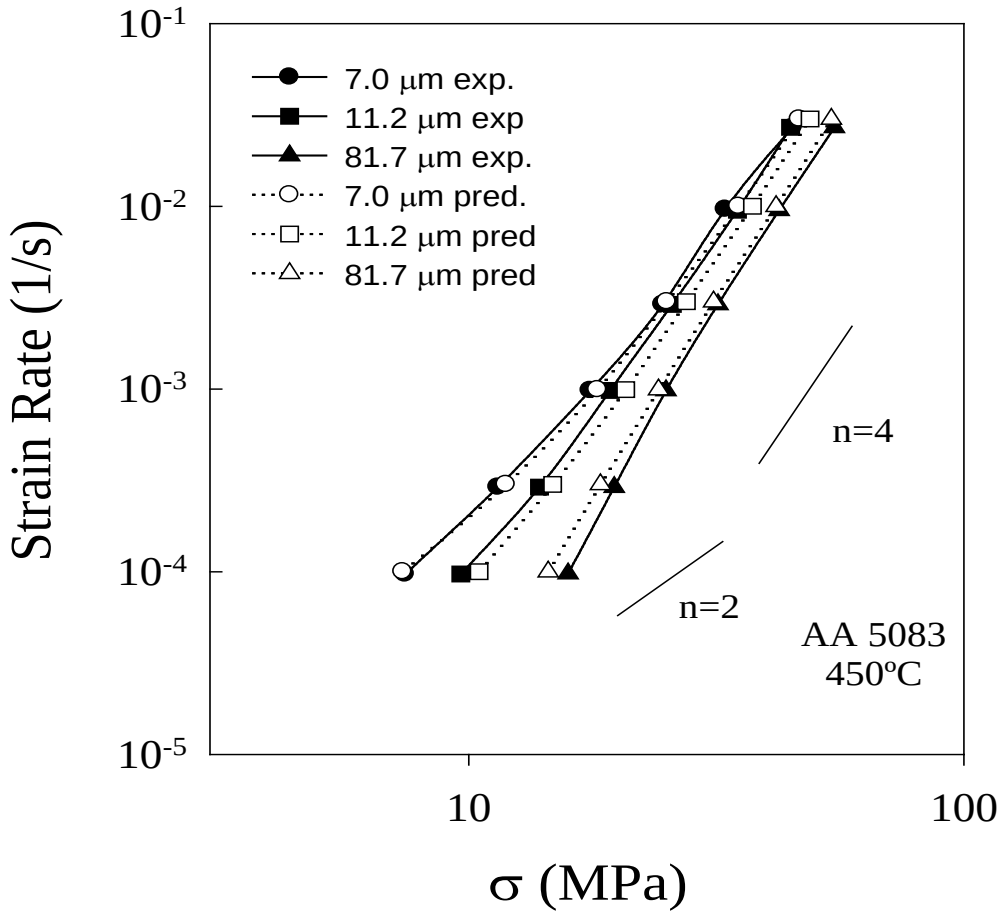

Figure 6-4 Strain rate versus stress data for 7.0 μm, 11.2 μm, and 81.7 μm AA5083 materials showing comparison of experimental results and numerical predictions.

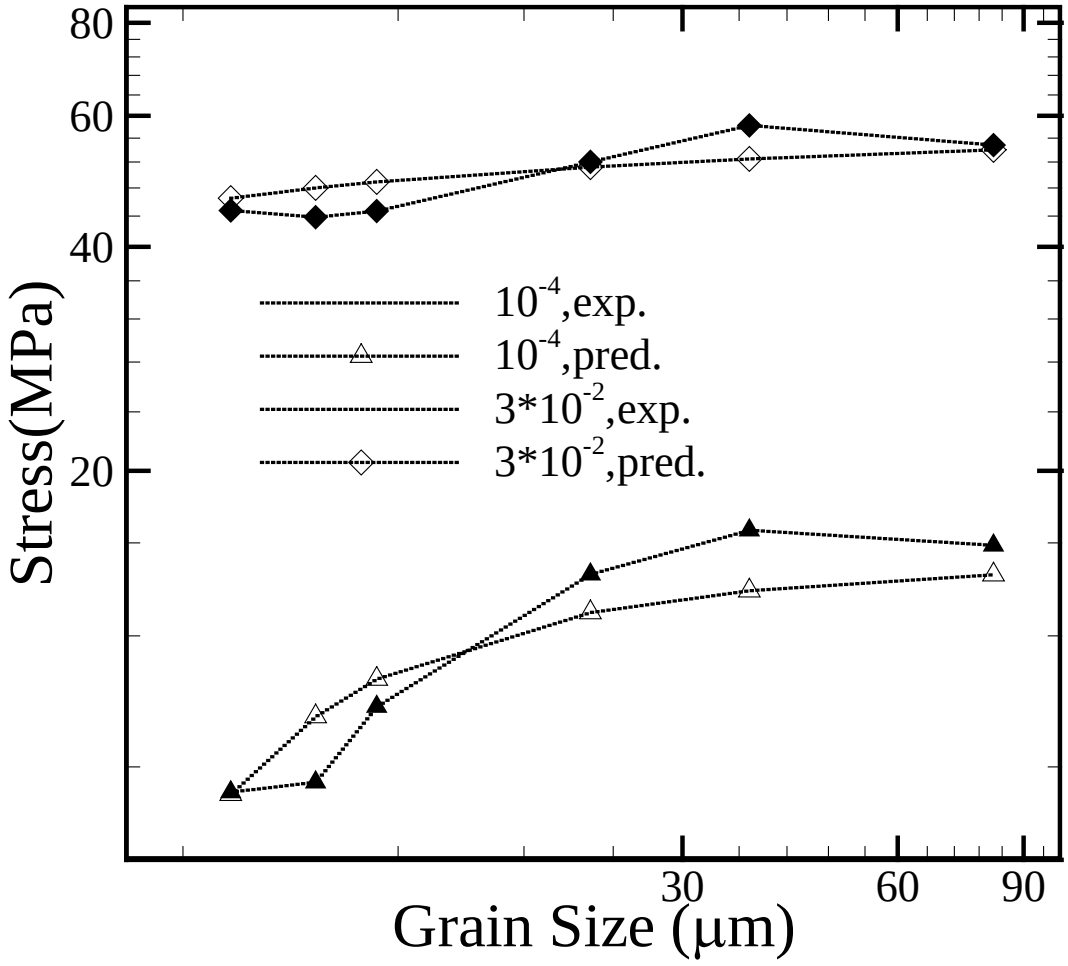

Figure 6-5 Effect of grain size on the flow stress at low and high strain rates.

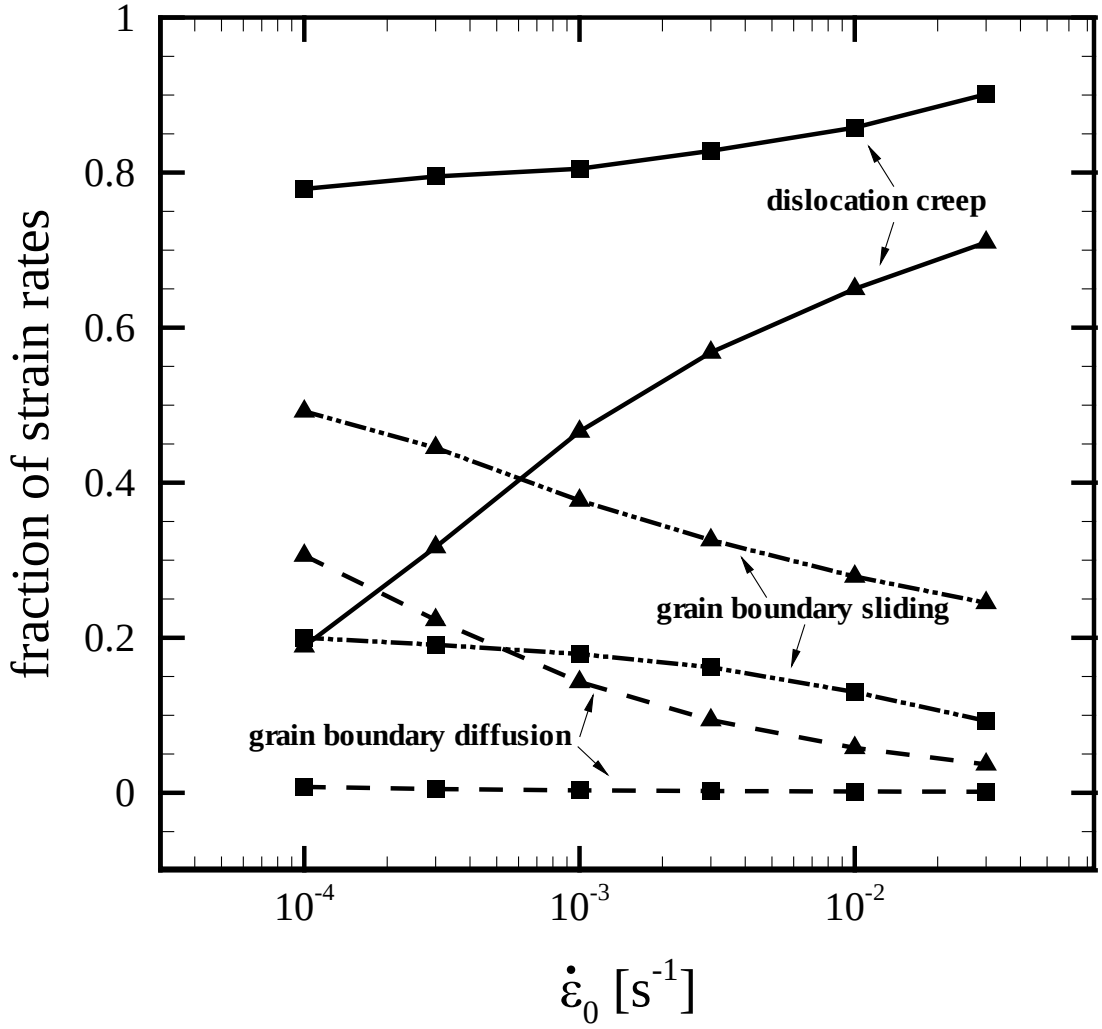

Figure 6-6 Fraction of strain rates resulted from various deformation mechanisms as a function of total strain rate for the materials with 7μm (delta) and 81.7μm (square) grain size.

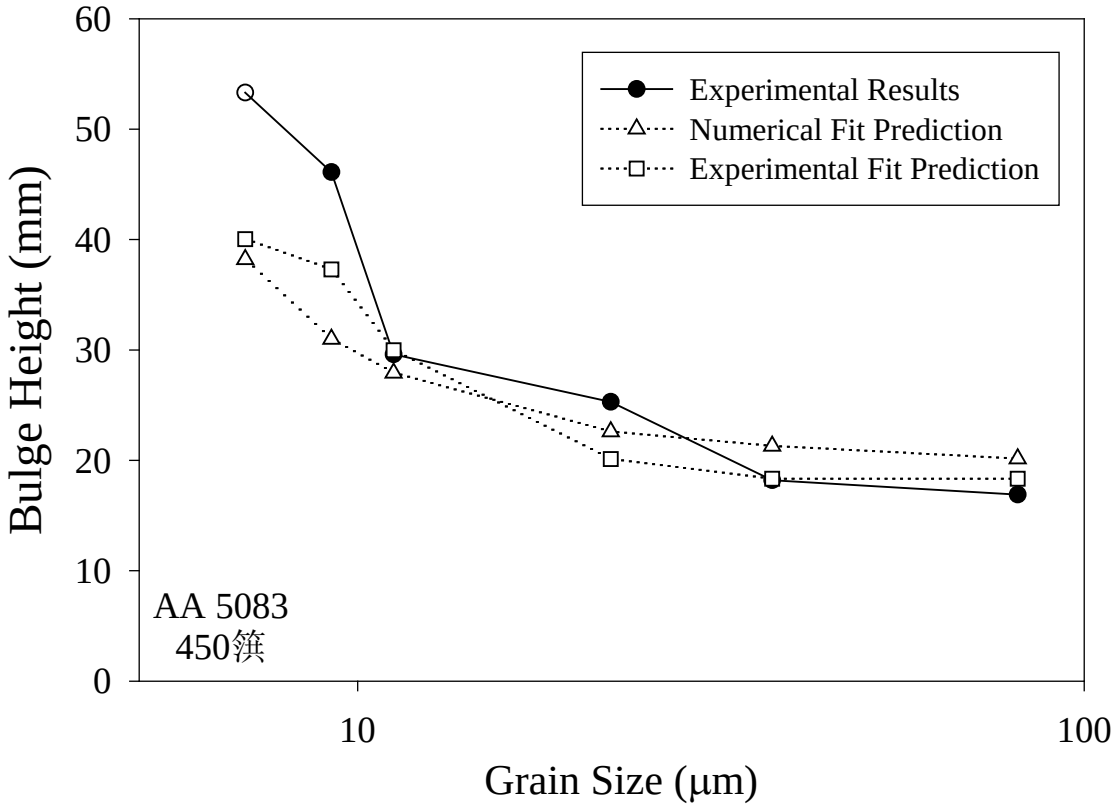

Figure 6-7 Dome height as a function of grain size at 450ºC and as measured experimentally and as predicted by finite element simulations using a constitutive model that was fit to (1) the uniaxial stress-v-strain rate predicted by the microstructure based finite element model; (2) the experimentally measured stress-v-strain data shown in Figure 6-3.

Chapter 7: Conclusions

This dissertation contains the investigation of a few aspects of superplastic flow and superplastic materials with numerical simulations at different length and time scales. Some attempts of incooperating simulations at various length scales are also presented.

In chapter 2, a finite element method rigorously accounts for the grain interior plasticity, grain boundary diffusion and grain boundary sliding is given. The method can be used to predict the constitutive response and microstructure evolution during deformation due to coupled mechanisms based on microstructural simulations. It can also be used to predict the contribution of each mechanism to the total plastic strain.

In chapter 3, the microstructure based finite element model is calibrated against the experiment measurements of Al AA5083 and used to estimate the influence of a threshold stress for grain boundary sliding on the relationship between macroscopic flow stress and strain rate for the material when subjected to plane strain uniaxial tension at 450°C. We find that a threshold stress less or equal to 4MPa has only a small influence

on flow stress and stress exponent in the dislocation creep regime (a threshold stress of 2MPa increases stress exponent from 4.2 to 4.5), but substantially increases both flow stress and stress exponent in the grain boundary sliding regime (a threshold stress of 2MPa increases *n* from 1.5 to 2.7). When a threshold stress is included in the model, good agreement is obtained between measured and predicted flow stress as a function of strain rate and resolves a discrepancy between theory and experiment reported in Agarwal et al [69].

In chapter 4, the microstructure finite element model is used to conduct a systematic study of the mechanisms of void growth in polycrystalline Al AA5083 during elevated temperature straining. The simulations were used to predict the effects of loading conditions, material parameters and microstructure on the rates and mechanisms of void growth. The predictions are shown to be in good agreement with experimental observations of cavitation in Aluminum. In addition, the simulations show that the rate of void growth is strongly sensitive to the detailed grain structure near the void. Consequently, the void growth rates in a realistic microstructure differ substantially from the predictions of models that idealize the grain structure as a periodic array.

In chapter 5, molecular dynamics simulations are used to investigate the effect of vacancies, Si and Mg impurities in the grain boundaries on grain boundary sliding. One symmetric tilt grain boundary and five asymmetric tilt grain boundaries are included in this study. The threshold stresses of grain boundary sliding for these grain boundaries with vacancies of two different concentrations are estimated and are compared to the threshold stress for the corresponding pure grain boundaries and we found that vacancies significantly decrease the threshold stress for grain boundary sliding in low energy grain boundaries by increasing the grain boundary diffusivity and has less significant effect in high energy grain boundaries. Si impurities greatly decrease the sliding threshold in high-energy grain boundaries by increasing energy/mobility of surrounding Al atoms and enhancing grain boundary diffusivity and Mg impurities increase sliding threshold of all grain boundaries independent of grain boundary energy by forming immobile clusters with surrounding Al atoms.

In chapter 6, a multi-scale approach that links the microstructure based finite element model to the continuum scale finite element simulations of elevated temperature forming of Al alloys is proposed. The approach is used to predict the effect of grain size on bulge forming height for AA5083 and the results are compared to experimental measurements. The results of simulations and experiments show encouraging agreement

with each other considering the small size of microstructure was used in the microstructural finite element model. The present study represents a first step towards the development of a methodology aimed at incooperating key microstructure features such as grain size, texture and precipiatate/dispersoid directly to predicting high temperature forming of AA5083 through numerical simulation.

Reference

[1] Nieh TG, Wadsworth J, Sherby OD. Superplasticity in metals and ceramics: Cambridge University Press, 1997.

[2] Chandra N. Constitutive behavior of superplastic materials. Int J Nonlinear Mech 2002;37:461.

[3] Barnes AJ. Superplastic aluminum forming - Expanding its techno-economic niche. Materials Science Forum 1999;304-306:785.

[4] Barnes AJ. Industrial applications of superplastic forming: Trends and prospects. Materials Science Forum 2001;357-359:3.

[5] Barnes AJ. Superplastic forming 40 years and still growing. J Mater Eng Perform 2007;16:440.

[6] Krajewski PE, Morales AT. Tribological issues during quick plastic forming. J Mater Eng Perform 2004;13:700.

[7] Krajewski PE, Schroth JG. Overview of Quick Plastic Forming Technology. Materials Science Forum 2007;551-552:3.

[8] Schroth JG. General Motors' Quick Plastic Forming Process. In: Taleff EM, Friedman PA, Krajewski PE, Mishra RS, Schroth JG, editors. Advances in Superplasticity and Superplastic Forming: Minerals, Metals, & Materials Society, 2004. p.9.

[9] Taleff EM, Nevland PJ, Krajewski PE. Tensile ductility of several commercial aluminum alloys at elevated temperatures. Metall Mater Trans A 2001;32:1119.

[10] Kaibyshev OA. Superplasticity of alloys, intermetallides, and ceramics: Springer-verlag, 1992.

[11] Langdon TG. An Evaluation of the Strain Contributed by Grain-Boundary Sliding in Superplasticity. Mat Sci Eng a-Struct 1994;174:225.

[12] Higashi K. Research and developement towards grain-boundary-plasticity from superplasticity. In: Taleff EM, Friedman PA, Krajewski PE, mishra RS, Schroth JG, editors. Advances in Superplasticity and Superplastic Forming: Minerals, Metals, & Materials Society, 2004. p.253.

[13] Raj R, Ashby MF. On grain boundary sliding and diffusional creep. Metallurgical and Materials Transactions B 1971;2:1113.

[14] Ashby MF, Verrall RA. Diffusion-Accommodated Flow and Superplasticity. Acta Metall Mater 1973;21:149.

[15] Ashby MF, Edward GH, Davenport J, Verrall RA. Application of Bound Theorems for Creeping Solids and Their Application to Large Strain Diffusional Flow. Acta Metall Mater 1978;26:1379.

[16] Yang W, Wang HT. Mechanics modeling for deformation of nano-grained metals. J Mech Phys Solids 2004;52:875.

[17] Wang HT, Yang W. Constitutive modeling for nanocrystalline metals based on cooperative grain boundary mechanisms. J Mech Phys Solids 2004;52:1151.

[18] Ball A, Hutchison MM. Superplasticity in the aluminium-zinc eutectoid. Met. Sci. J. 1969;3:1.

[19] Mukherjee AK. The rate controlling mechanism in superplasticity. Mater Sci Eng 1971;8:83.

[20] Langdon TG. Grain boundary sliding as a deformation mechanism during creep. Philosophical Magazine 1970;22:689.

[21] Hayden HW, Floreen S, Goodell PD. The deformation mechanisms of superplasticity. Metallurgical and Materials Transactions B 1972;3:833.

[22] Arieli A, Mukherjee AK. A Model for the Rate-Controlling Mechanism in Superplasticity. Mater Sci Eng 1980;45:61.

[23] Gifkins RC. Grain-Boundary Sliding and Its Accommodation during Creep and Superplasticity. Metall Trans A 1976;7:1225.

[24] Ghosh AK. A New Physical Model for Superplastic Flow. vol. 170: Aedermannsdorf, Switzerland: Trans Tech Publications, 1984-, 1994. p.39.

[25] Gittus JH. Theory of Superplastic Flow in 2-Phase Materials - Roles of Interphase-Boundary Dislocations, Ledges, and Diffusion. J Eng Mater-T Asme 1977;99:244.

[26] Kaibyshev OA, Valiev RZ, Emaletdinov AK. Deformation mechanisms and the theory of structural superplasticity of metals. physica status solidi (a) 1985;90:197.

[27] Langdon TG. A Unified Approach to Grain-Boundary Sliding in Creep and Superplasticity. Acta Metallurgica Et Materialia 1994;42:2437.

[28] Langdon TG. Grain boundary sliding revisited: Developments in sliding over four decades. J Mater Sci 2006;41:597.

[29] Padmanabhan KA. Theory of Structural Superplasticity. Mater Sci Eng 1977;29:1.

[30] Namilae S, Chandra N, Nieh TG. Atomistic simulation of grain boundary sliding in pure and magnesium doped aluminum bicrystals. Scripta Mater 2002;46:49.

[31] Chandra N, Dang P. Atomistic simulation of grain boundary sliding and migration. Journal of Materials Science 1999;34:655.

[32] Qi Y, Krajewski PE. Molecular dynamics simulations of grain boundary sliding: The effect of stress and boundary misorientation. Acta Materialia 2007;55:1555.

[33] Mishin Y, Farkas D. Atomistic simulation of [001] symmetrical tilt grain boundaries in NiAl. Philos Mag A 1998;78:29.

[34] Hoagland RG, Kurtz RJ. The relation between grain-boundary structure and sliding resistance. Philos Mag A 2002;82:1073.

[35] Shiga M, Shinoda W. Stress-assisted grain boundary sliding and migration at finite temperature: A molecular dynamics study. Phys Rev B 2004;70.

[36] Uesugi T, Tsuchiya K, Kohyama M, Higashi K. Grain Boundary Sliding of Sigma 5(001) Twist Grain Boundary in Aluminum Bicrystal from First-Principles Calculations. Materials Science Forum 2004;447--448:27.

[37] Cahn JW, Taylor JE. A unified approach to motion of grain boundaries, relative tangential translation along grain boundaries, and grain rotation. Acta Materialia 2004;52:4887.

[38] Cahn JW, Mishin Y, Suzuki A. Coupling grain boundary motion to shear deformation. Acta Materialia 2006;54:4953.

[39] Zhang H, Duy D, Srolovitz DJ. Effects of boundary inclination and boundary type on shear-driven grain boundary migration. Philosophical Magazine 2008;88:243.

[40] Weinberg F. Grain Boundary Shear in Aluminum. Trans.\ AIME 1958;212:808.

[41] Kokawa H, Watanabe T, Karashima S. Sliding Behavior and Dislocation Structures in Aluminum Grain Boundaries. Philosophical Magazine~A 1981;44:1239.

[42] Bernstein IM, Swartz JC, Rath BB. The Effect of Torsional Stress on Pure Twist Boundaries. The Philosophical Magazine 1969;20:849.

[43] Kato M. Grain Boundary Sliding in High-Purity Aluminium Bicrystal and Al-Cu Solid Solution Bicrystal during Plastic Deformation. Transactions of the Japan Institute of Metals 1969;10:215.

[44] Halliday MD, Beevers CJ. Some Observations of Grain-Boundary Sliding in Aluminium Bicrystals Tested at Constant Strain Rate and Constant Rate of Stress Increase. Journal of Materials Science 1971;6:1254.

[45] Fukutomi H, Iseki T, Endo T, Kamijo T. Sliding Behavior of Coincidence Grain-Boundaries Deviating from Ideal Symmetrical Tilt Relationship. Acta Metallurgica Et Materialia 1991;39:1445.

[46] Fukutomi H, Nonomura K, Takada Y, Yamamoto T. Effect of stress change on the behavior of grain boundary sliding of aluminium bicrystals. Mater Sci Forum 1997;233-:399.

[47] Fukutomi H, Yamamoto T, Nonomura K, Takada K. Examination of dislocation mechanism on grain boundary sliding in high angle grain boundaries by stress change test. Interface Science 1999;7:141.

[48] Monzen R, Futakuchi M, Suzuki T. Misorientation Dependence of Nanometer Grain-Boundary Sliding of [011]-Twist Boundaries in Copper. Scripta Metall Mater 1995;32:1277.

[49] Monzen R, Takada N. Nanometer sliding of [001] symmetric tilt boundaries in copper with boundary precipitates. Mat Sci Eng a-Struct 1997;234:202.

[50] Miura H, Sakai T, Otsuka T, Monzen R, Onaka S. Sliding of copper [001]-twist grain boundaries detected by shear deformation of liquid B2O3 particles on the grain boundaries. Acta Materialia 2000;48:1959.

[51] Watanabe T, Yamada M, Shima S, Karashima S. Misorientation Dependence of Grain-Boundary Sliding in (1010) Tilt Zinc Bicrystals. Philos Mag A 1979;40:667.

[52] Watanabe T, Kimura SI, Karashima S. The Effect of a Grain-Boundary Structural Transformation on Sliding in (1010)-Tilt Zinc Bicrystals. Philos Mag A 1984;49:845.

[53] Fukutomi H, Horiuchi R. Grain-Boundary Sliding of (111) Symmetric Tilt Boundaries in Aluminum. Journal of the Japan Institute of Metals 1983;47:457.

[54] Bower AF, Wininger E. A two-dimensional finite element method for simulating the constitutive response and microstructure of polycrystals during high temperature plastic deformation. J Mech Phys Solids 2004;52:1289.

[55] Kaibyshev R, Musin F, Lesuer DR, Nieh TG. Superplastic behavior of an Al-Mg alloy at elevated temperatures. Mat Sci Eng a-Struct 2003;342:169.

[56] Bae DH, Ghosh AK. Grain size and temperature dependence of superplastic deformation in an Al-Mg alloy under isostructural condition. Acta Mater 2000;48:1207.

[57] Agarwal S. Evaluation and prediction of material response during superplastic forming at various strain rates. Divsion of Engineering, vol. Ph. D. Providence, RI: Brown University, 2006.

[58] Kulas MA, Green WP, Taleff EM, Krajewski PE, McNelley TR. Failure mechanisms in superplastic AA5083 materials. Metall Mater Trans A 2006;37A:645.

[59] Valiev RZ, Kaibyshev OA. On the Quantitative-Evaluation of Superplastic Flow Mechanisms. Acta Metall Mater 1983;31:2121.

[60] Chandra N, Murali K. A Micromechanistic Model of Superplastic Behavior in Pseudo Single-Phase Aluminum-Alloys. Scripta Metall Mater 1995;32:1429.

[61] Murali K, Chandra N. Micromechanical Modeling of Superplastic Deformation. Acta Metallurgica Et Materialia 1995;43:1783.

[62] Dang P, Chandra N. A micromechanical model for dual-phase superplastic materials. Acta Mater 1998;46:2851.

[63] Chandra N, Rama J, Dang P. Application of micromechanical polycrystalline model in the study of threshold stress effects on superplasticity. Mat Sci Eng a-Struct 1997;231:134.

[64] Chandra N, Dang P. Application of micromechanical model to high strain rate superplastic materials. Scripta Mater 1997;36:1327.

[65] Blandin JJ, Dendievel R. A mesoscale model to predict the effect of microstructural heterogeneities on superplastic deformation. Acta Mater 2000;48:1541.

[66] Pan J, Cocks ACF. Computer simulation of superplastic deformation. Computational Materials Science 1993;1:95.

[67] Onck P, Van der Giessen E. Influence of microstructural variations on steady state creep and facet stresses in 2-D freely sliding polycrystals. Int J Solids Struct 1997;34:703.

[68] Simone A, Duarte CA, Van der Giessen E. A Generalized Finite Element Method for polycrystals with discontinuous grain boundaries. Int J Numer Meth Eng 2006;67:1122.

[69] Agarwal S, Briant CL, Krajewski PE, Bower AF, Taleff EM. Experimental validation of two-dimensional finite element method for simulating constitutive response of polycrystals during high temperature plastic deformation. J Mater Eng Perform 2007;16:170.

[70] Cipoletti DE, Bower AF, Qi Y, Krajewski PE. The influence of heterogeneity in grain boundary sliding resistance on the constitutive behavior of AA5083 during high-temperature deformation. Mat Sci Eng a-Struct 2009;504:175.

[71] Frost HJ, Ashby MF. Deformation-mechanism maps: the plasticity and creep of metals and ceramics: Pergamon Press, 1982.

[72] Buchovecky EJ, Du N, Bower AF. A Model of Sn Whisker Growth by Coupled Plastic Flow and Grain Boundary Diffusion. Applied Physics Letters 2009;94.

[73] Kulas MA, Green WP, Taleff EM, Krajewski PE, McNelley TR. Deformation mechanisms in superplastic AA5083 materials. Metall Mater Trans A 2005;36A:1249.

[74] Agarwal S, Krajewski PE, Briant CL. Texture development and dynamic recrystallization in AA5083 during superplastic forming at various strain rates. In: Taleff EM, Friedman PA, Krajewski PE, mishra RS, Schroth JG, editors. Advances in Superplasticity and Superplastic Forming: Minerals, Metals, & Materials Society, 2004. p.95.

[75] Chauhan M, Roy I, Mohamed FA. Creep behavior in near-nanostructured Al 5083 alloy. Mat Sci Eng a-Struct 2005;410:24.

[76] Ridley N, Bate PS, Zhang B. Effect of strain rate path on cavitation in superplastic aluminium alloy. Mat Sci Eng a-Struct 2007;463:224.

[77] Mabuchi M, Chino Y, Iwasaki H. An investigation of cavity growth rate in superplastic Al and Mg alloys. Pricm 5: The Fifth Pacific Rim International Conference on Advanced Materials and Processing, Pts 1-5 2005;475-479:2945.

[78] Kawasaki M, Xu C, Langdon TG. An investigation of cavity growth in a superplastic aluminum alloy processed by ECAP. Acta Mater 2005;53:5353.

[79] Kawasaki M, Huang Y, Xu C, Furukawa M, Horita Z, Langdon TG. A quantitative study of cavity development in the tensile testing of an aluminum metal matrix composite processed by equal-channel angular pressing. Mat Sci Eng a-Struct 2005;410:402.

[80] Chandra N, Khraisheh MK, Kalu P. Effect of state of stress on the cavitation behavior of Al 5083 superplastic material. Pricm 5: The Fifth Pacific Rim International Conference on Advanced Materials and Processing, Pts 1-5 2005;475-479:2931.

[81] Chino Y, Iwasaki H, Mabuchi M. Cavity growth rate in superplastic 5083 Al and AZ31 Mg alloys. J Mater Res 2004;19:3382.

[82] Ma ZY, Mishra RS. Cavitation in superplastic 7075Al alloys prepared via friction stir processing. Acta Mater 2003;51:3551.

[83] Cleveland RM, Ghosh AK, Bradley JR. Comparison of superplastic behavior in two 5083 aluminum alloys. Mat Sci Eng a-Struct 2003;351:228.

[84] Bae DH, Ghosh AK, Bradley JR. Stress-state dependence of cavitation and flow behavior in superplastic aluminum alloys. Metall Mater Trans A 2003;34A:2449.

[85] Bae DH, Ghosh AK. Cavity formation and early growth in a superplastic Al-Mg alloy. Acta Mater 2002;50:511.

[86] Bae DH, Ghosh AK. Observations related to healing of interface damage and cavity nucleation during superplastic flow. Mat Sci Eng a-Struct 2002;322:233.

[87] Bae DH, Ghosh AK. Cavity growth during superplastic flow in an Al-Mg alloy: I. Experimental study. Acta Mater 2002;50:993.

[88] Khraishi TA, Khaleel MA, Zbib HM. A parametric-experimental study of void growth in superplastic deformation. Int J Plasticity 2001;17:297.

[89] Iwasaki H, Mabuchi M, Higashi K. Plastic cavity growth during superplastic flow in AA 7475 Al alloy containing a small amount of liquid. Acta Mater 2001;49:2269.

[90] Chen CL, Tan MJ. Cavity growth and filament formation of superplastically deformed Al 7475 Alloy. Mat Sci Eng a-Struct 2001;298:235.

[91] Troeger LP, Starke EA. Microstructural and mechanical characterization of a superplastic 6xxx aluminum alloy. Mat Sci Eng a-Struct 2000;277:102.

[92] Hosokawa H, Iwasaki H, Mori T, Mabuchi M, Tagata T, Higashi K. Effects of Si on deformation behavior and cavitation of coarse-grained Al-4.5mg alloys exhibiting large elongation. Acta Mater 1999;47:1859.

[93] Koenigsmann HJ, Starke EA. Cavity nucleation and fracture in an Al-Si-Ge alloy. Aluminium Alloys: Their Physical and Mechanical Properties, Pts 1-3 1996;217:1479.

[94] Mahidhara RK, Mukherjee AK. Mechanisms of cavity growth in a fine-grained 7475 Al superplastic alloy. Mater Design 1995;16:343.

[95] Somekawa H, Mukai T. Effect of dominant diffusion process on cavitation behavior in superplastic Mg-AI-Zn alloy. Scripta Mater 2007;57:1008.

[96] Kawasaki M, Kubota K, Higashi KI, Langdon TG. Flow and cavitation in a quasi-superplastic two-phase magnesium-lithium alloy. Mat Sci Eng a-Struct 2006;429:334.

[97] Zhang KF, Yin DL, Wang GF, Han WB. Cavitation behavior during superplastic deformation of AZ31 magnesium alloy. J Mater Sci Technol 2005;21:510.

[98] Lee CJ, Huang JC. Cavitation characteristics in AZ31 Mg alloys during LTSP or HSRSP. Acta Mater 2004;52:3111.

[99] Mulholland M, Khraishi T, Shen YL, Horstemeyer M. Void growth and interaction experiments: Implications to the optimal straining rate in superplastic forming. Int J Plasticity 2006;22:1728.

[100] Kassner ME, Hayes TA. Creep cavitation in metals. Int J Plasticity 2003;19:1715.

[101] Chokshi AH. Cavity nucleation and growth in superplasticity. Mat Sci Eng a-Struct 2005;410:95.

[102] Needleman A, Tvergaard V, Hutchinson JW. Void growth in plastic solids. Topics in Fracture and Fatigue 1992:145.

[103] Rice JR, Tracey DM. On the ductile enlargement of voids in triaxial stress fields. J Mech Phys Solids 1969;17:201.

[104] McClintock FA. A criterion for ductile fracture by the growth of holes. Journal of Applied Mechanics 1968;35:363.

[105] Lee BJ, Mear ME. Evolution of elliptical voids in power-law viscous solids. Mech Mater 1999;31:9.

[106] Lee BJ, Mear ME. Studies of the growth and collapse of voids in viscous solids. J Eng Mater-T Asme 1994;116:348.

[107] Budiansky B, Hutchinson JW, Slutsky S. Void growth and collapse in viscous solids. Mechanics of solids: The Rodney Hill 60 th anniversary volume.(A 83-25302 10-39) Oxford, Pergamon Press 1982:13.

[108] Hull D, Rimmer DE. The growth of grain-boundary voids under stress. Philos Mag 1959;4:673.

[109] Cocks ACF, Searle AA. Void growth by grain-boundary diffusion in fine-grained materials. Mech Mater 1991;12:279.

[110] Beere W, Speight MV. Creep cavitation by vacancy diffusion in plastically deforming solid. Met Sci 1978;12:172.

[111] Edward GH, Ashby MF. Intergranular Fracture during Power-Law Creep. Acta Metallurgica 1979;27:1505.

[112] Needleman A, Rice JR. Plastic Creep Flow Effects in the Diffusive Cavitation of Grain-Boundaries. Acta Metallurgica 1980;28:1315.

[113] Cocks ACF, Ashby MF. On creep fracture by void growth. Prog Mater Sci 1982;27:189.

[114] Sham TL, Needleman A. Effects of Triaxial Stressing on Creep Cavitation of Grain-Boundaries. Acta Metallurgica 1983;31:919.

[115] Van der Giessen E, Van der Burg MWD, Needleman A, Tvergaard V. Void Growth Due to Creep and Grain-Boundary Diffusion at High Triaxialities. J Mech Phys Solids 1995;43:123.

[116] Van der Giessen E, Tvergaard V. Interaction of Cavitating Grain-Boundary Facets in Creeping Polycrystals. Mech Mater 1994;17:47.

[117] Tvergaard V. Effect of Grain-Boundary Sliding on Creep Constrained Diffusive Cavitation. J Mech Phys Solids 1985;33:447.

[118] Tvergaard V. On the Creep Constrained Diffusive Cavitation of Grain-Boundary Facets. J Mech Phys Solids 1984;32:373.

[119] Cocks ACF. The nucleation and growth of voids in a material containing a distribution of grain-boundary particles. Acta Metallurgica 1985;33:129.

[120] Sutton AP, Balluffi RW. Interfaces in crystalline materials: Clarendon Press Oxford, 1995.

[121] Suzuki A, Mishin Y. Interaction of point defects with grain boundaries in fcc metals. Interface Science 2003;11:425.

[122] Suzuki A, Mishin Y. Atomistic modeling of point defects and diffusion in copper grain boundaries. Interface Science 2003;11:131.

[123] Lu G, Kioussis N. Interaction of vacancies with a grain boundary in aluminum: A first-principles study. Phys Rev B 2001;6402.

[124] Farkas D. Atomistic theory and computer simulation of grain boundary structure and diffusion. J Phys-Condens Mat 2000;12:R497.

[125] Vetrano JS, Simonen EP, Bruemmer SM. Evidence for excess vacancies at sliding grain boundaries during superplastic deformation. Acta Materialia 1999;47:4125.

[126] Vetrano JS, Simonen EP, Bruemmer SM. Grain boundary structure and composition following superplastic deformation of Al-Mg alloys. Materials Science Forum 1997;243-245:493.

[127] Vetrano JS, Henager Jr CH, Simonen EP. Role of vacancies and solute atoms on grain boundary sliding. vol. 601. Boston, MA, USA: Materials Research Society, 2000. p.169.

[128] Zehetbauer MJ, Steiner G, Schafler E, Korznikov A, Korznikova E. Deformation induced vacancies with severe plastic deformation: Measurements and modelling. Nanomaterials by Severe Plastic Deformation 2006;503-504:57.

[129] Wu XL, Li B, Ma E. Vacancy clusters in ultrafine grained Al by severe plastic deformation. Appl Phys Lett 2007;91.

[130] Vetrano JS, Lavender CA, Bruemmer SM. Impurity segregation during superplastic deformation of Al-Mg-Mn alloys. Materials Science Forum 1994;170-172:225.

[131] Li XT, Li TJ, Li XM, Jin JZ. Study of ultrasonic melt treatment on the quality of horizontal continuously cast Al-1%Si alloy. Ultrason Sonochem 2006;13:121.

[132] Vetrano JS, Lavender CA, Bruemmer SM. Interfacial Segregation and Deformation of Superplastically Deformed Al-Mg-Mn Alloys. In: Ghosh AK, Bieler TR, editors. Superplasticity and Superplastic Forming. Warrendale, PA: TMS, 1995. p.49.

[133] Malis T, Chaturvedi MC. GRAIN-BOUNDARY SEGREGATION IN AN Al - 8 wt% Mg ALLOY. Journal of Materials Science 1982;17:1479.

[134] Vetrano JS, Lavender CA, Bruemmer SM. Interfacial segregation and deformation of superplastically deformed Al-Mg-Mn alloys. Las Vegas, NV, USA: Minerals, Metals & Materials Soc (TMS), 1995. p.49.

[135] Lambri OA, Massot M, Riehemann W, Lucioni EJ, Plazaola F, Garcia JA. The role of vacancies in the mobility of dislocations and grain boundaries in magnesium. Physica Status Solidi a-Applications and Materials Science 2007;204:1077.

[136] Vetrano JS, Henager Jr CH, Guertsman VY. Influence of grain boundary structure and composition on superplastic deformation. Charlotte, NC., United states: Minerals, Metals and Materials Society, 2004. p.225.

[137] Green WP, Kulas MA, Niazi A, Oishi K, Taleff EM, Krajewski PE, McNelley TR. Deformation and failure of a superplastic AA5083 aluminum material with a Cu addition. Metall Mater Trans A 2006;37A:2727.

[138] Mima G, Oka T, Nishi T. On the Grain Boundary Sliding of Aluminum Alloy Bicrystals during the Tensile Test under Constant Stress and Heating Rate Conditions. Journal of the Japan Institute of Metals 1969;33:639.

[139] Maruyama K, Wananabe Y, Oikawa H. Grain Boundary Strengthening at Elevated Temperatures: Creep of Aluminum Doped Zinc Bicrystals and Polycrystals. Acta Metallurgica 1986;34:2343.

[140] Molteni C, Marzari N, Payne MC, Heine V. Sliding mechanisms in aluminum grain boundaries. Physical Review Letters 1997;79:869.

[141] Ballo P, Kioussis N, Lu G. Grain boundary sliding and migration: Effect of temperature and vacancies. Phys Rev B 2001;6402.

[142] Ballo P, Degmova J, Slugen V. Grain boundary sliding and migration in copper: Vacancy effect. Phys Rev B 2005;72.

[143] Ballo P, Slugen V. Grain boundary sliding and migration in copper: the effect of vacancies. Computational Materials Science 2005;33:491.

[144] Wang L, Zhang HW, Deng X. Influence of defects on mechanical properties of bicrystal copper grain boundary interfaces. J Phys D Appl Phys 2008;41.

[145] Monk J, Hyde B, Farkas D. The role of partial grain boundary dislocations in grain boundary sliding and coupled grain boundary motion. Journal of Materials Science 2006;41:7741.

[146] Sansoz F, Molinari JF. Mechanical behavior of Sigma tilt grain boundaries in nanoscale Cu and Al: A quasicontinuum study. Acta Materialia 2005;53:1931.

[147] Van Swygenhoven H, Derlet PA. Grain-boundary sliding in nanocrystalline fcc metals. Phys Rev B 2001;64.

[148] Liu X, Wang X, Wang J, Zhang H. First-Principles Investigation of Mg Segregation at $ = 11(113)$ Grain Boundaries in Al. Journal of Physics: Condensed Matter 2005;17:4301.

[149] Du NN, Bower AF, Krajewski PE, Taleff EM. The influence of a threshold stress for grain boundary sliding on constitutive response of polycrystalline Al during high temperature deformation. Mat Sci Eng a-Struct 2008;494:86.

[150] Nose S. A molecular dynamics method for simulations in the canonical ensemble (Reprinted from Molecular Physics, vol 52, pg 255, 1984). Mol Phys 2002;100:191.

[151] Nose S. A Unified Formulation of the Constant Temperature Molecular-Dynamics Methods. J Chem Phys 1984;81:511.

[152] Hoover WG. Canonical Dynamics - Equilibrium Phase-Space Distributions. Phys Rev A 1985;31:1695.

[153] Lee BJ, Shim JH, Baskes MI. Semiempirical atomic potentials for the fcc metals Cu, Ag, Au, Ni, Pd, Pt, Al, and Pb based on first and second nearest-neighbor modified embedded atom method. Phys Rev B 2003;68.

[154] Gall K, Horstemeyer MF, Van Schilfgaarde M, Baskes MI. Atomistic simulations on the tensile debonding of an aluminum-silicon interface. J Mech Phys Solids 2000;48:2183.

[155] Jelinek B, Houze J, Kim S, Horstemeyer MF, Baskes MI, Kim SG. Modified embedded-atom method interatomic potentials for the Mg-Al alloy system. Phys Rev B 2007;75.

[156] Yang CC, Rollett AD, Mullins WW. Measuring relative grain boundary energies and mobilities in an aluminum foil from triple junction geometry. Scripta Mater 2001;44:2735.

[157] Hatch JE. Aluminum: properties and physical metallurgy: ASM International, 1984.

[158] bradley JR. Bulge testing of superplastic AA5083 aluminum sheet. In: taleff EM, Friedman PA, Krajewski PE, Mishra RS, Schroth JG, editors. TMS. Warrendale, PA, 2004.

[159] Nieh TG, Wadsworth J, Sherby OD. Superplasticity in metals and ceramics. Cambridge ; New York: Cambridge University Press, 1997.